Heinz Raether

Surface Plasmons

on Smooth and Rough Surfaces and on Gratings

With 113 Figures

Preface

This review describes the basic physics of surface plasmons (SPs) propagating on smooth and corrugated surfaces. SPs represent electromagnetic surface waves that have their intensity maximum *in* the surface and exponentially decaying fields perpendicular to it. They can be produced not only by electrons, but also by light in an optical device called the attenuated total reflection (ATR). An important property of the SPs is their coupling with photons via corrugated surfaces and vice versa, so that the SPs become involved in a series of optical phenomena. With the excitation of SPs by light, a strong enhancement of the electromagnetic field in the surface (resonance amplification) is combined, which can be rather strong. This has been demonstrated first by the excitation of SPs on a rough silver surface which emits light at an intensity nearly 100 times stronger in resonance than out of resonance. This field enhancement has found many applications: enhanced photoeffect by SPs, nonlinear effects as the production of second harmonic generation (SHG) in the strong field, surface enhanced Raman scattering (SERS), amplification of light scattered at Rayleigh waves, emission of light from tunnel junctions, etc. Also in fairly thin films, a strong field enhancement has been measured for the high-frequency mode.

This enhancement is correlated with a strong reduction of the reflected light up to a complete transformation of the incoming light into SPs. This reflectivity minimum represents an interesting phenomenon of metal optics on smooth and corrugated surfaces.

The SPs propagating along a corrugated surface decay into light of high intensity on a nonsmooth surface. The measurement of its intensity and its angular distribution allows determination of the roughness parameter, r.m.s. height, and correlation length. Also in normal scattering experiments on rough surfaces the SPs can be excited via the corrugation (grating coupling) and change the angular distribution of the diffusely scattered light. Recent developments of the theory seem to indicate an explanation of these phenomena.

Recent developments have further shown that the very large field enhancement (10^4–10^6) observed in SERS and in SHG are due mainly to localized plasmons; they exist only in very rough surfaces built up of large particles. A chapter is dedicated to the influence of SPs on grating phenomena. Due to the simpler structure of the corrugation, the results sometimes give a more detailed insight into the interaction between the photon and plasmon. The application

of holographic (interference) gratings especially of sinusoidal gratings to which higher harmonics can be added, together with the possibility of varying the grating constant, grating amplitude, and grating material rather simply has given strong impetus to this field.

The author has described the same subject in an earlier article. But in the meantime a number of new results have been reported, which has increased the interest in this subject, so that a more comprehensive account of the behavior of SPs on corrugated surfaces appeared to be desirable.

I have to thank John Simon (Toledo) for a critical reading of the first version of the manuscript. Helpful discussions with Vittorio Celli (Charlottesville) and A.M. Marvin (Trieste) are acknowledged. Additional information from numerous colleagues has been used to answer open questions.

Hamburg, December 1986   *Heinz Raether*

Contents

1. Introduction

Many of the fundamental electronic properties of the solid state can be successfully described by the analogy of single electrons moving in the periodic array of atoms. Another quite different approach to derive the properties of the solid state starts with the plasma concept: the free electrons of a metal are treated as an electron liquid of high density of about $10^{23}\,\mathrm{cm}^{-3}$, ignoring the lattice in a first approximation. From this approach, it follows that longitudinal density fluctuations, plasma oscillations, will propagate through the volume of the metal. The quanta of these "volume plasmons" have an energy $\hbar\omega_{\mathrm{p}} = \hbar\sqrt{4\pi ne^2/m_0}$, where n is the electron density, of the order of $10\,\mathrm{eV}$. They are produced by electrons which are shot into the metal. This exciting phenomenon has been studied in detail theoretically and experimentally with electron-loss spectroscopy.

An important extension of the plasmon physics has been accomplished by the concept of "surface plasmons". Maxwell's theory shows that electromagnetic surface waves can propagate along a metallic surface or on metallic films with a broad spectrum of eigen frequencies from $\omega = 0$ up to $\omega = \omega_{\mathrm{p}}/\sqrt{2}$ depending on the wave vector $\boldsymbol{k}$. Their dispersion relation $\omega(\boldsymbol{k})$ lies right of the light line which means that the surface plasmons have a longer wave vector than light waves of the same energy $\hbar\omega$, propagating along the surface, see Fig. 1.1. Therefore they are called "nonradiative" surface plasmons, which describe fluctuations of the surface electron density. Their electromagnetic fields decay exponentially into the space perpendicular to the surface and have their maximum in the surface, as is characteristic for surface waves.

These surface plasmons have also been studied with electron-loss spectroscopy and with light extensively. The excitation with light needs special light-plasmon couplers (grating coupler, prism coupler), since the dispersion relation lies right of the light line.

This concept of charge fluctuations on the two-dimensional boundary of the solid leads to the question: is it possible to realize a real two-dimensional (2D) free-electron gas? In this case 2D plasmons are expected. It is apparent that these 2D plasmons propagate inside a large frequency band as a function of their wave vector $\boldsymbol{k}$ and obey the dispersion relation $\omega = \sqrt{ak}$, $a = 2\pi n_{\mathrm{s}}e^2/m^*$, where n_{s} is the electron density in the 2D device. This concept has been realized by electrons sprayed on a liquid helium surface. At electron densities of about $10^8\,\mathrm{cm}^{-2}$, 2D plasmons of an energy of $\hbar\omega{\sim}10^{-3}\mathrm{meV}$ have been observed;
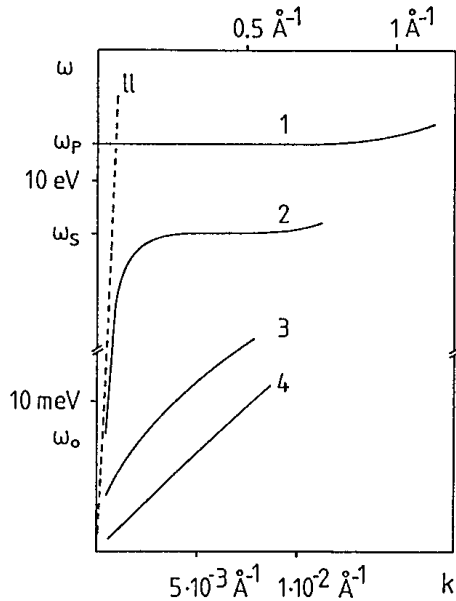
Fig. 1.1. Scheme of the dispersion of plasmons in a solid. *(1)* volume plasmons, *(2)* surface plasmons, *(3)* plasmons in a two-dimensional electron gas, *(4)* plasmons in a one-dimensional system. The upper scale is valid for *(1)* and *(2)*, the scale below for *(3)* and *(4)*. *ll* is the light line

this 2D gas behaves like a classical gas. Another device to realize a 2D gas has been found in a Schottky inversion layer on the surface of a semiconductor, e.g., a $Si-SiO_2$-metal structure. Electron densities of around $10^{12}\,cm^{-2}$ can be produced in Si at the $Si-SiO_2$ boundary, applying an electric field between the metal and the doped Si. In this inversion layer, 2D plasma waves propagate parallel to the boundary. Similar to the case of surface plasmons, the dispersion relation lies right from the light line in Fig. 1.1 so that they can be excited with light only with a grating coupler. Thus, 2D plasmons of an energy $\hbar\omega$ of $\sim 1-10\,meV$ with k-vectors of $\sim 1 - 10 \times 10^{-3}\,Å^{-1}$ have been observed. The low energy of these plasmons allows interaction with other modes of the lattice and thus gives interesting information. Since important technical applications are involved with these devices, this field is developing rapidly.

A further exciting phenomenon has been found: if the electron gas on the helium surface is sufficiently cooled down, the coulomb interaction of the electrons increases compared to their kinetic energy and the electron gas changes into an ordered state (electron lattice).

A further reduction of the dimensionality leads to the 1D electron gas which oscillates along a "quantum wire". The dispersion relation of these 1D plasmons is schematically shown in Fig. 1.1. The detection of these one-dimensional density oscillations is a genuine problem.

This short overview demonstrates the variety of applications of the plasmon concept.

In this article we concentrate on surface plasmons (SPs) which propagate on corrugated surfaces. This restriction, surprising at first, is because a strong electromagnetic field is built up in the surface by the excitation of the SP modes. The corrugation, roughness, or grating structure, acts then as a coupler between this strong SP field and photons, so that the SP field becomes radiative

and a strong light emission results. These processes are significant for numerous interesting experiments as the enhanced light emission from rough or sinusoidal surfaces, or the photoemission enhanced by SPs, the strong Raman scattering (SERS) or the generation of second harmonics in the strong SP field.

The reverse process is also important: if light hits a corrugated surface, SPs are excited via the roughness so that strong electromagnetic fields arise in the surface.

The physics of SPs on corrugated surfaces is described in Chaps. 2–6. Chapter 2 reviews the properties of SPs on smooth boundaries as far as is necessary for the succeeding chapters. In Chap. 3 the results displayed are those obtained at small roughness, r.m.s heigth of 5–10 Å: the resonant light emission due to the coupling of SPs with free electromagnetic waves via the corrugation and the field enhancement in the boundary. The theoretical interpretation is given which allows the derivation of the roughness parameters from the angular distribution of the emitted light. Besides, the radiation scattered into the air space, light "backscattered" into the dielectric part of the ATR (attenuated total reflection) device is demonstrated. In Chap. 4 one finds the results which are obtained at larger roughness: the change of the dispersion relation due to the stronger scattering of the SPs. The theoretical situation is considered. If a roughness structure is used which is built up by islands and by tips, "localized" plasmons can be excited which produce high electric fields. The field which can be determined by measuring the intensity of the second harmonic in the reflected light is of interest also for the discussion of the origin of the Surface Enhanced Raman Scattering (SERS).

Chapter 5 describes the experimental and theoretical facts of light scattering at rough surfaces with the classical light scattering device (no ATR arrangement). At rougher surfaces SPs are excited which change the distribution of the scattered light. In Chap. 6, interesting results are collected which display the effect of a grating on the properties of SPs. Two experimental methods, the ATR device and the grating coupler, are applied. The resonant emission of light is described. It can be theoretically treated with the first-order approximation for smaller values of the amplitudes of the grating. At larger amplitudes, similar to the findings at rougher surfaces, the dispersion relation is changed. Together with a discussion of the enhancement on gratings, the generation of the second harmonic due to the nonlinear susceptibility is demonstrated. Finally the coupling of two plasmons or of wave-guide modes with another plasmon via roughness is demonstrated which leads to a splitting of the dispersion relation.

In the literature the expression "surface plasma polariton" is often used which is identical to the term surface plasmon.

In [Ref. 1.1, Chap. 9], the author has tried to give a review on "Roughness and Surface Plasmons". The following overview is more complete and contains numerous new results, so that a more consistent picture of the present knowledge results. It is hoped that this new attempt is a useful guide for this field.

2. Surface Plasmons on Smooth Surfaces

In this chapter the fundamental properties of SPs are reviewed and thus give the background for Chaps. 3–7.

2.1 Fundamental Properties: Dispersion Relation, Extension and Propagation Length for the Electromagnetic Fields of the Surface Plasmons

Dispersion Relation

The electron charges on a metal boundary can perform coherent fluctuations which are called surface plasma oscillations, *Ritchie* [2.1]. Their existence has been demonstrated in electron energy-loss experiments by *Powell* and *Swan* [2.2]. The frequency ω of these longitudinal oscillations is tied to its wave vector k_x by a dispersion relation $\omega(k_x)$. These charge fluctuations, which can be localized in the z direction within the Thomas-Fermi screening length of about $1\,\text{Å}$, are accompanied by a mixed transversal and longitudinal electromagnetic field which disappears at $|z| \to \infty$, Fig. 2.1, and has its maximum in the surface $z = 0$, typical for surface waves. This explains their sensitivity to surface properties. The field is described by

$$E = E_0^{\pm} \exp\left[+ i(k_x x \pm k_z z - \omega t)\right] \tag{2.1}$$

with $+$ for $z \geq 0$, $-$ for $z \leq 0$, and with imaginary k_z, which causes the exponential decay of the field E_z. The wave vector k_x lies parallel to the x direction; $k_x = 2\pi/\lambda_{\mathrm{p}}$, where λ_{p} is the wavelength of the plasma oscillation. Maxwell's
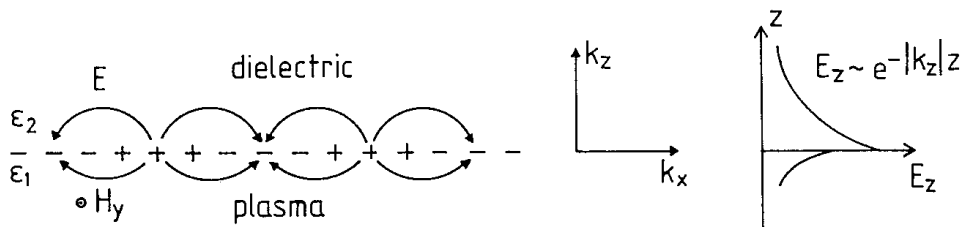

Fig. 2.1. The charges and the electromagnetic field of SPs propagating on a surface in the x direction are shown schematically. The exponential dependence of the field E_z is seen on the right. H_y shows the magnetic field in the y direction of this p-polarized wave

equations yield the retarded dispersion relation for the plane surface of a semi-infinite metal with the dielectric function ($\varepsilon_1 = \varepsilon_1' + i\varepsilon_1''$), adjacent to a medium ε_2 as air or vacuum:

$$D_0 = \frac{k_{z1}}{\varepsilon_1} + \frac{k_{z2}}{\varepsilon_2} = 0 \qquad \text{together with} \tag{2.2}$$

$$\varepsilon_i \left(\frac{\omega}{c}\right)^2 = k_x^2 + k_{zi}^2 \quad \text{or} \tag{2.3}$$

$$k_{zi} = \left[\varepsilon_i \left(\frac{\omega}{c}\right)^2 - k_x^2\right]^{1/2}, \quad i = 1, 2 \ .$$

The wave vector k_x is continuous through the interface (for the derivation see Appendix I). The dispersion relation (2.2) can be written as

$$k_x = \frac{\omega}{c} \left(\frac{\varepsilon_1 \varepsilon_2}{\varepsilon_1 + \varepsilon_2}\right)^{1/2} \ . \tag{2.4}$$

If we assume besides a real ω and ε_2 that $\varepsilon_1'' < |\varepsilon_1'|$, we obtain a complex $k_x = k_x' + ik_x''$ with

$$k_x' = \frac{\omega}{c} \left(\frac{\varepsilon_1' \varepsilon_2}{\varepsilon_1' + \varepsilon_2}\right)^{1/2} \tag{2.5}$$

$$k_x'' = \frac{\omega}{c} \left(\frac{\varepsilon_1' \varepsilon_2}{\varepsilon_1' + \varepsilon_2}\right)^{3/2} \frac{\varepsilon_1''}{2(\varepsilon_1')^2} \ . \tag{2.6}$$

For real k_x' one needs $\varepsilon_1' < 0$ and $|\varepsilon_1'| > \varepsilon_2$, which can be fulfilled in a metal and also in a doped semiconductor near the eigen frequency; k_x'' determines the internal absorption, see below. In the following we write k_x in general instead of k_x'.

The dispersion relation, see Fig. 2.2, approaches the light line $\sqrt{\varepsilon_2}\omega/c$ at small k_x, but remains larger than $\sqrt{\varepsilon_2}\omega/c$, so that the SPs cannot transform into light: it is a "nonradiative" SP, see below. At large k_x or

$$\varepsilon_1' \rightarrow -\varepsilon_2 \tag{2.7}$$

the value of ω approaches

$$\omega_{\text{sp}} = \left(\frac{\omega_{\text{p}}}{1 + \varepsilon_2}\right)^{1/2} \tag{2.8}$$
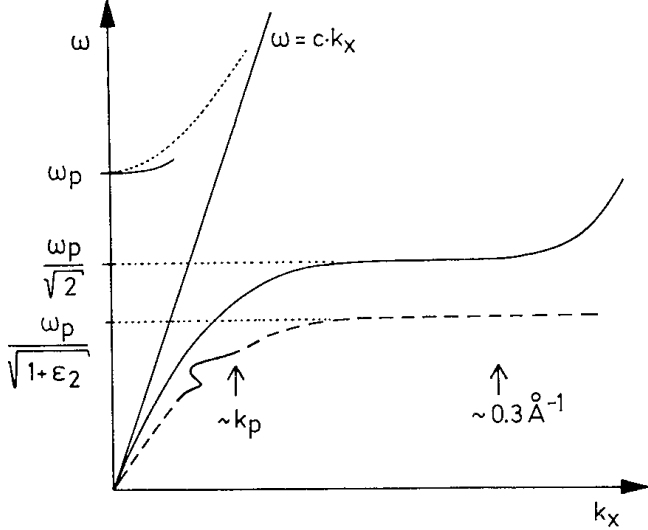
5

Fig. 2.2. The dispersion relation of nonradiative SPs (——), right of the light line $\omega = ck_x$; the retardation region extends from $k_x = 0$ up to about $k_p = 2\pi/\lambda_p$ (λ_p plasma wavelength). The dashed line, right of $\omega = ck_x$, represents SPs on a metal surface coated with a dielectric film (ε_2). Left of the light line, $\omega(k_x)$ of the radiative SPs starts at ω_p (——). (The dotted line represents the dispersion of light in a metal: $\omega/k_x = c/|\varepsilon_1'|^{1/2}$ or in the case of free electrons $\omega^2 = \omega_p^2 + c^2 k_x^2$.) The slight modulation in the dashed dispersion curve comes from an eigen frequency in a monomolecular dye film deposited on a Langmuir-Blodgett film (ε_2). The latter depresses $\omega_p/\sqrt{2}$ to $\omega_p/\sqrt{1 + \varepsilon_2}$

for a free electron gas where ω_p is the plasma frequency $\sqrt{4\pi n e^2/m}$, with n the bulk electron density. With increasing ε_2, the value of ω_{sp} is reduced.

At large k_x the group velocity goes to zero as well as the phase velocity, so that the SP resembles a localized fluctuation of the electron plasma.

Spatial Extension of the SP Fields

Wave vectors k_{z2} and k_{z1} are imaginary due to the relations $\omega/c < k_x$ and $\varepsilon_1' < 0$, see (2.3), so that, as mentioned above, the field amplitude of the SPs decreases exponentially as $\exp(-|k_{zi}||z|)$, normal to the surface. The value of the (skin) depth at which the field falls to $1/e$, becomes

$$\hat{z} = \frac{1}{|k_{zi}|} \quad \text{or} \tag{2.9}$$

$$\text{in the medium with } \varepsilon_2: \quad \hat{z}_2 = \frac{\lambda}{2\pi}\left(\frac{\varepsilon_1' + \varepsilon_2}{\varepsilon_2^2}\right)^{1/2}$$

$$\text{in the metal with } \varepsilon_1: \quad \hat{z}_1 = \frac{\lambda}{2\pi}\left(\frac{\varepsilon_1' + \varepsilon_2}{\varepsilon_1'^2}\right)^{1/2}. \tag{2.10}$$

For $\lambda = 6000\,\text{Å}$ one obtaines for silver $\hat{z}_2 = 3900\,\text{Å}$ and $\hat{z}_1 = 240\,\text{Å}$, and for gold $2800\,\text{Å}$ and $310\,\text{Å}$, respectively.

At large k_x, $\hat{z}_i$ is given by about $1/k_x$ leading to a strong concentration of the field near the surface in both media.

At low k_x or large $|\varepsilon_1'|$ values, the field in air has a strong (transverse) component E_z compared to the (longitudinal) component E_x, namely $E_z/E_x = -i|\varepsilon_1'|^{1/2}$ and extends far into the air space; it resembles thus a guided photon field (Zenneck-Sommerfeld wave). In the metal, E_z is small against E_x since $E_z/E_x = i|\varepsilon_1'|^{-1/2}$. These relations are derived from $\text{div} E = 0$, valid outside the surface air/metal. At large k_x both components E_x and E_z become equal: $E_z = \pm i E_x$ (air: $+i$, metal: $-i$).

Propagation Length of the SPs

The intensity of SPs propagating along a smooth surface decreases as $e^{-2k_x''x}$ with k_x'' from (2.6). The length L_i after which the intensity decreases to $1/e$ is then given by

$$L_i = (2k_x'')^{-1} \ .$$ (2.11)

In the visible region, L_i reaches the value of $L_i = 22\,\mu$ in silver at $\lambda = 5145\,\text{Å}$ and $L_i = 500\,\mu$ (0.05 cm) at $\lambda = 10\,600\,\text{Å}$. The absorbed energy heats the film, and can be measured with a photoacoustic cell, see Sect. 2.3.

Instead of regarding the spatial decay of the SPs along the coordinate x, the temporal decay time T_i can be of interest. The values of L_i and T_i are correlated by $L_i = T_i v_g$ with v_g the group velocity. Assuming a complex $\omega = \omega' - i\omega''$ and real k_x', with $T_i = 2\pi/\omega''$, we obtain from (2.4)

$$\omega'' = k_x' c \frac{\varepsilon_1''}{2(\varepsilon_1')^2} \frac{\varepsilon_1' \cdot \varepsilon_2}{\varepsilon_1' + \varepsilon_2}$$

$$\omega' = k_x' c \frac{\varepsilon_1' + \varepsilon_2}{\varepsilon_1' \varepsilon_2}^{1/2} \ .$$ (2.12)

More detailed information on SPs can be found in [2.3–5].

2.2 Excitation of Surface Plasmons by Electrons and by Light

Excitation by Electrons

Electrons penetrating a solid transfer momentum $\hbar q$ and energy ΔE_0 to the electrons of the solid. The projection of q upon the surface of the film k_x determines the wave vector and, together with the dispersion relation, the energy loss of the scattered electron $\Delta E = \hbar\omega$, see Fig. 2.3. Since the electrons are scattered at different angles θ, they transfer different momenta $\hbar k_x = \hbar k_{el}' \sin\theta \cong \hbar k_{el}\theta$ with $k_{el} = 2\pi/\lambda_{el}$. If one observes the energy loss $\Delta E = \hbar\omega$ at an increasing angle θ (or smaller λ_{el}) the dispersion relation of the SPs can be measured up to large k_x beyond the Brillouin zone. The physics of SPs has thus been studied intensively with electrons, especially with fast electrons, and the fundamen-

7
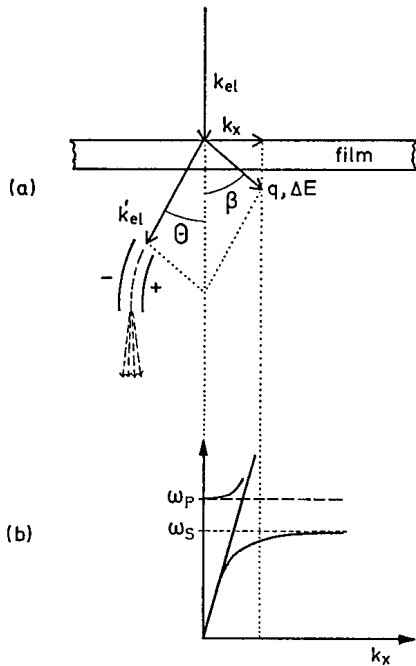
Fig. 2.3. Excitation of SPs by electrons in transmission of thin films. k_{el}, k'_{el} wave vector of the incoming resp. scattered electron; q wave vector transferred to the film; its projection on the surface k_x and the dispersion relation determine the energy $\hbar\omega$ of the SPs. The choice of $\theta(k'_{el})$ fixes k_x and thus ω. From [2.3b]

tal properties of SPs have been found in good agreement with the theoretical concept [2.3b].

Fast electrons are a good tool with which to study the dispersion relation at larger k_x ($k_x > \omega_p/c$), e.g., measurements up to $k_x \sim 0.3\,\text{Å}^{-1}$ have been performed in order to study the slow increase of the dispersion relation of SPs in Al [2.3,6]. However, it is not convenient to reach the region of small k_x with electrons, fast or slow, since the aperture of the electron beam cannot be sufficiently reduced due to intensity reasons: A value of the aperture of 5×10^{-5} rad with $\lambda_{el} = 0.05\,\text{Å}$ (50KeV) gives an experimental k_x width (Δk_x) of $3 \times 10^{-3}\,\text{Å}^{-1}$ which is comparable with the extension of the whole retarded region of the dispersion relation. This demonstrates that fast and slow electrons are not suitable, as yet, for studying the SP properties at very low k_x values. The reverse is valid for light: a laser beam with a divergence of 10^{-3} rad at 6000 Å gives a Δk_x of about $10^{-6}\,\text{Å}^{-1}$ and allows thus to probe the SP dispersion relation down to very low k_x values. It has not yet been possible to reach the region of larger k_x with photons.

Excitation by Light

The application of photons to excite SPs meets the difficulty that the dispersion relation lies right from the light line ($k_x > \omega/c$). At a given photon energy $\hbar\omega$ the wave vector $\hbar\omega/c$ has to be increased by a Δk_x value in order to "transform" the photons into SPs. There are two methods:

a) Grating Coupler. If light ($k = \omega/c$) hits a grating with a grating constant a, at an angle θ_0 its component in the surface can have wave vectors
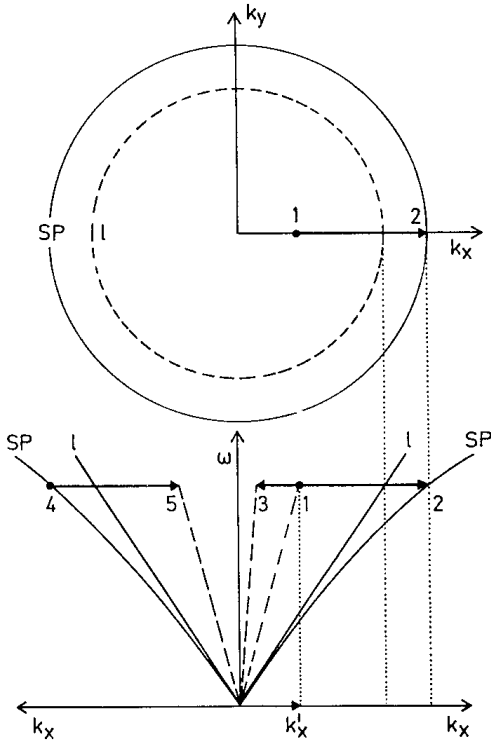
$(\omega/c)\sin \theta_0 \pm \nu g$ with ν an integer and $g = 2\pi/a$. The dispersion relation (2.4) can then be fulfilled by the sum

$$k_x = \frac{\omega}{c}\sin \theta_0 \pm \nu g = \frac{\omega}{c}\sqrt{\frac{\varepsilon}{\varepsilon + 1}} = k_{\mathrm{sp}} \ ,$$

or more generally

$$k_x = \frac{\omega}{c}\sin \theta_0 \pm \Delta k_x = k_{\mathrm{sp}} \tag{2.13}$$

where Δk_x, in Fig. 2.4 the vector 1–2, stems from any perturbation in the smooth surface; $\Delta k_x = 0$ gives no solution of the dispersion relation (2.4).

Fig. 2.4. The grating coupler. SP: dispersion relation of SPs, l : light line. The incoming light, wave vector k'_x, point (1) is transformed into a SP, point (2), by taking up Δk_x. The interaction $1{\to}3$ via roughness leads to light scattered inside the light cone. The process $4{\to}5$ describes the decay of a SP into light via Δk_x; it is the reverse of $1{\to}2$. Upper part: the full circle represents the values of $|k| = (k_x^2 + k_y^2)^{1/2}$ and the light circle (dashed circle) at $\omega = $ const. in the two-dimensional k space

The resonance can be observed as a minimum of the reflected light, see Fig. 6.8.

The reverse takes place too: SPs propagating along a grating or a rough surface can reduce their wave vector k_x by Δk_x so that the SP is transformed into light, see Fig. 2.4, arrow $4{\to}5$, and Fig. 2.5. This light emission, a consequence of the photon-SP coupling via roughness, plays an important role.

Correlated experiments have been reported by *Teng* and *Stern* [2.7]. This radiation can be used as detector for SPs: If the SP is excited to its maximum
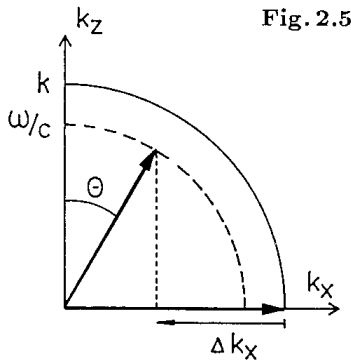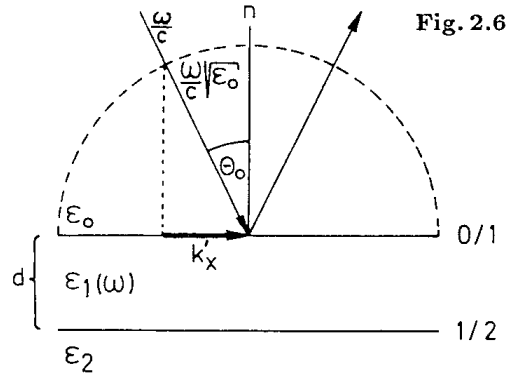
Fig. 2.5. Transformation of the SPs of wave vector k_x into photons by losing Δk_x to the rough surface and by taking up k_z from the surface, so that the relation $(\omega/c)^2 = (k_x - \Delta k_x)^2 + k_z^2$ is fulfilled; in the case of a grating: $\Delta k_x = g$

Fig. 2.6. Reflection of light at a metal surface $[\varepsilon_1(\omega)]$. The medium above the metal is a dielectric medium (ε_0) as glass or quartz; below the metal is air or a vacuum (ε_2). From [2.3a,b]

value, the emitted intensity passes a maximum too, see Fig. 3.1 (scattering device) [2.8,9].

b) ATR Coupler. If light is reflected at a metal surface covered with a dielectric medium $(\varepsilon_0 > 1)$ e.g., with a quartz half cylinder, its momentum becomes $(\hbar\omega/c)\sqrt{\varepsilon_0}$ instead of $\hbar\omega/c$ and its projection on the surface, see Fig. 2.6,

$$k_x = \sqrt{\varepsilon_0}\frac{\omega}{c} \sin \theta_0 \ . \tag{2.14}$$

The dispersion relation (2.4) for SPs propagating on the interface $\varepsilon_2/\varepsilon_1$ (air/ metal) can thus be satisfied between the lines c, beyond which limit total reflection at an interface $0/1$ takes place, and $c/\sqrt{\varepsilon_0}$, see Fig. 2.7. The excitation
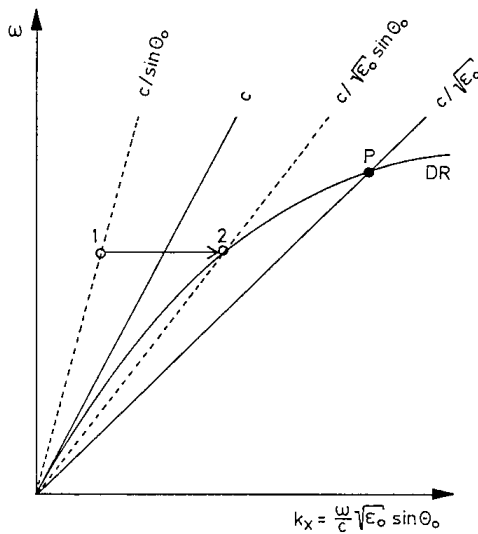
Fig. 2.7. The ATR method: Dispersion relation DR of SPs for a quartz/metal/air system $\varepsilon_2 = 1$, c : light line in vacuum, $c/\sqrt{\varepsilon_0}$: light line in the medium ε_0. Since the light line $c/\sqrt{\varepsilon_0}$ lies to the right of the DR up to a certain k_x, light can excite SPs of frequencies ω below the crossing point P on the metal/air side. The SPs on the interface $0/1$ metal/quartz cannot be excited, since their DR lies to the right of $c/\sqrt{\varepsilon_0}$ because $\varepsilon_0 > 1$

10

is recognized as a minimum in the (totally) reflected intensity (ATR minimum [2.10]).

Another way to understand the formation of SPs in this device: Since the excitation of SPs occurs in the region of total reflection at the interface quartz/metal, an evanescent light wave with a phase velocity $v = \omega/k_x = c/(\sqrt{\varepsilon_0}\sin\theta_0)$ with $\sqrt{\varepsilon_0}\sin\theta_0 > 1$ propagates in the interface with $v \leq c$. The resonance condition for SPs

$$\omega/k_x^0 = c\sqrt{\frac{\varepsilon+1}{\varepsilon}} = c/(\sqrt{\varepsilon_0}\sin\theta_0) \qquad (2.15)$$

can thus be fulfilled, particularly because the character of both waves is the same.

Two devices are possible: in Fig. 2.8 (a) the metal surface is separated by an air or dielectric slit at a distance of about λ from the medium ε_0 (glass or quartz). The evanescent field couples with the SP on the 1/2 interface [2.10]; in (b) the metal film (ε_1) with a thickness of several 10^2 Å contacts the medium ε_0. The electromagnetic field decreases exponentially in the film and excites the SPs on the 1/2 interface [2.8,11]. The experiments described in this book are made with the device (b) (Kretschmann-Raether configuration). The objections to this device are due to an error [2.12]. The Otto configuration (a) is well adapted to surfaces which would not be damaged or touched by the prism. This is important e.g., for studying surface phonon polaritons on single crystal surfaces.

The quantitative description of the minimum of the reflected intensity R can be given by Fresnel's equations for the three-layer system 0/1/2: 0 dielectric medium, e.g., quartz or glass; 1 metal film of thickness d; 2 dielectric, e.g., air, vacuum, etc. The reflectivity R for p-polarized light, with E_0 the incoming and E_r the reflected field, is given by
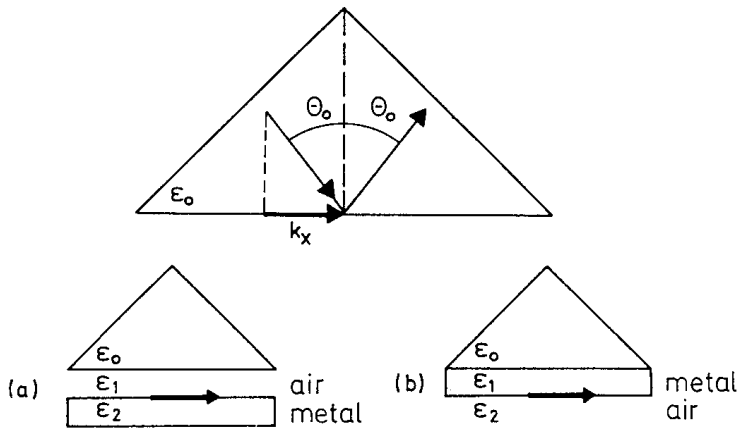
Fig. 2.8a,b. Configuration of the ATR method. (a): The dielectric (air) lies between the prism and the metal surface, Otto configuration. (b): The metal contacts the prism and couples the SPs with the evanescent field of the totally reflected light wave, Kretschmann-Raether configuration. From [2.3a]

$$R = |r_{012}^p|^2 = \left|\frac{E_r^p}{E_0^p}\right|^2 = \left|\frac{r_{01}^p + r_{12}^p \exp\left(2ik_{z1}d\right)}{1 + r_{01}^p r_{12}^p \exp\left(2ik_{z1}d\right)}\right|^2 \quad \text{with} \tag{2.16}$$

$$r_{ik}^p = \left(\frac{k_{zi}}{\varepsilon_i} - \frac{k_{zk}}{\varepsilon_k}\right)\bigg/\left(\frac{k_{zi}}{\varepsilon_i} + \frac{k_{zk}}{\varepsilon_k}\right) . \tag{2.17}$$

Under the special conditions $|\varepsilon_1'| \gg 1$ and $|\varepsilon_1''| \ll |\varepsilon_1'|$ this dependence can be approximated in the region of the resonance by the Lorentzian type relation [2.11], which reveals its physical meaning:

$$R = 1 - \frac{4\Gamma_i \Gamma_{\mathrm{rad}}}{\left[k_x - (k_x^0 + \Delta k_x)\right]^2 + (\Gamma_i + \Gamma_{\mathrm{rad}})^2} \tag{2.18}$$

with k_x given by (2.14) and k_x^0 by (2.15). The resonance wave vector $(k_x^0 + \Delta k_x)$ is different from (2.4), which is valid only for a semi-infinite metal; here we have a finite metal film of thickness d_1 between two dielectrica. The term Δk_x can be approximated for $\exp\left(2ik_x d_1\right) \ll 1$ by

$$\Delta k_x = \left[\frac{\omega}{c}\frac{2}{1 + |\varepsilon_1'|}\left(\frac{|\varepsilon_1'|}{|\varepsilon_1'| - 1}\right)^{3/2}\exp\left(-2|k_x^0|d_1\right)\right]r_{01}^p(k_x^0) \quad \text{or} \tag{2.19}$$

$$\Delta k_x = \mathrm{const}.\, r_{01}^p(k_x^0) . \tag{2.20}$$

Its real part causes a displacement of the resonance position compared to k_x^0 (2.5),

$$\mathrm{Re}\left\{\Delta k_x\right\} = \mathrm{const}.\,\mathrm{Re}\left\{r_{01}^p(k_x^0)\right\} . \tag{2.21}$$

Its imaginary part gives an additional damping term

$$\mathrm{Im}\left\{\Delta k_x\right\} = \Gamma_{\mathrm{rad}} = \mathrm{const}.\,\mathrm{Im}\left\{r_{01}^p(k_x^0)\right\} \tag{2.22}$$

to the internal damping

$$\Gamma_i = \mathrm{Im}\left\{k_x^0\right\} . \tag{2.23}$$

r_{01}^p is given by (2.17). For details see Appendix III. Equation (2.18) demonstrates that R passes a minimum which is zero for

$$\Gamma_i = \Gamma_{\mathrm{rad}} . \tag{2.24}$$

This matching condition fixes, as (2.22) and (2.23) show, the thickness d_{min} of the metal film at a given λ. For example at $\lambda = 5000\,\text{Å}$ a silver film gives $R = 0$ at $d_{\mathrm{min}} = 550\,\text{Å}$. The value of d_{min} depends on the dielectric function ε. Since it is not known exactly, d_{min} varies at least by 10 %.
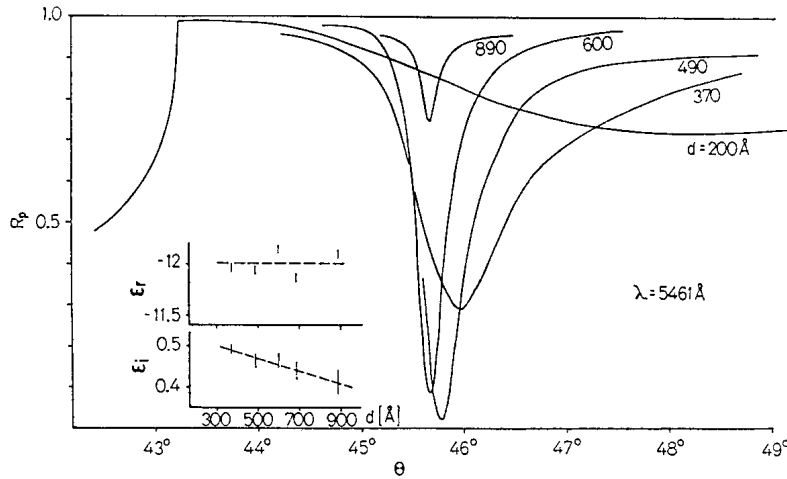
Fig. 2.9. Reflection at silver films of different thickness measured with an ATR device. $\lambda =$ 5461 Å. *Inset:* the dielectric function $(\varepsilon', \varepsilon'')$ derived from these curves. Observed data [2.11]

Figure 2.9 demonstrates the effect of a variation of d_1 at constant λ on the position of the ATR minimum, its shape and its height [2.11]. In this case Γ_{rad} changes, whereas Γ_{i} remains constant.

The energy conservation requires: $R + A + T = 1$, the sum of the relative reflection, absorption and transmission. Since $T = 0$ and, at d_{min}, $R = 0$, A becomes 1, i.e., the whole energy is absorbed in the metal film.

A comment on the reflectivity given by (2.18) shall be added, since the physics giving rise to the reflectivity minimum are in general not discussed.

The light wave, having passed the hemicylinder (ε_0), is partially reflected at the interface 0/1. Partially it traverses the silver film (of thickness d_1) as a exponentially decaying wave. At the interface 1/2 it induces excitations which radiate light back into the silver film. If the thickness d_1 increases, the back-scattered field disappears due to $\Gamma_{\text{rad}} \rightarrow 0$, so that R approaches the value unity (more exactly a value just below unity, see Appendix II).

For decreasing thickness d_1 the back-scattered field increases. Since it is in antiphase with the incoming wave, see (2.18), the two interfere destructively thus reducing R. At $d_1 = d_{\text{min}}$ they even compensate each other and R becomes zero.

The antiphase radiation field, captured in the metal film, is converted into heat. In the resonance case $R = 0$ the total damping amounts to $2\Gamma_{\text{i}}$. This value determines the half-width of the reflection minimum. A further decrease of d_1 leads to increasing Γ_{rad} and has the effect that R assumes again a value close to unity.

More details and derivation of (2.18–24) are given in Appendix II.

The same matching phenomenon as above is observed in the reflection of light at gratings and rough surfaces, see Chaps. 3 and 6.

13

2.3 Internal and Radiation Damping

The two damping processes on a smooth surface can be measured separately.

Internal Damping

The internal absorption is given by k_x'' (2.6). The electromagnetic field of the SPs excites electron-hole pairs at the Fermi level; the following de-excitation produces phonons and thus heating. The energy can be lost also by the emission of photoelectrons, if $\hbar\omega >$ work function; this is not the case with silver, except that a very thin film of cesium (a few Å) decreases the work function of silver from 4.5 eV to <2 eV, so that a strong photoemission is observed in case of SP resonance [2.13]. The heat can be measured with a photoacoustic cell: chopping the incoming light, the periodic heating of the silver film can be registered by the periodic pressure variations in a microphone [2.14a]. Such a photoacoustic signal is seen in Fig. 2.10 [2.14b]. It can be compared to the reflection signal R above it. It has been shown that the energy lacking in the reflected light is measured with the photoacoustic cell as heat energy in the silver film; the power lost by light decaying from SPs can be detected, it is however below the limit of measurements at rather smooth surfaces, e.g., at $\delta \sim 5$ Å.
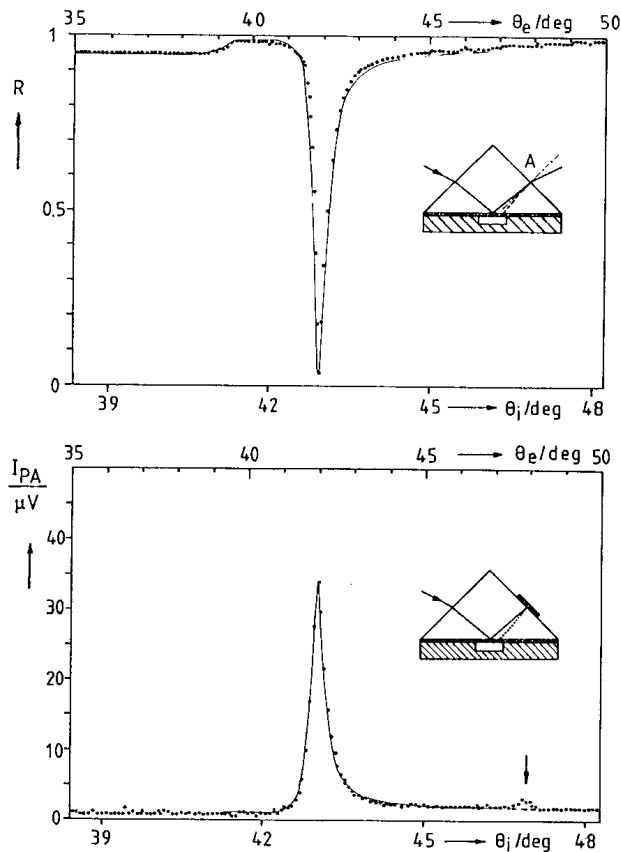
Fig. 2.10. The ATR minimum at a silver film (500 Å thick) above, is compared to the signal in a photoacoustic cell which indicates the absorbed power (Joule heat) in the silver film, below. The non-reflected power is found as heat in the metal film. From [2.14b]

Radiation Damping

If SPs propagate in the smooth interface 2/1, air/metal, see Fig. 2.6, and a dielectric material $\varepsilon_0 > 1$ contacts the thin metal film from the other side as in an ATR device, the SPs, an evanescent wave, with the imaginary k_{z1} (2.3)

$$k_{z1} = \left[\varepsilon_1\left(\frac{\omega}{c}\right)^2 - k_x^2\right]^{1/2} \quad \text{with} \quad \varepsilon_1 < 0$$

transform in the medium ε_0 into a plane wave due to the real k_{z2}, since $k_x \leq \sqrt{\varepsilon_0}\omega/c$. This leads to the radiation damping, characteristic for an asymmetric two-interface system.

This back-coupled radiation loss can be observed, if, e.g., as in Fig. 2.11, SPs are produced by electrons in the interface 2/1. These SPs radiate into the ε_0 space. Figure 2.11 shows, besides the negligible four lobes of the transition radiation, produced at the interface 2/1 which are of no interest here, strong needle-like light beams [2.15]. This radiation produces a light circle around the normal of the surface and has been observed on Al films [2.16].

In the ATR device this back-coupled light interferes with the incoming light at the boundary quartz/metal destructively, so that in case of $R = 0$ no photons leave the quartz cylinder and the incoming light power is transformed into heat $(A = 1)$.

If however the metal surface metal/air is rough, this light can be observed: If the SPs are scattered out of the plane of incidence, they are decoupled with
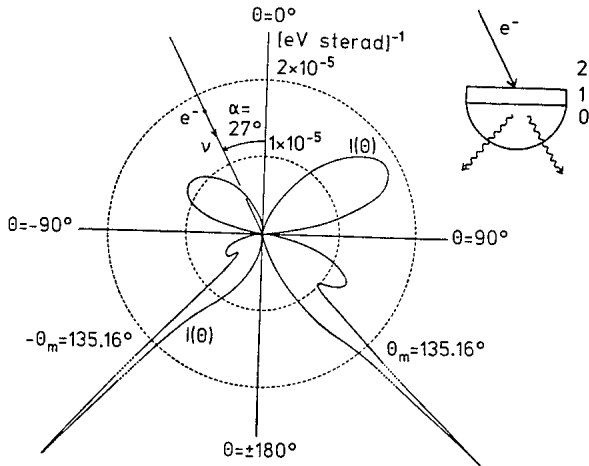
Fig. 2.11. Calculated radiation damping of SPs propagating on a smooth surface (2/1) of a thin silver film (1) (600 Å thick). Electrons of 25 KeV excite the SPs. These SPs, which emit light into the dielectric (ε_0) produce two intense needle-like plasma radiation peaks ($\lambda = 5000$ Å) of an angular width of $0.4°$ and an intensity of about 100 times stronger than the four lobes of the transition radiation. The two needles result from electrons scattered into the two angles $\pm\theta$, see Fig. 2.3. Since the electrons are scattered into a bundle of directions, an intense light circle around the film normal is produced. From [2.15a]

respect to the phase and emit light under the reflection angle θ_0 into a circle around the normal of the surface, see Fig. 3.10. This light can be used to derive the roughness parameters of the surface, see Chap. 3.

Damping by Single Particle Excitation

Since the wave vector k_z perpendicular to the surface, is not fixed so that a continuum of k_z is disposable for interaction processes, a strong coupling of SPs with the electron-hole pairs should be possible, since momentum conservation can be fulfilled. However, as yet there is no indication of this damping process. For example, the position and the half width of the surface loss of indium measured with electron-loss spectroscopy has been compared with the values calculated from optical constants obtained by ellipsometric measurements under clean vacuum conditions; they showed good agreement at least within some percentage points [2.17]. Since the optical constants are derived from bulk properties and therefore are not influenced by the damping just mentioned, one can assume that this type of damping is not important, at least in In. It is still an open question as to why this coupling is weak.

2.4 Field Enhancement Due to Surface Plasmons

If the reflectivity R has its lowest value, the intensity of the electromagnetic field reaches its maximum in the surface, see Fig. 2.12. The value of the enhancement is given by the ratio of the field intensitiy on the metal surface at the air side ($\varepsilon_2 = 1$), given by $|H_y(2/1)|^2$ (H_y the magnetic field of the SPs) divided by the incoming field intensity $|H_{y0}(0/1)|^2$ in the medium ε_0, e.g., quartz (ε_0), for p-polarized light [2.18]:

$$\frac{|H_y(2/1)|^2}{|H_{y0}(0/1)|^2} = |t^p_{012}|^2 = \frac{t^p_{01} t^p_{12} \exp\left(i k_{z1} d_1\right)}{1 + r_{01} r_{12} \exp\left(2 i k_{z1} d_1\right)} \ , \tag{2.25}$$

where $|t^p_{012}|^2$ represents Fresnel's transmission coefficient for a two-boundary system; t^p_{ik} are the corresponding coefficients for an one-boundary system. The following correlation is applicable:

$$t^p_{ik} = 1 + r^p_{ik} \ , \tag{2.26}$$

for r^p_{ik} see (2.17).

Equation (2.25) can be developed similarly for $|r^p_{012}|^2$, see (2.18), and thus demonstrates its resonance character, see Fig. 2.13. With d as parameter, $|t^p_{012}|^2$ as a function of the angle of incidence has a strong maximum at $d = d_{\min}$ which comes out as
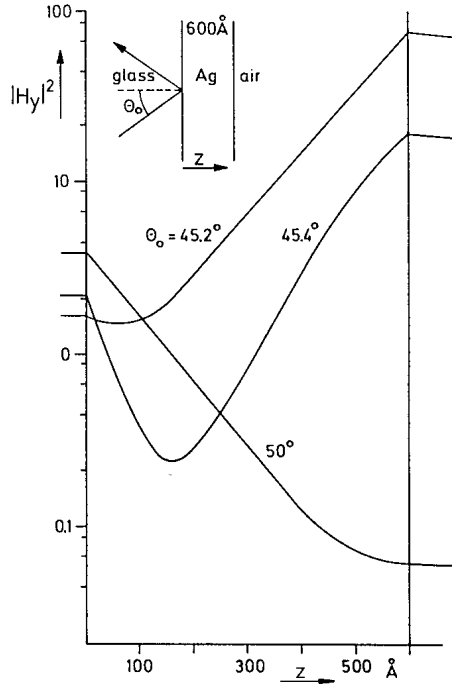
Fig. 2.12. Density of the relative electromagnetic energy $|H_y|^2$ as a function of the distance from the medium (ε_0), glass or quartz, in z direction. Thickness of the silver film: 600 Å. Parameter: θ_0 angle of incidence. $\theta_0 = 45.2°$ equals the resonance angle for $\lambda = 6000$ Å and shows the maximum enhancement. The spatial shape of the field intensity in resonance and out of it is demonstrated. It shows the exponential decay of the surface waves at both interfaces. From [2.3a,18]

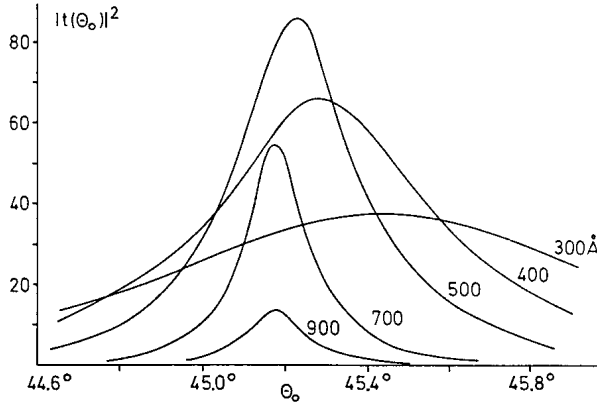**Fig. 2.13.** The enhancement factor $|t^p|^2$ of silver $\lambda = 6000$ Å for different thickness d. The maximum is reached at $\Gamma_i = \Gamma_{\mathrm{rad}}$ (internal damping = radiation damping). Γ_{rad} varies with $\exp(-2dk_x^0)$. From [2.18]

$$|t^p_{012}|^2_{\max} = \frac{1}{\varepsilon_0} \frac{2|\varepsilon_1'|^2}{\varepsilon_1''} \frac{a}{1 + |\varepsilon_1'|} \qquad \text{using} \qquad (2.27)$$

$$|t^p_{01}|^2_{\max} = \frac{4a^2}{a^2 + \varepsilon_0^1} \quad \text{and} \quad a^2 = |\varepsilon_1'|(\varepsilon_0 - 1) - \varepsilon_0 \ . \qquad (2.28)$$

17

In general one is interested in the maximum enhancement of the *electric*-field intensity which is obtained from

$$\left(\frac{|H_y(2/1)|^2}{|H_{y,0}(0/1)|^2}\right)_{\text{max}} = \frac{\varepsilon_2}{\varepsilon_0}\left(\frac{|E(2/1)|^2}{|E_0(0/1)|^2}\right)_{\text{max}} = \frac{\varepsilon_2}{\varepsilon_0}T_{\text{max}}^{\text{el}} \qquad \text{as} \qquad (2.29)$$

$$T_{\text{max}}^{\text{el}} = \frac{1}{\varepsilon_2}\frac{2|\varepsilon_1'|^2}{\varepsilon_1''}\frac{a}{1+|\varepsilon_1'|} \qquad (2.30)$$

with $a^2 = |\varepsilon_1'|(\varepsilon_0 - 1) - \varepsilon_0$ [2.19].

If $\varepsilon_2 = 1$ (air) and $\varepsilon_0 = 2.2$ (quartz) one calculates for silver at $\lambda = 4500$ Å: $T_{\text{max}}^{\text{el}} \approx 100$; at $\lambda = 6000$ Å: $T_{\text{max}}^{\text{el}} \approx 200$, and at $\lambda = 7000$ Å: $T_{\text{max}}^{\text{el}} \approx 250$; the dielectric function $\varepsilon(\omega)$ is taken from [2.20]. At $\lambda = 6000$ Å a $T_{\text{max}}^{\text{el}}$ of about 30 is obtained for gold, whereas values for Al of about 40 and Cu of about 7 are obtained. Since the experimental values of the dielectric function $\varepsilon_1(\omega)$, especially ε_1'', are very sensitive to the experimental conditions (see the appendix in [2.21]), the values of $T_{\text{max}}^{\text{el}}$ are approximate data. The ε value of Al has been taken from [2.22].

It depends on the problem as to which of these terms is needed. For example, $|t_{012}^p|^2$ appears in (3.1) for the light emission emitted from SPs propagating on rough surfaces, whereas T_{el} is of interest for the second harmonic generation, see Sect. 2.8.

If one refers the intensity $|E(2/1)|^2$ not to the incoming intensity in quartz, but to that in air, before the light enters the quartz, we get $T_{\text{max}}^{\text{el}} = |t_{012}^p|^2$ which is smaller than that of (2.30).

The enhancement, at least its maximum amount, can be derived in an obvious manner by applying energy conservation [2.23]. The Poynting vector $P(x)$ of the SPs, integrated over z from $-\infty$ up to $+\infty$, contains the field intensity $|E_{\text{sp}}(0^+)|^2$ of the SPs just at the metal surface. We wish to calculate $|E_{\text{sp}}(0)^+|^2$ at the surface air/metal in air. At resonance or $R = 0$ the power of the SPs is lost exclusively by internal absorption in the metal or

$$-\frac{dP(x)}{dx} = 2k_x''P(x) \qquad (2.31)$$

with k_x'', according to (2.6). This loss is compensated for by the power of the incoming light $|E_0|^2$ which radiates on the unit surface area. Both have to be equal in the steady state. Thus one obtaines the quotient $|E_{\text{sp}}(0^+)|^2/|E_0|^2$ as a function of the experimental parameters as the angle of incidence, the dielectric function, etc. This is helpful especially in the case of the grating coupler, see Chap. 6.

2.5 Determination of $\varepsilon(\omega)$ In Situ
Using the ATR Minimum

For a series of evaluations the knowledge of $\varepsilon(\omega)$ is needed. Since these data show fluctuations due to unknown preparation conditions, see e.g., the comparison of $\varepsilon(\omega)$ of silver and gold in the appendix of [2.21], it is therefore important that the reflection minimum allows determination of $\varepsilon(\omega)$ of the film surface in situ very accurately. By fitting Fresnel's equation (2.18) with the observed ATR curve, ε_1', ε_1'', and d of the metal film can be obtained very accurately without using values given in the literature [2.11]. This method has been applied to determine $\varepsilon(\omega)$ of Ag [2.11], Li, Na [2.24], Cu [2.25], Au [2.25,26], Al [2.22], LiF [2.26]. A discussion of the method is also given in [2.27]. The measurements on lithium and sodium have been made in a special UHV device at pressures of 2×10^{-9} Torr [2.24]. An experimental arrangement for high vacuum work is described in [3.6].

In the appendix values of $\varepsilon(\omega)$ of silver, gold and aluminum are collected and compared with each other.

2.6 Coating of the Metal Surface with a Dielectric Film; Thickness Dispersion of Surface Plasmons

Coating, Without a Particular Eigen Frequency
In many experiments the metal surface is covered with a thin, dielectric film which reduces the frequency of the SPs by the polarization of the dielectricum produced by the oscillating charges as given in (2.8), for very large k_x and very thick films.

In general we have to deal with finite k_x values and thin dielectric films. Therefore we discuss here the behavior of the SP frequency as a function of k_x, starting with the bare metal surface and depositing thicker dielectric films.

Such investigations which demonstrate the "thickness dispersion" have already been performed with the methods of electron-loss spectroscopy [2.36]. In the light-line region of the dispersion relation of SPs, however, optical methods can additionally give interesting details.

We regard the SPs on a metallic substrate $(\varepsilon_1 = \varepsilon_1' + i\varepsilon_1'')$ covered with a thin film of thickness d_2 and characterized by the dielectric function $\varepsilon_2 = \varepsilon_2' + i\varepsilon_2''$, so that we have a two-boundary system, see Fig. 2.14. The metal substrate ε_1 is represented by a (thick) film of thickness d_1 which is assumed to be constant in the following discussion.

Where the dielectric function ε_2 of the coating film is a real quantity $(\varepsilon_2'' \approx 0)$, one observes with the ATR device for $\omega = $ const. a shift of the position θ_0 of the ATR minimum to larger θ_0 values with increasing thickness d_2 [2.28,29]. This behavior is demonstrated in Fig. 2.15 with the system LiF/Ag. Here a LiF film of different thickness is vaporized on a silver substrate. The depth of the ATR minimum remains unchanged, whereas the half width $\theta_0^{1/2}$

19
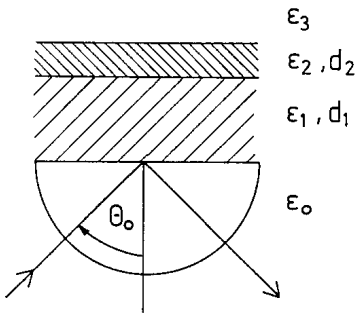
Fig. 2.14. Layered system for the observation of SPs with the reflection method. ε_0 quartz, ε_1 metal film of thickness d_1, ε_2 coating film of thickness d_2, ε_3 dielectric, air or vacuum etc
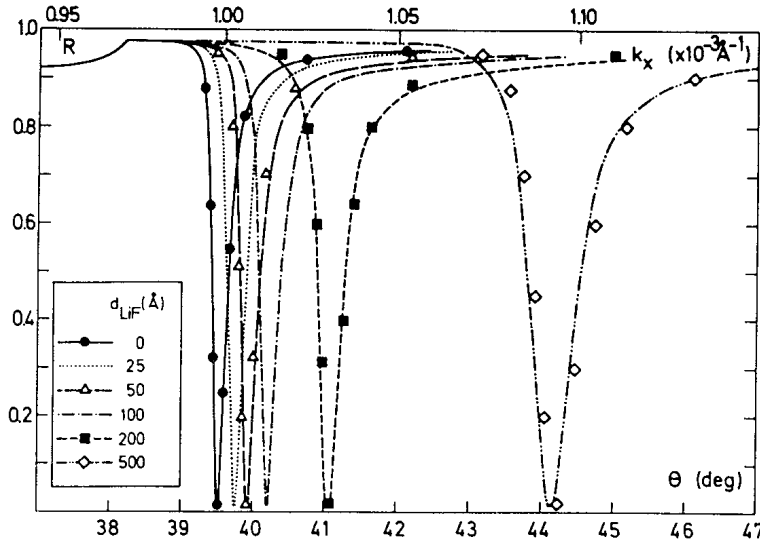
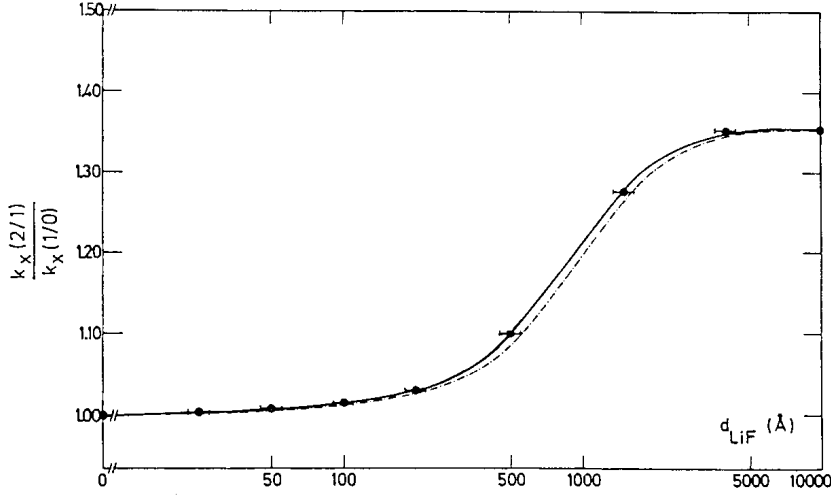**Fig. 2.15.** Observed displacement of the ATR minimum of silver with increasing thickness of a LiF coating, $\varepsilon_2'' = 0$, $\lambda = 6471\,\text{Å}$; ε_1 (Ag) $= -18.4 + i0.55$; d_1 (Ag) $= 496\,\text{Å}$, $\varepsilon_0 = 2.61$. Points are calculated values. From [2.29]

increases at thicker LiF films. The latter statement is surprising since the damping term in this film has been neglected ($\varepsilon_2'' = 0$). A detailed discussion shows that with increasing thickness d_2 of the LiF film the power flow in the different layers changes: it increases in the absorbing metal film if $\varepsilon_2' > \varepsilon_3$, see Fig. 2.15 (the reverse holds for $\varepsilon_2' < \varepsilon_3$), so that internal damping becomes stronger. At the same time the field of the SPs in the $\varepsilon_1/\varepsilon_2$ interface increases with d_2 – and thus radiation damping of the SPs – in such a way that the matching condition: internal damping equals radiation damping remains fulfilled, independent on d_2. Therefore the depth of the ATR minimum does not change. Numerical calculations have proved these considerations [2.29].

The dependence of k_x on d_2 (LiF) at constant ω or the thickness dispersion, is displayed in Fig. 2.16 for a dielectric film (LiF) of negligible ε_2'' : it changes from

$$k_x = \frac{\omega}{c}\left(\frac{\varepsilon_1'}{\varepsilon_1' + 1}\right)^{1/2} \quad \text{to} \quad k_x = \frac{\omega}{c}\left(\frac{\varepsilon_1'\varepsilon_2'}{\varepsilon_1' + \varepsilon_2'}\right)^{1/2} \ ,$$

Fig. 2.16. Observed dependence of the wave vector k_x of the resonance minimum as function of d_2 (LiF) at $\omega = $ const. (—•—): calculated with ε_2 (LiF)= 1.75; (——): calculated assuming a special layered structure of the LiF film. The ordinate displays the quotient of $k_x(2/1)/k_x(1/0)$. Above a value of d about 5000 Å the field configuration is that of an infinite thick film. From [2.29]

here $\varepsilon_3 = 1$. If the condition $d_2 > \lambda$ is fulfilled, one expects that the medium ε_2 can be regarded as infinitely thick. This is the case for $d_2 \approx 5000$ Å in Fig. 2.16.

For a small thickness of the coating d_2, the displacement against the position for $d_2 = 0$ can be written for $k'_{z2}d_2 \ll 1$ [2.11]

$$\Delta k_x(d_2) = \frac{\omega}{c} \frac{\varepsilon_2 - 1}{\varepsilon_2} \left(\frac{|\varepsilon'_1|}{|\varepsilon'_1| - 1} \right)^2 \frac{|\varepsilon'_1| + \varepsilon_2}{|\varepsilon'_1| + 1} \frac{1}{\sqrt{|\varepsilon'_1|}} \frac{2\pi d_2}{\lambda} \ .$$

This linear behavior is displayed in Fig. 2.16 up to $\sim d_2 = 50$ Å. For larger thicknesses the less simple relations have to be used [2.29].

If the coating film has a finite value of ε''_2, the behavior is different in so far as the depth of the ATR minimum changes drastically with increasing d_2 as demonstrated in Fig. 2.17 for a silver surface coated with thin films of carbon. In this case the internal absorption increases with the thickness d_2 of the absorbing material.

The behavior of dielectric coatings on gratings shall be discussed here, since the results are almost identical as long as the modulation of the grating is not too strong. Coating of the silver grating with LiF leads to figures that are very similar to those ones mentioned before [2.28a]. Experiments on gratings of Aluminum covered with Al_2O_3 or with MgF_2 demonstrated a similar displacement of k_x towards larger values [2.28b].

Planar Guided Waves. Coating with Eigen Modes

Increasing the thickness d_2 beyond the values of d_2 displayed in Fig. 2.16 we observe a series of ATR minima with the device of Fig. 2.14, or maxima, if we
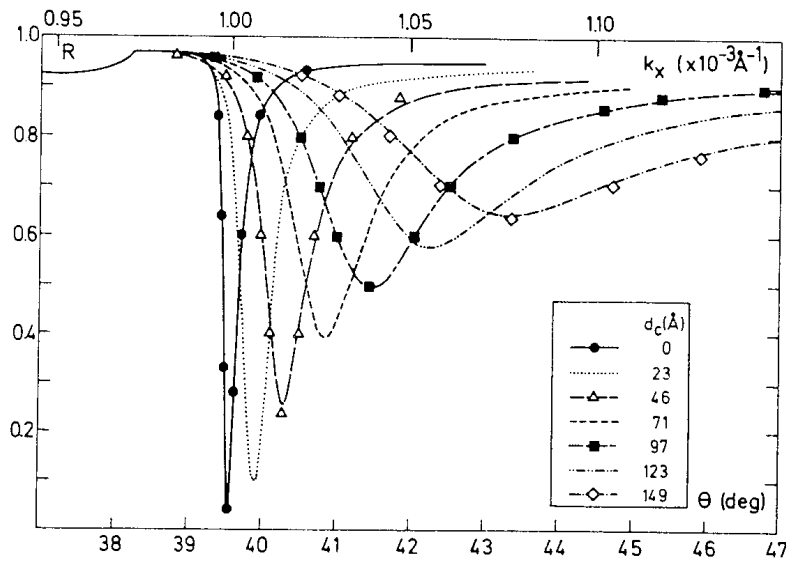
**Fig. 2.17.** Observed changes of the ATR minima of silver covered with carbon films of different thickness d_2. d_1 (Ag) $= 490$ Å, ε_2 (carbon) $= 6.0 + i3.3$; the other data are the same as in Fig. 2.15. From [2.29]

observe the light due to the coupling of SPs with the roughness of the surface (scattering device), see Fig. 2.18 [2.31]. These resonances belong to the p- and s-polarized planar guided waves in LiF. The thickness d_2 has to be at least $> \lambda/(2\sqrt{\varepsilon_2'})$ to excite the lowest mode of the spectrum. In Fig. 2.19 the relation between d_2 and k_x at constant frequency is displayed. The mode $m_p = 0$ is identical with the surface plasmon. If we scan, at constant d_2 and constant ω, over the angle θ_0 or k_x we obtain Fig. 2.18. We recognize also the thickness dispersion of SP in Fig. 2.16.
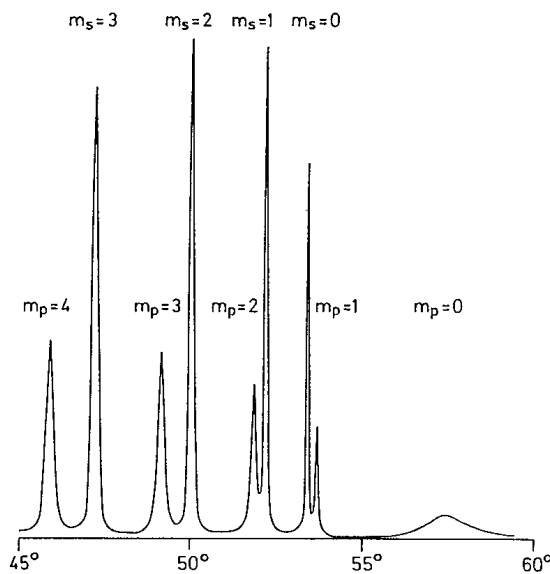
Fig. 2.18. Modes of planar guided waves, excited in a $20\,\mu$m LiF film deposited on a silver film of 500 Å thickness in an ATR device with $\lambda = 5500$ Å. They were detected by the light emitted via roughness (scattering device). The mode $m_p = 0$ is identical with the SP which is damped stronger than the other guided modes which do not have their field maxima in the metal surface. The LiF film, prepared by vaporization, has a slightly anisotropic index of refraction, therefore the sequence of s and p modes changes and is different from that given in Fig. 2.19. From [2.31]
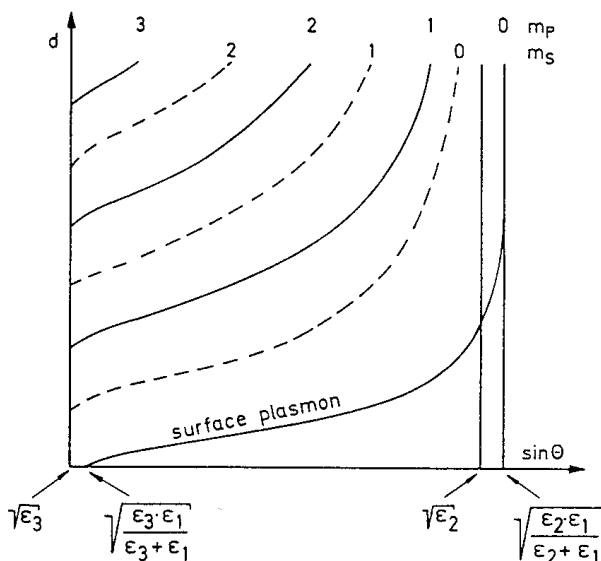
Fig. 2.19. Thickness dispersion: the relation between the thickness (d_2) of the wave-guiding film (ε_2) and the angle of incidence (sin θ) in an asymmetric layer system: $\varepsilon_1/\varepsilon_2/\varepsilon_3$, ε_1 metal film, $\varepsilon_3 \neq \varepsilon_1$, for a given frequency ω. Between the light lines $c/\sqrt{\varepsilon_3}$ and $c/\sqrt{\varepsilon_2}$ in a $\omega(k_x)$ diagram or in the present d vs. sin θ diagram at $k_x/(\omega/c) = \sqrt{\varepsilon_3}$ and $\sqrt{\varepsilon_2}$ the light modes exist, except the $m_p = 0$ or the SP mode which starts at $[\varepsilon_1\varepsilon_3/(\varepsilon_1 + \varepsilon_3)]^{1/2}$ for $d_2 = 0$ and converges to $[\varepsilon_1\varepsilon_2/(\varepsilon_1 + \varepsilon_2)]^{1/2}$, for $d_2 \to \infty$. From [2.3a]

Excitons in a Dye

Another interesting example relates to the excitonic excitation of a dye. A silver film can be coated with monolayers of cadmium arachidate (C 20) using the Langmuir-Blodgett method; each layer has a thickness of 27 Å and displaces the ATR minimum by $\Delta\theta_0$ which amounts for small $\Delta\theta_0$ at $\lambda = 6000$ Å to about 1/2 degree as Fig. 2.20 [2.32] shows. On this C 20 layer a monolayer of dye molecules has been deposited forming a "Scheibe" or "j-aggregate". This dye layer can have a relatively sharp absorption band in the visible range, e.g., $\lambda_0 = 5750$ Å for the dye "S 120", see [2.33]. Measuring the dispersion relation of the system: silver ($d_1 = 500$ Å)/a layer C 20/a dye monolayer, the curves displayed in Fig. 2.21 are obtained. On the left the dispersion relation of the bare silver surface is illustrated and on the right that of the layer system. The figure demonstrates the interaction of the SP with the excitonic excitation in the coating film by the deformation of the dispersion relation. The same phenomenon has also been observed with other dyes on C 20 layers [2.34, 34a].

A similar situation occurs if a silver surface is covered with a LiF film on which small isolated silver clusters are deposited [2.35]. The LiF film serves as a spacer. The clusters have an eigen frequency ("localized plasmon") of ≈ 4000 Å in this case; a displacement of the ATR minimum has been observed, see also [2.36], but not a kink since the dispersion of this system has been measured below the eigen frequency at 5145 Å, so that no bending back of the ATR minimum is observed as in Fig. 2.21.

If a metallic coating is used instead of a dielectric, e.g., Mg/Al, the existence of a SP with frequency ω_s is possible in the interface. In the simple case
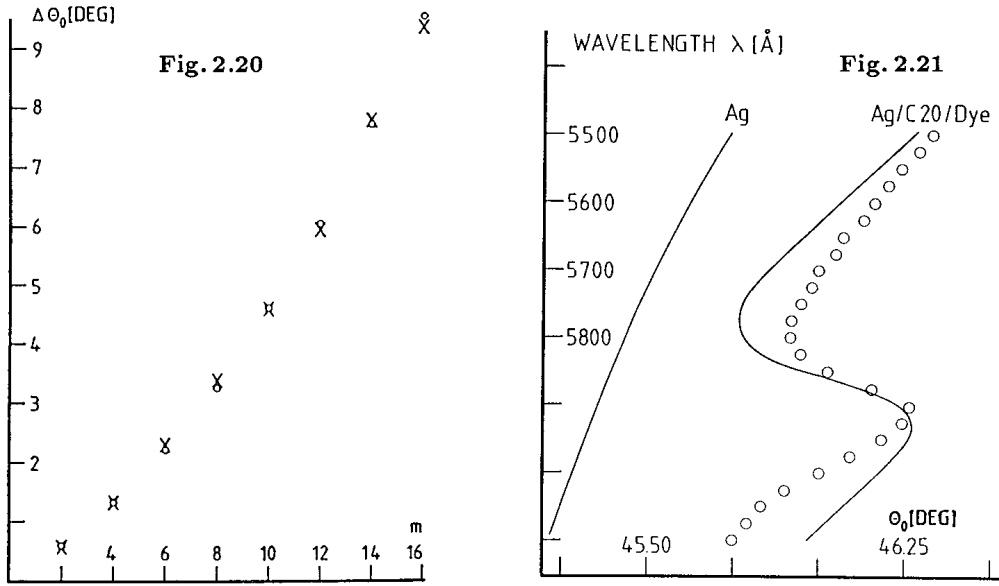
Fig. 2.20. (X) Observed shift on the resonance minima, $\Delta\theta_0$, with increasing number m of cadmium arachidate monolayers; (o) calculated values. [ε(C20) = 2.28]. From [2.32]

Fig. 2.21. The position of theATR minima as a function of θ_0 and of λ of the layer system (silver/C20/dye). *Left:* bare silver surface. The kink in the right curve demonstrates the interaction of the SP with the dye. (o) measured data; (———): calculated data. From [2.33]

of a free-electron gas as in Al and Mg with the plasma frequencies ω_{p1} and ω_{p2} the condition $\varepsilon_1 = -\varepsilon_2$, see (2.7), yields with

$$\varepsilon_i = 1 - \frac{\omega_{pi}^2}{\omega^2} \tag{2.32}$$

for the frequency ω_s

$$\omega_s^2 = \tfrac{1}{2}(\omega_{p1}^2 + \omega_{p2}^2) \tag{2.33}$$

valid in the nonretarded region. This result has been verified in experiments with electron-loss spectroscopy [2.37]. The behavior in the retarded region has been discussed in [2.38a]. A detailed study of the gold-silver system, i.e., a metal covered with another metal, has been reported in [2.38b,c].

2.7 Surface Plasmons on Thin Films; Thickness Dependence of the Damping

Up to now we have treated the physics of SPs which propagate on smooth surfaces of semi-infinite metals. Surface plasmons exist on thin films, too. Their properties depend on the film thickness and the dielectric medium on both sides of the film.

As we have seen, the metal film between asymmetric dielectrica, e.g., quartz/metal film/air allows the excitation of SPs by irradiation with light, see Fig. 2.6. The symmetric environment on both sides of the metal film, see Fig. 2.22, also has interesting properties, especially if the thickness of the metal film becomes small, more exactly $k_{z1}d\ll1$. The symmetry causes the SP frequency to be the same on both sides of the film, so that in the case of a thin film the electromagnetic fields of both surfaces interact and the frequency splits into $\omega^\pm$, a high-frequency mode ω^+ (electric field asymmetric to the plane $z = 0$) and a low-frequency mode ω^- (electric field symmetric to the plane $z = 0$) [2.1]. For further details see [2.3b]. The values of ω^+ and ω^- depend therefore on k_x as well as on d, the thickness of the metal film, as Fig. 2.23 displays.

The dispersion relation for the symmetric environment is the following [2.3b]:

$$\omega^+ \ : \ L^+ = \varepsilon_1 k_{z2} + \varepsilon_2 k_{z1}\tanh\frac{1}{2i}k_{z1}d = 0 \tag{2.34}$$

$$\omega^- \ : \ L^- = \varepsilon_1 k_{z2} + \varepsilon_2 k_{z1}\mathrm{ctgh}\frac{1}{2i}k_{z1}d = 0 \ . \tag{2.35}$$
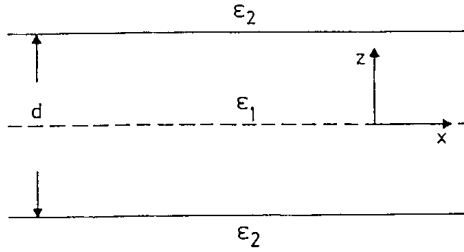
Fig. 2.22. A symmetric layer system $\varepsilon_2/\varepsilon_1/\varepsilon_2$. ε_1 : dielectric function of the metal film. $z = 0$ is the plane of symmetry
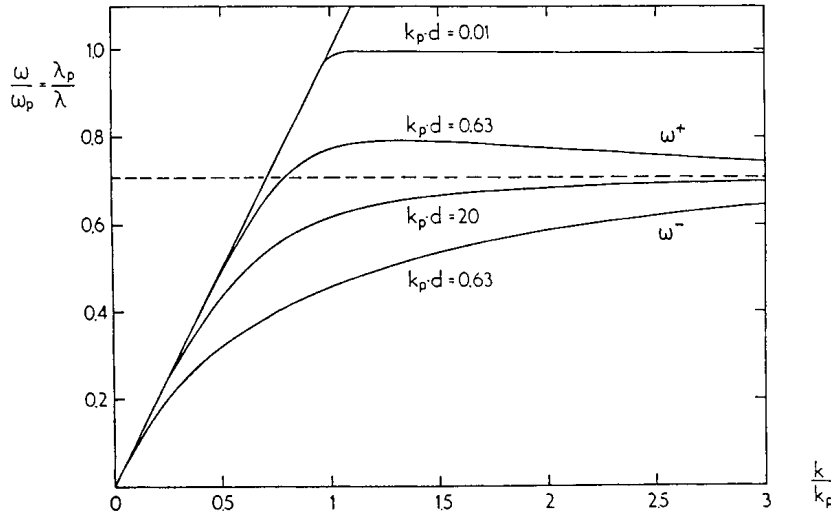
Fig. 2.23. Dispersion relations of nonradiative surface plasmons of films of different thickness d (at constant k_p). $k_p d = 0.63$ means, e.g., at a plasma wavelength of $\lambda_p = 6000$ Å: $d = 630$ Å; $k_p = 2\pi/\lambda_p$. $k_p d = 20$ represents a very thick film, so that the SPs of both sides are almost decoupled and the curve is identical with the dispersion relation of a single boundary metal/dielectric. The metal is assumed as free electron gas. From [2.3b]

This is valid for p-polarized light; s modes do not exist. For large k_x ($k_{z1} = k_{z2} = ik_x$) (2.34) becomes

$$\frac{\varepsilon_2 + \varepsilon_1}{\varepsilon_2 - \varepsilon_1} = \mp e^{-k_x d} \tag{2.36}$$

which yields for a free-electron gas [2.1] and $\varepsilon_2 = 1$:

$$\omega^{\pm} = \frac{\omega_p}{\sqrt{2}}(1 \pm e^{-k_x d})^{1/2} \ . \tag{2.37}$$

If the metal foil is covered with a dielectric material ε_2 we obtain

$$\omega^{\pm} = \frac{\omega_p}{(1 + \varepsilon_2)^{1/2}} \frac{1 \pm \exp(-k_x d)}{1 \mp \gamma \exp(-k_x d)} \ ,$$

$$\gamma = \frac{\varepsilon_2 - 1}{\varepsilon_2 + 1} \ . \tag{2.38}$$

These equations demonstrate the splitting in the nonretarded region and in addition the relation $\omega^+ > \omega^-$ for finite d. For $k_x d > 1$ we obtain (2.8) which we have discussed earlier.

This theoretical prediction has been confirmed by electron-loss spectroscopy with freely supported Al foils of $\approx 200\,\text{Å}$ thickness [2.39,40]. Figure 2.24 shows besides the 15 eV loss, the excitation of the volume plasmon $\hbar\omega_p$, the SPs split into 4.9 and 9.4 eV. This is the surface excitation of a Al film. (It is covered with a very thin oxyd film which reduces the 10 eV excitation of a clean Al surface to about 7 eV) [2.41].

The dispersion relation displayed in Fig. 2.25 has been studied from large k_x values down to k_x values of $\approx 10^{-2}\,\text{Å}^{-1}$. In the case of fast electrons k_x is given by $k_{el} = 2\pi/\lambda_{el}$, $\lambda_{el} = 0.05\,\text{Å}$ at 50 KeV, and the scattering angle θ
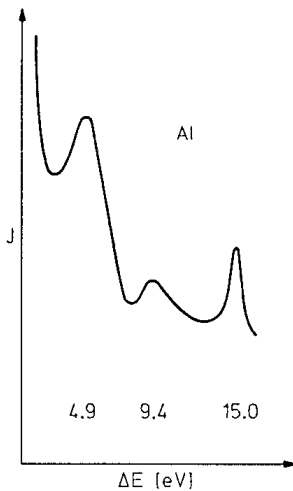
Fig. 2.24. Electron-loss spectrum in transmission of a thin (200 Å) Al film (oxydized): the 4.9 eV and 9.4 eV loss display the split 7 eV SP and the 15 eV shows the volume plasmon loss. Observed at $\theta = 0$ with an angular aperture of 1.6×10^{-4} rad. From [2.3b]

26

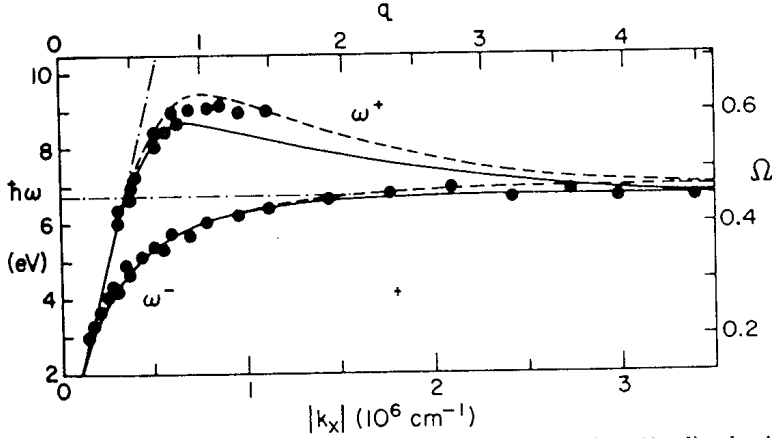**Fig. 2.25.** Dispersion relation $\omega(k_x)$ of a thin Al foil (oxydized), obtained with electron-loss spectroscopy at the 6.7 eV loss. The spectrometer has an angular resolution of approximately $\Delta k_x = 10^{-4}$ Å^{-1}. From [2.42]

(see Fig. 2.3): $k_x = k_{el}\theta$. If θ amounts to about 10^{-4} rad, k_x is given as about 10^{-2} Å^{-1}. Applying special electron optics, the aperture of the electron beam has been reduced by an order of magnitude, so that the dispersion relation could be observed down to $k_x \approx 10^{-3}$ Å^{-1}, which is comparable with that reached with optical means, see Fig. 2.25 [2.42].

It is obvious that this splitting has also been studied with optical means, since the observations in the region of the light line are less difficult than those with electron-loss spectroscopy and give more details in the low k_x region. Such experiments have been reported by *Kovacs* and *Scott* [2.43a] who observed the splitting in a MgF$_2$/Ag/MgF$_2$ device and they noticed that the damping of the ω^+ mode slightly decreased with smaller thickness d of the metal film [2.43b]. *Fukui* and *Normandin* [2.44] found in a study of the symmetric system, that the damping of the high-frequency mode ω^+ decreases with decreasing thickness d and the reverse of the ω^- mode. This result has been confirmed by *Sarid* [2.45]. The physical reason is the decrease of the field in the film which is pushed out of it with decreasing d, so that the Joule heat per cm^3 diminishes.

Numerical values of the damping as a function of the film thickness d are obtained by evaluating (2.34). For a quick calculation (2.34) can be simplified for small d by putting tgh $x \approx x$ with $x = (1/2i)k_{z1}d$ which implies $(1/3)x^2 < 1$. With $\lambda = 6325$ Å, $|\varepsilon_1'| = 18$, and $k_x = 1.5 \times 10^{-3}$ Å^{-1}, this is valid for $d \lesssim 800$ Å. For real ω the imaginary part k_x comes out as

$$k_x'' / \left(\frac{\omega}{c}\right) = \sqrt{\varepsilon_2^5} \frac{|\varepsilon_1'| + \varepsilon_2}{2|\varepsilon_1'|} \frac{\varepsilon_1''}{2|\varepsilon_1'|^2} \left(\frac{\omega}{c}d\right)^2 \tag{2.39}$$

which shows that k_x'' decreases below $d = 800$ Å with d^2.

In Fig. 2.26 [2.46] the lower full line shows the computer-calculated decrease of Im$\{\beta\} = k_x''/(\omega/c)$ with decreasing film thickness d. Crosses display measured values; both values observed and calculated agree within a factor
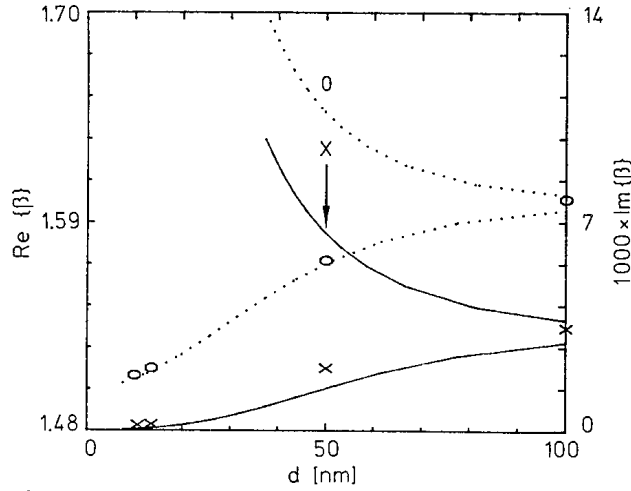
Fig. 2.26. The real part $k'_x/(\omega/c)$ ($= \mathrm{Re}\{\beta\}$) and the imaginary part $k''_x/(\omega/c)$ ($= \mathrm{Im}\{\beta\}$) as function of the thickness d. From [2.45]

2. Values calculated with (2.39), display good agreement with the computer-calculated data, see Table 2.1.

Table 2.1. Damping of the ω^+ mode as function of film thickness d

d [Å]	k''_x [Å^{-1}]	
	Computer calculated data	Equation (2.39)
500	1.4×10^{-3}	1.45×10^{-3}
400	0.9	0.93
300	0.5	0.52
200	0.2	0.23

Figure 2.26 demonstrates some further results: the k''_x of the ω^- mode, low-frequency mode, upper full line, increases with decreasing thickness due to the fact that the electromagnetic energy density increases with decreasing d.

Another feature is shown: the real parts of k_x (lower dotted line for ω^+ and upper dotted line for ω^-) change with the film thickness d in an opposite manner; this however is easily understood from Fig. 2.27.

Another experiment by *Quail* et al [2.47] demonstrates how the half widths of the ATR minima decrease if the silver film thickness is reduced from 505 Å to 170 Å: it decreases from 0.5° to about 0.05°, see Fig. 2.28. The calculated data (full line) indicate a smaller width perhaps because diffraction effects are neglected [2.47]. The device used in this experiment is shown in Fig. 2.29.

Since the propagation length L_i is proportional to $(2k''_x)^{-1}$, see (2.12), L_i increases by about a factor of 10 compared to L_i ($d = \infty$) in the above cases. A corresponding increase of the enhancement of the field intensity is expected in these thin films.
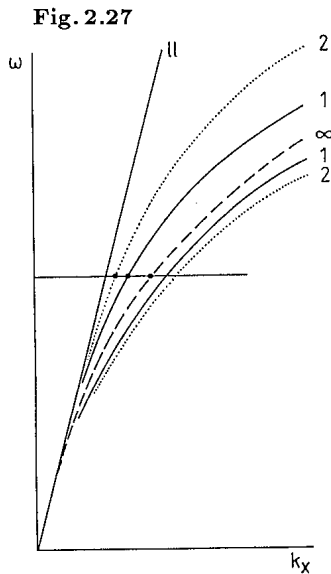
Fig. 2.28 ►
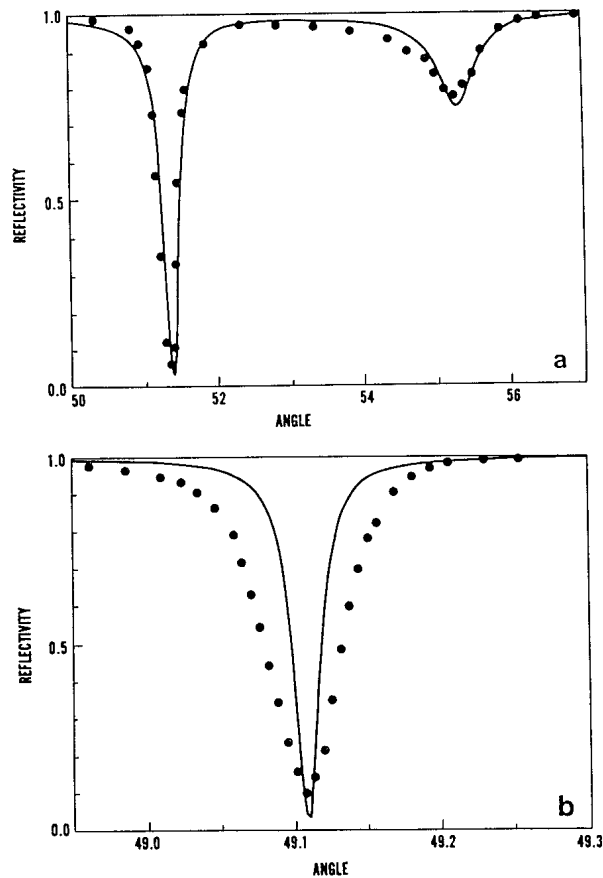
Fig. 2.27

Fig. 2.27. Schematic representation of the dispersion relation for ω^+ and ω^- near the light line (ll). The numbers beside the curves indicate the thickness of the metal film: $d = \infty$ (---) is identical with $k_{\mathrm{p}}d = 20$ of Fig. 2.23. (1) is valid for a thin film and (2) for a still thinner film: At a given frequency the resonance angle displaces to smaller values of k_x if the film becomes thinner as shown in Fig. 2.26. $d{\to}0$ leads to $\omega{\to}c/\sqrt{\varepsilon_2}\,k_x$ (light line)

Fig. 2.28a,b. ATR minima from a thin silver film in a symmetric environment as a function of the interior angle of incidence $\lambda = 10\,600\,\text{Å}$. **(a)** displays the splitting of the silver SPs into the ω^+ (left minimum) and ω^- mode. $d\,(\text{Ag}) = 505\,\text{Å}$. **(b)** If the film thickness of Ag is reduced to $170\,\text{Å}$, the resonance angle displaces to a smaller angle and the half width decreases essentially. This displacement can be understood with the help of Fig. 2.27. The coupling distances $d(b)$ amount to $5000\,\text{Å}$ in **(a)** and to $12\,000\,\text{Å}$ in **(b)**. From [2.47]

Fig. 2.29. ATR device for exciting the symmetric SP mode ω^+ of a very thin metal film (c). The layers (b) (oil $n = 1.4564$) and (d) (glass $n = 1.4569$) represent the symmetric environment of the metal film (c) so that a splitting of the SP mode occurs. The optimal thickness of the layer (b) can be realized by changing the mechanical pressure between the prism (a) and the glass (d). From [2.47]

2.8 Second Harmonic Generation (SHG)

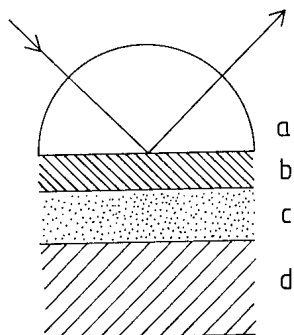An interesting way of demonstrating the field enhancement at the SP resonance in an ATR device has been displayed by the generation of SH [2.48]: A strong electric field of frequency ω produces in a nonlinear medium a polarization $P(2\omega) = \chi^{(2)}E^2$, with $\chi^{(2)}$ the quadratic susceptibility. This polarization causes a light emission of frequency 2ω, e.g., light reflected at a smooth silver surface gives a signal of 2ω light which is easy to detect. The scheme of the device is shown in Fig. 2.30: Two SPs of frequency ω interact in the high field region in the silver/air surface, so that because of the conservation of momenta and energy, we have

$$2\hbar\frac{\omega}{c}[\varepsilon_0(\omega)]^{1/2}\sin\theta_1 = \hbar\frac{2\omega}{c}[\varepsilon_0(2\omega)]^{1/2}\sin\theta_2 \ . \tag{2.40}$$
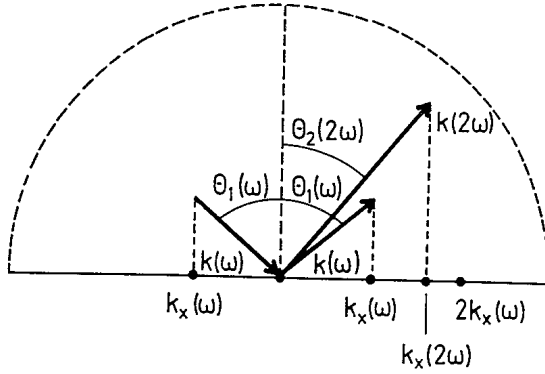
Fig. 2.30. The generation of a second harmonic in the ATR device and its detection by reflection

The angle of emission of the 2ω beam becomes

$$\sin\theta_2 = [\varepsilon(\omega)/\varepsilon_0(2\omega)]^{1/2}\sin\theta_1 < \sin\theta_1 \tag{2.41}$$

with ε_0 the dielectric function of e.g., glass or quartz. If $\theta_1(\omega)$ reaches the resonance value or the enhanced field its maximum, the 2ω intensity, emitted at θ_2, goes to a maximum. The SH beam is reflected at an angle θ_2, 1.5° smaller than θ_1 ($\lambda = 7000\,\text{Å}$, crown glass) as a result of the dispersion of the glass (Fig. 2.31).

If the surface metal/air is rough, the SH can also be observed by roughness scattering.

These experiments were recently reexamined under improved experimental conditions at $\lambda = 1.06\,\mu$. The structure of the SHG background reflectivity as a function of the angle of incidence and the observed strong increase of the SHG peak by about a factor of 100, if the fundamental SP frequency is excited, have been found to be within 20% in agreement with theoretical considerations [2.49].

The generation of SH has been also applied to demonstrate the strong enhancement in thin films, as discussed in Sect. 2.7.

30
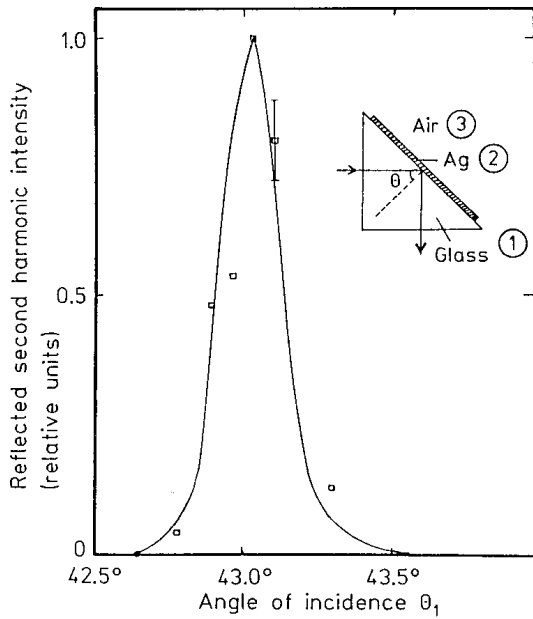
Fig. 2.31. Reflected second-harmonic intensity at a silver film of 560 Å thickness, deposited on a glass prism as a function of the angle of incidence, see inset. The smooth curve is calculated. The 2ω radiation is produced by the nonlinear susceptibility of the silver surface. From [2.48]

For this purpose the ATR device, Fig. 2.29, is used. The medium (d) in Fig. 2.29 is replaced by a nonlinear material, e.g., a quartz crystal of special orientation, so that the dielectrica on both sides are symmetric concerning the refractive index. The metal film has a thickness d of 135 Å. If the fundamental SP is excited, a strong intensity of 2ω is emitted from the interface metal/quartz, Fig. 2.32 [2.50]. The 2ω intensity of the large peak, the LRSP mode (long range surface plasmon) is more than 10^3 times stronger than that of a single boundary SP displayed by the dashed curve.

In the cases just mentioned the resonant excitation of SPs has been produced in the ATR device. Since SPs can also be excited via corrugation of the surface e.g., at rough as well as at sinusoidal profiles, and a strong field enhancement is produced, we expect the SH generation also under these conditions, see Chaps. 3, 5.

Application of the Nonlinear Third-Order Susceptibility

The third-order nonlinear susceptibility $\chi^{(3)}$ $(\omega_1, \omega_2, \omega_3)$ has also been applied in SP physics: If one regards those nonlinear processes which reproduce the incoming frequency ω or $P^{(3)} = \chi^{(3)} E^3$, the dielectric function can be written as

$$\varepsilon_0(E) = \varepsilon_0(E \approx 0) + \chi^{(3)}(\omega)E^2 \ , \qquad (2.42)$$

where E^2 is given by the incoming light intensity. This means that the dielectric behavior of this material depends on the intensity of the electromagnetic field acting in it. If such dielectrica as Si or GaAs are adjacent to the silver surface on which the SPs propagate, the dispersion relation is changed. Assuming

$$\varepsilon_0(E) < \varepsilon_1' \quad \text{and} \quad \chi^{(3)}(\omega)E^2 < \varepsilon_0(E \approx 0) \qquad \text{one obtains}$$
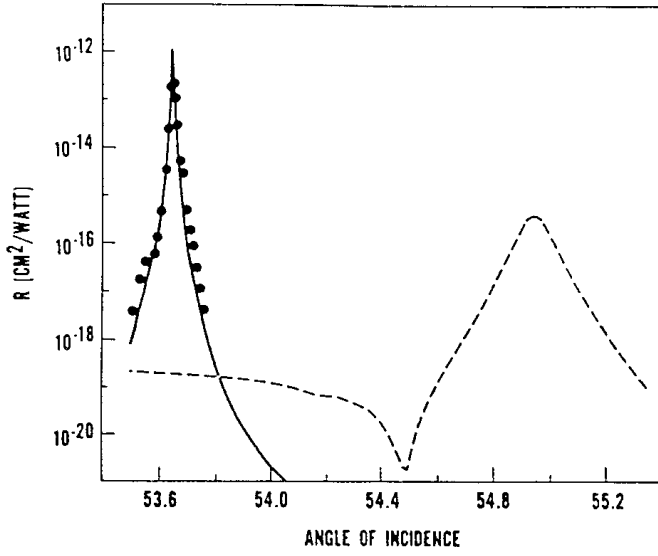
Fig. 2.32. Reflected second-harmonic intensity from the ATR device Fig. 2.29 as a function of the angle of incidence in the prism. The thin metal film (c) of 135 Å lies between an oil film (b) and a quartz crystal (d). By mechanical pressure between (a) and (d) which changes the thickness of the oil film (b), the optimal coupling of the fundamental SP ($\lambda = 1.06\,\mu$) into the system can be reached; it is $d(b) = 30\,000$ Å. The high field at the metal/quartz interface and the nonlinearity of the quartz produce the 2ω radiation peak (full circles). For comparison the dashed line displays the SH intensity at a single boundary. From [2.50]

$$k_x(E) = \frac{\omega}{c}\left(\frac{\varepsilon_1' \varepsilon_0(E)}{\varepsilon_1' + \varepsilon_0(E)}\right)^{1/2}$$

$$= k_x(E \approx 0)\left\{1 + \chi^{(3)}(\omega)\frac{2\pi E^2}{\varepsilon_0(E \approx 0)}\right\} \tag{2.43}$$

and as consequence the resonance is displaced; the sign of it and its value allow measurement of the quantity $\chi^{(3)}(\omega)$ [2.51].

The SP field E consists essentially of the inhomogeneous field $E(z)$, the transverse component, which extends into the nonlinear medium. This $E(z)$ field can be substituted by the field at the metal surface which is given by the incoming light intensity [2.51].

In the experiments grating couplers were used. The gratings were brought up on single crystals of Si and GaAs and covered with a thick silver film. p-polarized light ($\lambda \approx 1\,\mu$) was incident on the air/semiconductor interface. Scanning the angle of incidence reflection minima were observed when the (-1) diffraction order was resonantly excited. Figure 2.33 displays the result on a Si/Ag surface at low laser intensities, $10\,\mu$ Joule/pulse, whereas higher intensities, $70\,\mu$ Joule/pulse, displace the minimum to larger angles; the reverse happens at GaAs/Ag interfaces. At Si the $\chi^{(3)}(\omega)$ is negative, as Fig. 2.33 demonstrates and the value of the displacement yields a change of the refractive index of 4×10^{-5} per MW/cm^2 of laser intensity at the interface under the given experimental conditions [2.51].
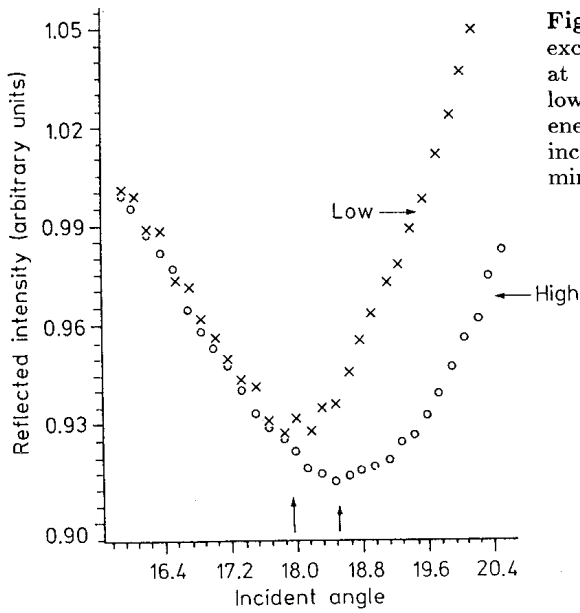
Fig. 2.33. The intensity around the SP excitation reflected at a Si/Ag grating at high (o) (70 μ Joule/pulse) and at low (X) (10 μ Joule/pulse) input laser energy as a function of the angle of incidence. The arrows indicate the ATR minima. From [2.52]

2.9 Influence of Corrugation

General Relations

Discussing the grating coupler together with Fig. 2.4 we have seen that the surface wave vector k_x of SP or of photons can combine linearly with the vectors Δk_x which compose the Fourier spectrum of the perturbation of the surface. In the simplest case of a sinusoidal grating these values of Δk_x are $\pm 2\pi/a$, a being the grating constant, whereas in the case of a statistical rough surface a continuum of Δk_x values is disposable. Since in this case the roughness profile cannot be described by an analytical function, a correlation function is introduced: The roughness profile may be given by $z = S(x, y)$, see Fig. 2.34, which is measured against the plane $z = 0$, defined by

$$z = \frac{1}{F} \int s(x, y) dx\, dy = S = 0 \ . \tag{2.44}$$
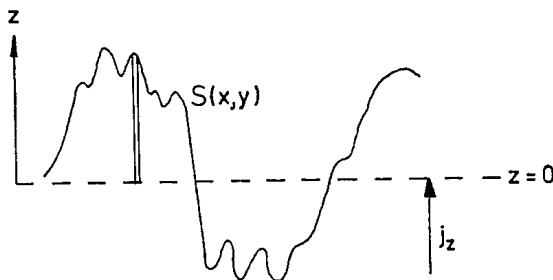
Fig. 2.34. Scheme of a rough surface. The integral $(1/L) \int_0^L S(x)dx = S = 0$ defines the level $z = 0$. The corrugation is drawn much stronger than that considered in this book. For example, the first-order approximation requirs $\delta/\sigma{\sim}1$ % or the deviations of $S(x, y)$ from the line $z = 0$ have to be reduced by a factor of about 100

It follows that the expression for the correlation function is given by

$$G(x,y) = \frac{1}{F} \int_F S(x',y')S(x'-x,y'-y)dx'dy' \tag{2.45}$$

which measures the correlation of $S(x',y')$ and $S(x'-x,y'-y)$ in a distance x,y.

From (2.45) it follows that

$$G(0,0) = \overline{S^2} \,, \tag{2.46}$$

where $(\overline{S^2})^{1/2}$ is called the root mean square height δ. It characterizes the roughness.

A further important relation is the Fourier transform of the correlation function. It appears as a result, e.g., in light scattering theory, see (3.1), and can be measured. From (2.45) it follows for the transform that:

$$\left(\frac{1}{2\pi}\right) \int_F dx\,dy\,G(x,y)\exp[-i(\Delta k_x x + \Delta k_x y)] = |s(\Delta k)|^2 \,. \tag{2.47}$$

The term $|s(\Delta k)|^2$ is often called "spectral density function" since it gives the spectrum of Δk values which may be transferred from the rough surface to SPs or photons.

In some papers the Fourier transform is defined as in (2.47), but without the factor $(1/2\pi)^2$. Then instead of $|s(\Delta k)|^2$ one writes $(2\pi)^2|s(\Delta k)|^2 = \delta^2|g(\Delta k)|^2 = \delta^2\pi\sigma^2\exp[-(1/4)\sigma^2(\Delta k)^2]$.

In order to evaluate this relation an assumption for the correlation function is necessary. For simplicity a Gaussian function is often used, since it allows convenient calculations

$$G(x,y) = \delta^2\exp\left(-\frac{x^2+y^2}{\sigma^2}\right) \tag{2.48}$$

with σ being the correlation length. This shows how quickly the correlation disappears with larger distances; $\sigma \to 0$ means the S values are not correlated, a completely random distribution exists.

The Fourier transform of (2.48) comes out as

$$|s(\Delta k)|^2 = \frac{1}{4\pi}\sigma^2\delta^2\exp\left(-\frac{\sigma^2(\Delta k)^2}{4}\right) \,. \tag{2.49}$$

It shows that the plot of observed $|s(\Delta k)|^2$ values in logarithmic presentation gives a linear relation between $\ln|s|^2$ and Δk^2 which allow us to obtain the roughness parameters δ and σ from $\ln|s(0)|^2$ and the slope of this linear dependence.

The experiments showed that the Gaussian function is in some cases a satisfying approximation. In other cases, e.g., for polished surfaces, the expo-

nential correlation function describes the experiments somewhat better, see Chap. 5.

The term Δk, one Fourier component of the roughness spectrum, means the roughness vector transferred from the rough surface to the SPs or photons. For example, in the ATR device the incoming light has a component parallel to the surface $k_x = \sqrt{\varepsilon_0}\omega/c \sin\theta_0$, the scattered light $k_x = (\omega/c)\sin\theta$. With ϕ being the angle between the plane of incidence and observation, we have

$$\Delta k = \frac{\omega}{c}[(\sqrt{\varepsilon_0}\sin\theta_0)^2 - 2\sqrt{\varepsilon_0}\sin\theta\cdot\cos\phi + \sin^2\theta]^{1/2} \; , \qquad (2.50)$$

where Δk has its largest value for $\phi = 0$ and $\theta < 0$ (backward scattering):

$$\Delta k = \frac{\omega}{c}(\sqrt{\varepsilon_0}\sin\theta_0 + \sin\theta) \; . \qquad (2.51)$$

At $\theta = 0$, observation in the direction of the surface normal, the value of Δk becomes

$$\Delta k = \sqrt{\varepsilon_0}\frac{\omega}{c}\sin\theta_0 \; . \qquad (2.52)$$

Since the roughness is regarded as isotropic, we write in the following $\Delta k = \Delta k_x$.

If $|s(\Delta k)|^2$ is known from the experiments, $\overline{S^2}$ can also be derived from (2.47)

$$\overline{s^2} = 2\pi \int d\Delta k \Delta k |s(\Delta k)|^2 \; , \qquad (2.53)$$

without specifying $|s(\Delta k)|^2$.

In the case of a grating described by

$$S(x) = h\sin\frac{2\pi}{a}x \qquad (2.54)$$

the Fourier transform becomes

$$|s(\Delta k_x)|^2 = \left(\frac{h}{2}\right)^2 |\tilde{\delta}(k_x^0 + g) + \tilde{\delta}(k_x^0 - g)| \; , \qquad (2.55)$$

where $\tilde{\delta}$ means the delta function. It shows that, in this approximation, only two light emission directions $k_x \pm g$ exist, the two diffraction orders ± 1, which are produced by a sinusoidal grating.

Propagation Length of the SPs on Rough Surfaces

We have seen that the energy of the SPs dissipates on smooth surfaces by internal absorption. The term L_i measures this propagation length, see (2.11).

If the surface is rough, two additional processes have to be regarded which can influence the propagation length: the transition of the SPs via roughness into photons emitted into the air space and further the scattering of the SPs into SPs of different direction but without change of the absolute value of the wave vector. Both processes have been discussed, see Figs. 2.5, 3.9.

The relations of the mean free path length L_{rad} for radiation loss and L_{sc} for scattering in the presence of roughness have been calculated [2.52]. The scattering process at the corrugations in the surface comes out as

$$L_{\text{sc}} = \frac{2}{3} \frac{|\varepsilon_1'|}{(\omega/c)^5} \frac{1}{\sigma^2 \delta^2} \ . \tag{2.56}$$

The radiation loss is given by

$$L_{\text{rad}} = \frac{3}{4} \frac{|\varepsilon_1'|^{1/2}}{(\omega/c)^5} \frac{1}{\sigma^2 \delta^2} \ . \tag{2.57}$$

The intensity of the SP decreases to $1/e$ after having traveled these lengths.

These relations are valid for $|\varepsilon_1'| \gg 1$ i.e., in the region of the light line for $k_x \sigma \ll 1$.

Comparing both processes one sees that

$$L_{\text{rad}}/L_{\text{sc}} = \tfrac{9}{8} (\sqrt{|\varepsilon_1'|})^{-1} \ . \tag{2.58}$$

With longer wavelengths the value of L_{rad} becomes shorter, i.e., the radiation loss is more effective than the scattering. This is due to the similarity of SPs and photons near the light line.

For $|\varepsilon_1'| \to 1$, in the flat part of the dispersion relation, the reverse holds: the value of L_{sc} increases more than L_{rad}.

For experiments with the ATR device one can roughly say that due to the condition $\Gamma_i = \Gamma_{\text{rad}}$ the damping is doubled or the value of L_i is halved, so that L_i/L_{rad} becomes smaller and the roughness influence is reduced.

The application of the above relations is strongly limited by the condition $k_x \sigma \ll 1$. In the infrared $\lambda = 10\mu$ the condition is fulfilled. Most experiments however are made between $\lambda = 1\mu$ and 0.5μ. Although at $\lambda = 5000\,\text{Å}$ ($\varepsilon_1' = -10.5$) and $\sigma = 500\,\text{Å}$: $k_x \sigma = 0.6$ is not small against 1, the numerical values may be given for $\delta = 15\,\text{Å}$: $L_i = 22\mu$, $L_{\text{rad}} = 1400\mu$, and $L_{\text{sc}} = 4000\mu$. It shows − if one accepts the calculation − that the internal absorption is the most effective one.

The roughness has been chosen in this example to be $\delta = 15\,\text{Å}$. This value is near the limit of the linear approximation. In theoretical papers, a value of $\delta \sim 100\,\text{Å}$ is often used for numerical calculations without regarding this limit.

Even at $\delta = 50\,\text{Å}$ multiple scattering is so strong that one has to be careful with the assumption of excessively large δ values.

The question arises whether roughness comes into play if the damping (internal absorption) of the ω^+ mode is strong in very thin films, see Sect. 2.7. It may be that the reduction of the damping is limited by roughness, but this is difficult to say in a general form. Using the above figures, an increase of the propagation length L_i by a factor of 50–60 would bring L_i near L_{rad}, so that the total mean free path length, given by $L_{tot}^{-1} = (L_i)^{-1} + (L_{rad})^{-1}$ is reduced.

Localization of SPs

If the surface is rather rough, say with an approximate value of $\delta > 50\,\text{Å}$, the SPs are strongly scattered and move with increasing disorder and less as an extended wave. They are strongly scattered so that their propagation along the surface resembles a diffusion process to be described with a diffusion coefficient. This is similar to the case of electrons in a perturbated potential of an amorphous solid which propagate no longer like a plane wave in a crystal.

Such a situation is realized if a light beam of frequency $\omega < \omega_s$ is reflected at a rough surface and SPs are excited via roughness coupling. The diffusion, just mentioned, leads to an accumulation of electromagnetic field density which is higher than that of an extended SP wave on a smooth surface or on a surface of small roughness.

Theoretical considerations [2.53] which speculate about this enhancement phenomenon give the following numbers: At $\delta = 250\,\text{Å}$ and $\sigma = 750\,\text{Å}$ on a silver surface the enhancement increases from the value 4, which is valid for a smooth surface at small ω for a coherent superposition of the incoming and reflected light, to about 20 at larger frequencies. It increases with roughness as is expected and depends strongly on σ since with larger σ the propagation of the SP resembles more like an extended SP. Using these calculations one expects no localization on a rough surface with a δ of 5–20 Å and $\sigma = 1000\,\text{Å}$.

As is evident, it is favorable for localization that $L_{sc} < L_{rad}$ or that scattering is more probable than radiation loss. This, however, is valid only for ω near ω_s and large Δk_x. Since most experiments have been made near the light line these calculations have a limited validity. One needs experiments further away from the light line. Experimental results of this enhancement on rough surfaces are not yet available.

2.10 "Localized" Plasmons and Enhancement

Surface plasmons also exist on curved surfaces, e.g., on spheres or cylinders. We had seen that on a plane surface in the nonretarded case the eigen modes are given by the equation $\varepsilon_1 = -\varepsilon_0$ (ε_1 metal, ε_0 dielectric).

In case of a sphere the corresponding condition for SPs is given by [2.54]

$$\varepsilon_1(\omega) = -\varepsilon_0 \frac{l+1}{l} \quad l = 1, 2, 3 \ldots . \tag{2.59}$$

This yields an infinite number of modes. The lowest mode $l = 1$ can be calculated from

$$\varepsilon_1(\omega) = -2\varepsilon_0 \ . \tag{2.60}$$

These modes are radiative — the curved surface couples the modes with photons — so that they are damped in addition to the internal damping by light emission [2.55].

This relation can also be obtained from calculating the polarization of a sphere (radius a) in a uniform exterior field E_0

$$P(\omega) = \frac{3}{4\pi} \frac{\varepsilon_1(\omega) - \varepsilon_0}{\varepsilon_1(\omega) + 2\varepsilon_0} E_0 \ . \tag{2.61}$$

Equation (2.61) is valid as long as $a \ll \lambda$, where λ is the wavelength of the exterior field. The field at the surface outside the sphere ($\varepsilon_0 = 1$) is

$$E(a) = 2 \frac{\varepsilon_1 - 1}{\varepsilon_1 + 2} E_0 + E_0 = \frac{3\varepsilon_1}{\varepsilon_1 + 2} E_0 \tag{2.62}$$

which has a maximum for $\varepsilon_1' = -2$ and gives an enhancement of

$$T_{\mathrm{el}} = \left| \frac{E(a)}{E_0} \right|^2 = \left| \frac{3\varepsilon_1'}{\varepsilon_1''} \right|^2 \ . \tag{2.63}$$

For silver the condition $\varepsilon_1' = -2$ gives $\lambda = 3500\,\text{Å}$ (3.5 eV) and $\varepsilon_1'' = 0.28$ so that $T \approx 480$ results, a value which is somewhat higher than on a plane at the same wavelength.

This resonance is well known as the collective oscillation of the conduction electrons. Since it is limited to the sphere, it is often called a "localized" plasmon, and has been observed on small spheres with light as well as with electrons (electron-loss spectroscopy). More details and earlier literature can be found in [2.56].

If the sphere is deformed into a spheroid with a major (a) and a minor (b) axis lengths, the electric field at the tip of the major axis induced by an incoming light wave with E_0 parallel to this latter axis is, for an isolated spheroid [2.57,58],

$$E_{\mathrm{tip}} = \frac{(1 - A)(\varepsilon_1 - 1)}{1 + (\varepsilon_1 - 1)A} E_0 + E_0 = \frac{\varepsilon_1}{1 + (\varepsilon - 1)A} E_0 \tag{2.64}$$

with $\varepsilon_0 = 1$; the light wavelength $\lambda \gg a, b$; and A is the depolarization factor.

The resonance condition, equivalent to (2.6) is then given by

$$1 + (\varepsilon_1' - 1)A = 0 \ . \tag{2.65}$$

38

The maximum enhancement at the tip of the spheroid comes out as

$$T_{\text{max}}^{\text{el}} = \left| \frac{E_{\text{tip}}}{E_0} \right|^2_{\text{res}} = \left(\frac{\varepsilon_1'}{\varepsilon_1'' A} \right)^2 . \qquad (2.66)$$

With decreasing b/a (more elongated ellipsoids) or decreasing A, the resonance displaces to longer wavelengths and the enhancement increases. For example, with $A = 0.1$ ($b/a \simeq 1/3$) one obtains from (2.65) $\varepsilon_1' = -9$ or $\hbar\omega_{\text{res}} = 2.5\,\text{eV}$ and $\varepsilon_1'' = 0.3$; this gives $T_{\text{max}} = 10^5$.

These values are of importance for the experiments of the second harmonic generation as well as for the surface enhanced Raman scattering, see Sect. 4.5.

Since the oscillating charges radiate, the field enhancement does not reach the calculated values and in addition the resonances are broadened. This correction is introduced into (2.64) by replacing the real A by a complex term [2.59]

$$A + i\frac{4\pi^2}{3}\frac{V}{\lambda^3} = A + iR \qquad (2.67)$$

which represents a first correction of the electrostatic solution; V is the volume of the spheroid. The local field enhancement factor E_{tip}/E_0 then becomes, with $\varepsilon_0 \neq 1$ [2.60]:

$$\frac{E_{\text{tip}}}{E_0}$$

$$= \frac{\varepsilon_1'/\varepsilon_0}{1 + [(\varepsilon_1'/\varepsilon_0) - 1)]A + i(\varepsilon_1''/\varepsilon_0)A + R\varepsilon_1''\sqrt{\varepsilon_0} + iR(1 - \varepsilon_1')\sqrt{\varepsilon_0}} , \quad (2.68)$$

$R = 0$ or no radiation damping gives (2.64). Using the resonance condition (2.65), one obtains

$$\left(\frac{E_{\text{tip}}}{E_0} \right)_{\text{max}} = \frac{\varepsilon_1'/\varepsilon_0}{i(\varepsilon_1''/\varepsilon_0)A + [\varepsilon_1'' R\sqrt{\varepsilon_0} + iR(1 - \varepsilon_1')\sqrt{\varepsilon_0}]} . \qquad (2.69)$$

The radiation damping can be neglected if $\varepsilon_1'' < \varepsilon_1'$ and

$$\varepsilon_1''/\varepsilon_0 A > R(1 - \varepsilon_1')\sqrt{\varepsilon_0} \quad \text{or} \qquad (2.70)$$

$$\frac{\varepsilon_1''}{1 - \varepsilon_1'} A(\varepsilon_0)^{3/2} > R \qquad \text{hold.}$$

An Example: For a sphere [$A = 1/3$, $V = (4\pi/3)a^3$] the diameter of the sphere $2a$ can be estimated from (2.70), e.g., for silver with $\lambda = 3.500\,\text{Å}$ and $\varepsilon = -2 + i\,0.3$) we get $2a \lesssim 600\,\text{Å}$ for the value, below which radiation damping can be neglected.

For prolate spheroids these numbers are approximately the same; more precise numbers depend on the detailed conditions, see, e.g., [2.59].

3. Surface Plasmons on Surfaces of Small Roughness

In this chapter, the influence of small roughness ($\delta \approx 5{-}10\,\text{Å}$) on SPs measured with the ATR method, is reported. The remarkable result is the resonant light emission due to the SP-photon coupling via roughness. The angular distribution of the emitted light allows determination of the roughness parameters, using the linear approximation of light scattering theory.

3.1 Resonant Light Emission Observed with the ATR Device

Looking at the surface of a thin silver film deposited on the base of a prism or of a half cylinder of glass in the arrangement of Fig. 3.1, a strong light emission is observed if the dispersion relation is fulfilled and the reflected light shows a minimum intensity, below left in Fig. 3.1 [2.8].

These experiments demonstrated, that

a) the excitation of SPs on a thin metal film in direct contact with the glass prism produces an ATR minimum;

b) the SPs propagating on a rough surface radiate light into the air space of a Lorentzian shape by SP-photon coupling; and

c) the strong light intensity in the resonance case indicates a strong electromagnetic field in the boundary air/metal (field enhancement).

In Fig. 3.2a the enhanced radiation is registered: it displays the intensity maxima at different wavelengths reflecting thus the dispersion relation. The numbers on the curves mean: $n \sin \theta_0 = \sqrt{\varepsilon_0} \sin \theta_0 = \sqrt{\varepsilon_1'/(1 + \varepsilon_1')}$ given by the intersection of the dispersion relation and the straight line in the (ω, k) diagram with the slope $(c/n) \sin \theta_0$, see Fig. 2.7. Changing $n \sin \theta_0$ by choosing another ω at $\theta_0 = $ const, the maxima of Fig. 3.2a are observed. In Fig. 3.2b the corresponding experiments are displayed at $\omega = $ const and at varying angle of incidence θ_0 [2.9].

These experiments demonstrate that the first obvious effect of roughness on the SPs is the emission of light. The nonradiative SPs become radiative. The enhancement of this radiation is quantitatively expressed by the factor $|t_{012}|^2$ in (3.1).
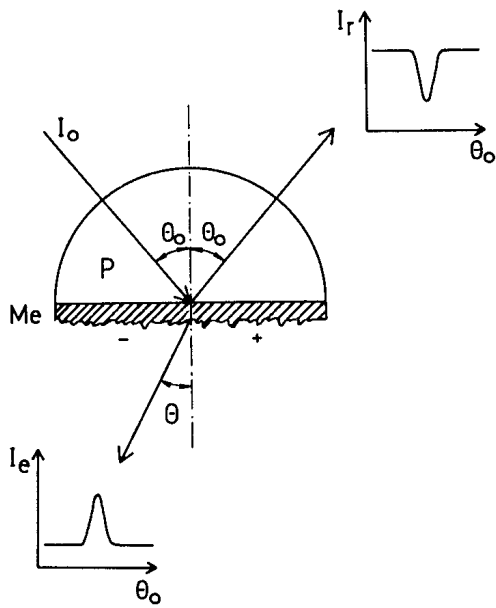
Fig. 3.1. If the SP excitation reaches its maximum at the resonance angle θ_0, the reflection intensity goes through a minimum, *top right;* at the same time the light emission due to the coupling of the SP with photons via roughness has its maximum, *bottom left*. Both methods allow detailed experiments with SPs. θ means the fixed direction of observation. From [2.4]
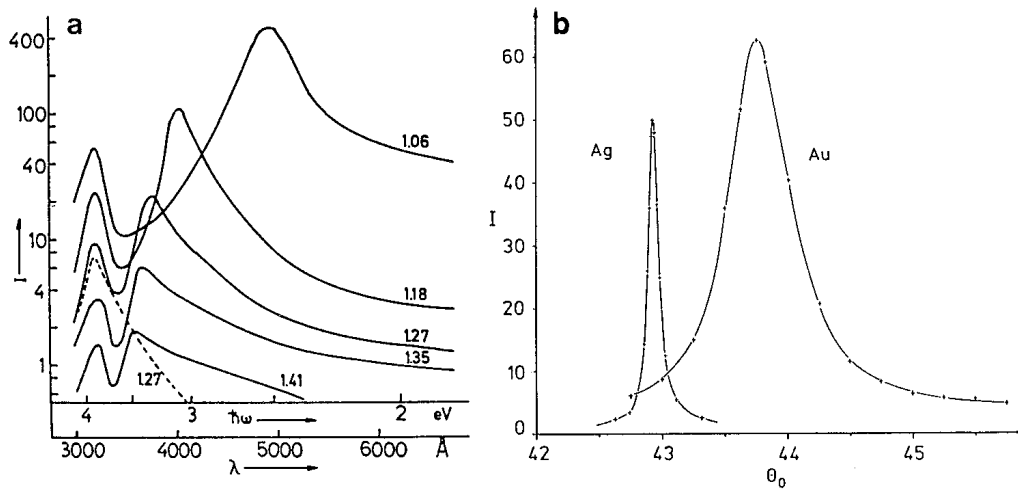

Fig. 3.2. (a) Light emission of a rough surface, $\delta{\sim}5\,\text{Å}$, due to the coupling of photons with SPs, see Fig. 3.1 bottom left. The resonance excitation of the SP produces an enhancement $|t^p_{012}|^2$ of the electromagnetic field *in* the film surface which becomes higher with longer wavelengths. The emitted intensity is plotted (a) as a function of the wavelength of the incoming light λ at a fixed angle of incidence. The maxima of excitation at different wavelengths λ demonstrate the enhancement of the radiation field and reflect the dispersion relation of the SP. Note the logartihmic scale! A secondary effect is seen: At $\lambda = 3200\,\text{Å}$ silver has a maximum of transparency which appears also in the measurements with s-polarized light (- - -) and which comes from light scattered at the interface silver/quartz. From [2.8]. (b) The same light emission as a function of the angle of incidence θ_0, for Ag and Au at constant λ. The enhancement of the emitted radiation in resonance is evident. Different sensitivities for both metals have been used. Both curves demonstrate a Lorentzian profile. From [2.9]

41

3.2 Measurement of the Roughness

Theoretical Remarks

The strong intensity of the scattered light in Fig. 3.2 can be used to derive the roughness parameters of this silver surface. The theoretical relations of this process have been developed in 1974 by *Kretschmann* [3.1] and have been applied to evaluate the experimental data. The relation of the intensity dI emitted into the solid angle $d\Omega$, with I_0, the intensity of the incoming p-polarized light, is given in a first or linear approximation with $\delta \ll \lambda$ (phase change in z direction neglected) and $\delta \ll \sigma$ by

$$P = \frac{1}{I_0}\frac{dI}{d\Omega} = \frac{1}{4}\left(\frac{\omega}{c}\right)^4 \sqrt{\varepsilon_0}\frac{|W(\theta)|^2}{\cos\theta_0}|t^p_{012}|^2|s(\Delta k_x)|^2 \ , \tag{3.1}$$

where θ_0 is the angle of incidence; $|t^p_{012}|^2$ Fresnel's coefficient of the two interface system quartz/metal/air, (2.25); $|s(\Delta k_x)|^2$ the Fourier transform of the roughness correlation function, (2.47); and $|W(\theta)|^2$ the dipole function. The latter two functions both determine the angular distribution of the emitted radiation. The dipole function $|W|^2$ represents the angular radiation characteristic of the intensity distribution of one single emitter, whereas $|s(\Delta k_x)|^2$ describes its correlation with the surrounding dipoles and thus the coupling of the photons with the roughness, see Sect. 2.9. The term Δk_x has been explained in (2.50). The emitted intensity is proportional to $\sqrt{\varepsilon_0}$, ε_0 is the dielectric function of the half cylinder, mostly SiO_2.

The term "linear" approximation stems from the development of the field above the rough surface, here the magnetic field H_y :

$$H_y(z) = H_y(0) + S(x)\left(\frac{\delta H_y}{\delta z}\right)\bigg|_{z=0} \ . \tag{3.2}$$

For calculating the intensity of the emitted light the value of $\overline{H_y^2}$ is needed, so that due to $\overline{S} = 0$, $\overline{S(x)^2} = \delta^2$ (2.44) comes into effect. Thus the linear approximation gives a dependence quadratic in δ.

The function $|W(\theta)|^2$ can be split up into the three components W_x, W_y, and W_z, which can be represented as follows: One of the theoretical approaches to get (3.1), is to start with the model of polarization currents induced by the incoming electromagnetic field. This current has three components, x, y, and z, each acting as a Hertz dipole on a metallic surface. The three components of the Hertz dipole can now be associated with the three components of $W(\theta)$. The relative positions of the plane of observation and the plane of incidence, measured by the angle ϕ, determine which components come into play.

The usual method is to make observations at $\phi = 0$, i.e., the two planes (1,2), see Fig. 3.3, are parallel. The dipole function for $\phi = 0$ is given by [3.2,3]:

$$|W(\theta)|^2 = A(\theta,\varepsilon_1)\sin^2\Psi\left|\left(1 + \frac{\sin^2\theta}{|\varepsilon_1|}\right)^{1/2} - \sin\theta\right|^2 \quad \text{with} \tag{3.3}$$
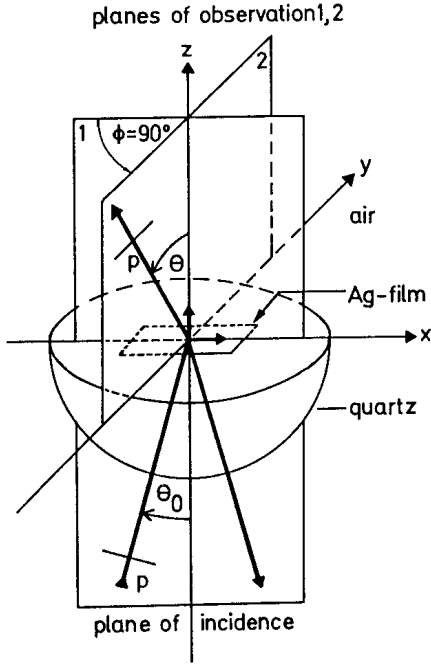
Fig. 3.3. Experimental arrangement for the observation in the plane of incidence *(1)* and in a plane of observation *(2)* inclined by an angle ϕ agains plane *(1)*. θ_0 : angle of incidence, θ : angle of observation; p indicates the direction of polarization. If the polarization p lies perpendicular (parallel) to the plane of observation, it is called s polarization (p polarization). The two short arrows at the origin denote the x and z component of the radiating dipole. From [2.4]

$$A(\theta, \varepsilon_1) = \frac{|\varepsilon_1| + 1}{|\varepsilon_1| - 1} \frac{4}{1 + \frac{1}{|\varepsilon_1|} \text{tg}^2 \theta} \quad . \tag{3.4}$$

The angle Ψ means the angle of the plane of polarization and the plane of observation: for $\Psi = 0°$ both planes are perpendicular (s polarization) and for $\Psi = 90°$ both planes are parallel (p polarization).

Equation (3.3) shows that s-polarized light, i.e., light which vibrates perpendicular to the plane of observation or $\Psi = 0$ does not exist theoretically in this linear approximation. The emitted light (p light) has its maximum in the backward direction as Fig. 3.4 demonstrates, a result of the interference of the light emitted by the tangential (x) and the normal (z) component of the dipole. This behavior can be seen immediately from (3.3): if the term $\sin^2 \theta / |\varepsilon_1|$ is neglected against 1, the relation $(1 - \sin \theta)^2$ yields a larger value for $\theta < 0°$ than for $\theta > 0°$ (the forward direction).

The theoretical result of Fig. 3.4 cannot be verified directly in the experiment since the unknown factor $|s(\Delta k_x)|^2$ has a strong influence and changes the angular distribution of the emitted light as Fig. 3.5 displays. This gives the possiblity to determine $|s(\Delta k_x)|^2$.
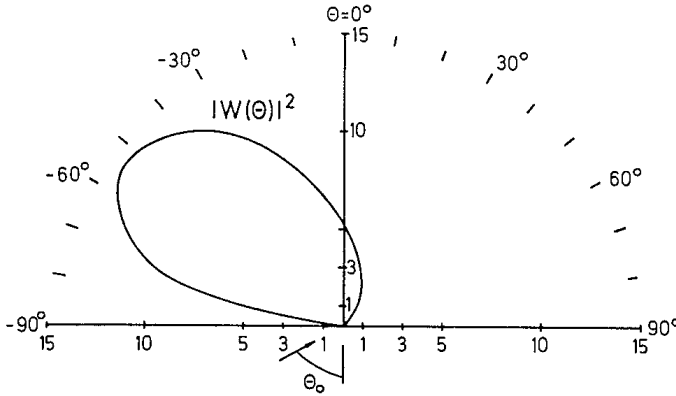
Fig. 3.4. Calculated dipole function $|W(\theta)|^2$ for $\phi = 0$, $\lambda = 5500\,\text{Å}$, silver, $\theta_{\max} = -55°$, which does not change significantly with λ. The preferred backward scattering is remarkable, a result of the interference of the light emitted from the x and z component of the dipole. The roughness function $|s(\Delta k)|^2$, see (3.1), turns the lobe more or less to the right, see Fig. 3.5. From [2.4]
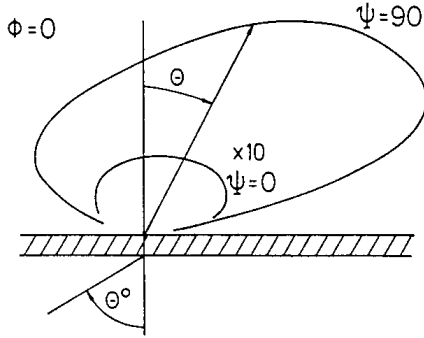
Fig. 3.5. Intensity distribution from a rough surface at $\Psi = 0$. θ_0 and θ are the angles of incidence and observation. The incoming light is p polarized. The angular distribution of the p light ($\Psi = 90°$) is determined essentially by the roughness. A weak s light ($\Psi = 0$), 10 $\times$ enlarged, is observed, forbidden in the linear approximation. From [3.2]

Additional Remark

It is of interest to look also at the case $\phi = 90°$, crossed planes 1, 2 see Fig. 3.3, since this configuration allows a control of the theoretical concept. The calculated dependence for $\Psi = 0$ gives roughly for $|\varepsilon| \gg 1$

$$|W|^2 \cong A(\theta, \varepsilon) \cos^2 \theta \qquad \text{and for } \Psi = 90° \qquad (3.5)$$

$$|W|^2 \cong A(\theta, \varepsilon) \sin^2 \theta \ .$$

For more accurate expressions see [3.2]. The roughness has practically no influence since δk_x changes very little between $\theta = +90°$ and $-90°$, see (2.50). Turning the detector around the x axis in the plane of observation (y, z) with the analyzer perpendicular to the plane of observation ("s-polarized" light) we look at the x component of the dipole and expect the distribution $\Psi = 0$ in Fig. 3.6. In the case where $\Psi = 90°$, the polarizer in the plane of observation, we expect a double-lobed distribution of the y component of the dipole. Both distributions of $\Psi = 0°$ and $\Psi = 90°$ are measured and agree with the calcu-

44
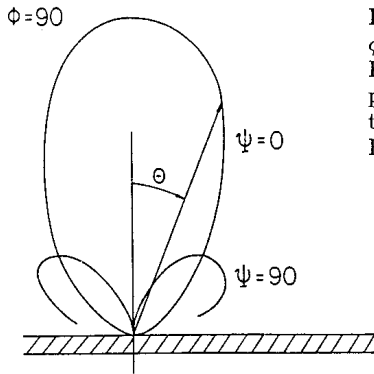
Fig. 3.6. Intensity distribution from a rough surface at $\phi = 90°$, turning the detector around the x axis, see Fig. 3.3, with the analyzer perpendicular ($\Psi = 0$) and parallel to the plane of observation ($\Psi = 90°$). θ means the angle of observation. Silver, 700 Å thick, $\lambda = 5000$ Å. From [2.4]

lated data [3.2]. At $\theta = 90°$ a small rest intensity indicates that deviations of the linear theory come into effect, see Fig. 3.12.

Experimental Remark

The experimental arrangement to measure the angular intensity distribution is shown in Fig. 3.7, suitable for reflection and scattering. At the air/metal interface of the metal film, SPs are excited. The film is deposited by evaporation on fire-polished quartz plate (≈ 1 mm thick) which is stuck on the base of a prism or half cylinder (P) using an immersion oil for optical contact. This system is fixed on a goniometer (G). The light beam (L), laser, or xenon high-pressure lamp plus monochromator, passes the chopper (C), the prism polarizers (P1, P2), the diaphragm (BL1), and a cylindrical lens ZL to compensate the refration at the cylindrical surface so that nearly parallel light hits the surface of the metal film. The detectors are either photomultipliers (PM) or photodiodes
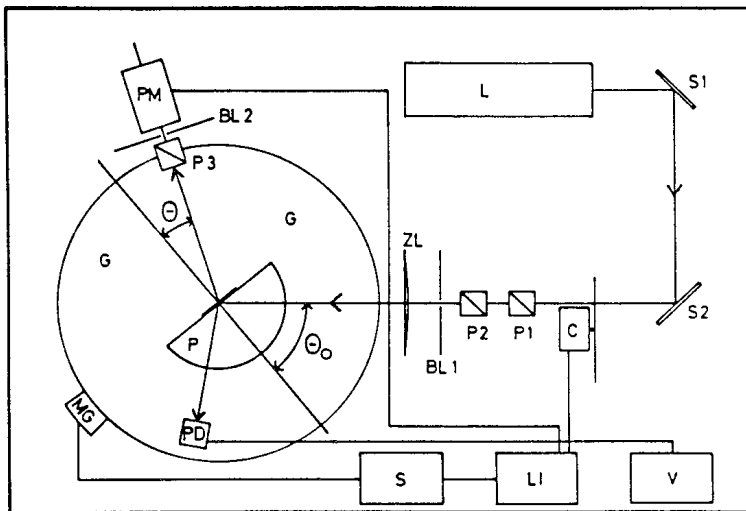
Fig. 3.7. Scheme of the experimental arrangement to measure the angular distribution of the light emission in reflection as a function of θ_0 (incoming light) or of the scattered light as a function of θ at a given θ_0. From [2.4]

(PD). The signals are recorded by the lock in (LI) or amplified in (V) and plotted in (S). Calibration is made by marks through MG. This arrangement has been improved [3.4] by replacing the goniometer with two separated rotary tables of a diameter of ≈ 60 cm; the system P is mounted on the interior table, whereas the detectors are fixed on the exterior, both driven by stepping motors. The whole unit is enclosed in a box into which the light beam enters through a small diaphragm, which improves the signal-noise ratio. The manipulations are performed electrically from the exterior. For the observation in a plane different from that of the plane of incidence ($\phi > 0$), the two rings can be inclined against each other. They can also be displaced by ca. 7.5 cm to measure the emitted light along the surface of, e.g., a wave-guide system.

The accuracy of the position θ_0 amounts to $\Delta\theta_0 = 0.01°$ (absolutely); that of θ regarding the accuracy of the determination of the edge of total reflection (0.02°) gives $\Delta\theta = 0.04°$; the divergence of the laser is some 0.01°, and that of the xenon lamp plus monochromator is 0.05° at a spectral width of a few angstroms.

With the accuracy given above, it has been noticed that after evaporation the resonance minimum (or maximum according to the method used) displaces to smaller angles and its half width gets narrower in the first hour by the order of approximately 1 %. This has been stated for silver measured in air [2.9] as well as for silver films prepared and measured in a vacuum, some 10^{-7} Torr [3.5] and $3-4 \times 10^{-8}$ Torr [3.6] without being exposed to air. Apparently recrystallization comes into play in the first hour.

The measurements were in general performed after enough hours had elapsed for SP data to remain constant. After one day the samples exposed to air change due to contamination; these data are not used.

The sensitivity of the method has been considerably improved, so that relative displacements of 4×10^{-4} deg were detected in a vacuum chamber of $3-4 \times 10^{-8}$ Torr [3.6]. Processes of absorption have been studied, e.g., the absorption of O_2 of about 2 % of a monolayer on clean silver films could be detected. The height of the scattering maximum allows observation of changes of the surface roughness. For more details see [3.6].

Most of the experiments on SPs are carried out with silver, which has a number of advantages: as a noble metal it resists chemical reactions to a high degree. The optical properties are favorable, since ε'' in the visible region is small, e.g., compared to gold, so that the damping of the SPs is small, see (2.6). At $\lambda = 6000$ Å the value of $\varepsilon''/2|\varepsilon'|^2$ for silver is 1×10^{-3}, however, for gold it is 1×10^{-2}. Small changes of the position and width of the ATR minimum can thus be detected. Furthermore the energy of the volume plasmon (3.78±0.02 or $\lambda = 3270$ Å) and of the surface plasmon (3.6±0.02 or $\lambda = 3450$ Å) are rather close, due to the band structure of silver, and in a spectral region accessible to usual lasers. Finally, silver is a metal which has no difficulty in forming continuous films of a thickness of about 10^2 Å and more by evaporation.

46

Determination of the Roughness Parameters

The configuration $\phi = 0$ is of special interest because it allows us to measure the roughness function $|s(\Delta k_x)|^2$ using (3.1). The value $P(\theta) = (1/I_0)dI/d\Omega$ is measured, and the factor $|t^p_{012}|^2$ as well as $|W(\theta)|^2$ are calculated with the $\varepsilon_1(\omega)$ obtained from fitting the ATR minimum of the silver surface in situ, see Sect. 2.5 so that one obtains $|s(\Delta k_x)|^2$. The plot $\ln|s(\Delta k_x)|^2$ as a function of $(\Delta k_x)^2$ can be described in the linear region, $\Delta k_x > 10^{-3}\,\text{Å}^{-1}$, by a Gaussian correlation function, see Fig. 3.8:

$$\ln|s(\Delta k_x)|^2 = \ln\tfrac{1}{4}\delta^2\sigma^2 - \tfrac{1}{4}\sigma^2\Delta k_x^2 \ . \tag{3.6}$$
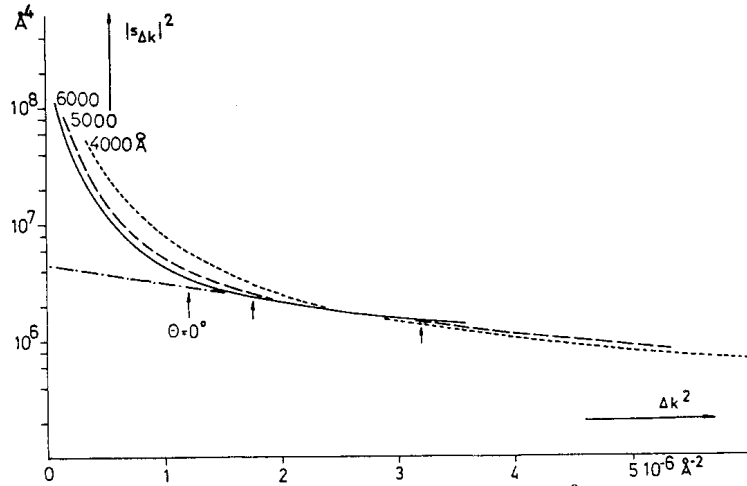
Fig. 3.8. Observed roughness function $|s(\Delta k_x)|^2$ as a function of $(\Delta k_x)^2$ for a silver film, 550 Å thickness, at different wavelengths. The arrows indicate $\theta = 0°$ or $\Delta k_x = \sqrt{\varepsilon_0}(\omega/c)\sin\theta_0$, the observation is along the normal of the surface. The solid angle of the light detector is $\delta\Omega = 4 \times 10^{-3}$ sr. The back-scattered light, right side of the curve, is determined by the roughness of the silver surface. From [3.1]

The slope yields σ and the linear extrapolation to $\Delta k_x = 0$ gives δ. The values of the roughness parameters obtained with this method are collected in Table 3.1 [3.12]. They are measured in the Δk_x region given in the Table 3.1.

The strong forward scattering at $\Delta k_x \lesssim 1 \times 10^{-3}\,\text{Å}^{-1}$ which shows an intensity varying with the substrate is remarkable. This Δk_x region indicates

Table 3.1. Observed roughness parameters of silver films [3.12]

δ [Å]	σ [Å]	Δk_x [Å^{-1}]	d (Ag) [Å]	Reference
7	1180	$(0.5 - 3) \times 10^{-3}$	400–900	3.1,2
4–5	850	$(1 - 2.7) \times 10^{-3}$	500	3.7
5–7		$(1 - 2.2) \times 10^{-3}$	350	3.8
5–7		$(1 - 2.5) \times 10^{-3}$	400–850	3.9
7	800±150	$(1 - 2.2) \times 10^{-3}$	540	3.4
5			1000	3.11
6	1400		550	3.10

47

roughness components of rather long wavelengths $\Lambda = 2\pi/\Delta k_x$ in excess of 1μ [3.1]. This has been interpreted as due to a waviness of the fire-polished quartz plates which serve as a substrate and which may be caused by the production process. It is interesting that such excess scattering at low Δk_x values has also been observed at highly polished surfaces of Zerodur, see Fig. 5.10b. This waviness at $\theta > 0°$ is characteristic for the substrate, whereas the linear part of Fig. 3.8 or mainly the backward lobe shown containes the information of the roughness of the silver film.

This interpretation is supported by two experiments:

a) If the quartz substrate is replaced by a "supersmooth" quartz plate, the forward scattering diminishes drastically, see Table 3.2. This improves the quality of measurements considerably.

b) If the metal film is roughened by underlying crystalline material such as CaF_2, MgF_2, etc., the forward scattering is reduced in favor of the backward scattering, compare Fig. 4.5 and 3.8. Thus the linear part of $\ln |s(\Delta k_x)|^2$ is extended and the accuracy of the (δ, σ) determination is improved.

Experiments of the same type under comparable conditions have been performed by *Braundmeier* and *Hall* [3.13]. The experimental results are essentially in agreement with the observed phenomena just described: the appearance of a strong forward lobe and a backward lobe. After what has been said, the waviness of the quartz substrate has a strong influence on the intensity of the forward lobe, so that the angular distributions can vary. An evaluation of the angular intensity distribution to get the roughness parameters has not been made since the interpretation of the backward lobe failed due to an error in the computer programm [3.14].

Similar measurements of the roughness of evaporated copper films have been published [3.15]. The authors could not reliably derive the $|s(\Delta k_x)|^2$ function from the data observed at their films. They could, however, calculate a lower limit of δ of Cu films of 5000 Å thickness on quartz: $\delta > 4.4$ Å and Cu on mica: $\delta > 5.8$ Å. In experiments with aluminum films, ≈ 340 Å thick, using the ATR device for the generation of the second harmonic (see Fig. 2.30) the roughness has been determined from the scattered 2ω light. The values obtained are: $\delta = 25$ Å and $\sigma = 1390$ Å [3.16].

Table 3.2. Comparison of values of the roughness spectrum $|s(\Delta k_x)|^2$ for silver films ($d = 500$ Å) evaporated on "smooth" and "supersmooth" quartz substrates, for $\Delta k_x < 1 \times 10^{-3}$ Å^{-1} [3.8]

$\Lambda = 2\pi/\Delta k_x$ [Å]	$|s(\Delta k_x)|^2$ [Å^4]	
	Supersmooth	Smooth
10 000	4×10^6	12×10^6
15 000	7×10^6	35×10^6
20 000	1×10^6	73×10^6

These experiments have been performed in the quartz/metal/air configuration, see Fig. 2.8. Scattering measurements in the quartz/air/metal configuration which are less convenient to handle, have also given $\delta \sim 5$ Å at thin silver films [3.11].

One has to bear in mind that the experiments with scattering of light for x-rays yield values of the roughness parameters only in a limited Δk_x region given by the scanned θ region, which is approximately $2 \times 2\pi/\lambda$, in the region of visible light 1–2.5×10^{-3} Å^{-1} (see Table 3.1) and for x-rays 1.5×10^{-5} up to some 10^{-4} Å^{-1}. It is an open question whether the whole Δk_x region can be described with one Gaussian function and the same two parameters; to get this information these measurements have to be made with different wavelengths on the same sample.

The profile of a statistically rough surface is, in the case of an evaporated metal film, given by the arrangement of crystals of different diameter and exterior shape. One can conclude from the results discussed in this chapter, that such an arrangement can be described in the region of visible light by a Gaussian correlation function.

3.3 Directional Scattering

On a rough surface the SPs are scattered *in* the surface out of the direction of k_x without changing its value, "directional scattering", see Fig. 3.9:

$$\overline{\Delta k} = \overline{k} - \overline{k_x} \tag{3.7}$$

with $|k| = |k_x|$. The plasmons take up different values of $|\Delta k| = 2|k_x| \sin \phi/2$ from the roughness spectrum and are deviated by different angles ϕ. These deviated SPs propagate in the metal surface and emit light under the reflection angle into the backside of the metal, see Fig. 3.10, a process which has been described in [3.10,17]. By the way, this is still a first-order interaction. The angle ϕ varies between $0°$ and $180°$, so that a light circle is produced which can be photographed, see Fig. 3.11.

The intensity along this circle is proportional to the roughness function $|s(\Delta k)|^2$ and thus allows derivation of the roughness parameters δ and σ [3.10]. The result of this evaluation of silver films, 500 Å thick, are given in Table 3.1 with $\delta \sim 6$ Å and $\sigma \sim 1400$ Å in agreement with the results obtained from the observations on the light scattered into the air side.

The radiation scattered back into the ε_0 side results from the following processes: The incoming field permeates the silver film and excites the resonance field at the metal-air surface. This field penetrates back through the metal film and has therefore to be multiplied with $|t_{210}^p|^2$ so that the light scattered back comes out as [3.10]:

$$\frac{1}{I_0} \frac{dI}{d\Omega}\bigg|_{\text{back}} = 4 \left(\frac{\omega}{c}\right)^4 |t_{012}^p|^2 |t_{210}^p|^2 W(\theta_i, \theta_s, \phi) |s(\Delta k)|^2 \tag{3.8}$$
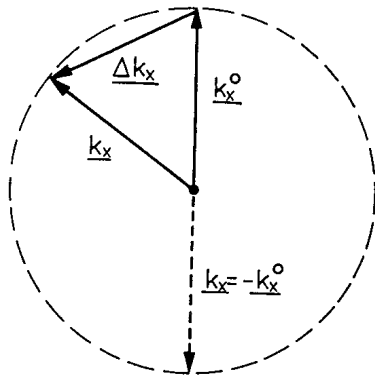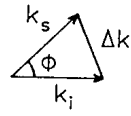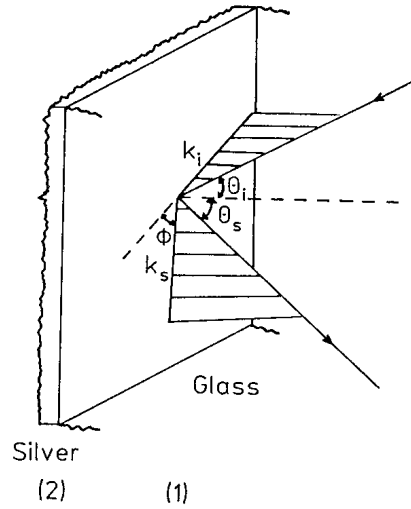
49

Fig. 3.9. The SP with the wave vector k_x^0 is scattered without changing its absolute value: "directional" scattering

Fig. 3.10. Scheme to illustrate the "directional" scattering phenomenon. From [3.10]

This equation displays two enhancement factors, one for the incoming, the second for the scattered light.

It is the same result which has been found in later calculations of SERS theory; the difference is that there the scattered light has suffered a small energy loss by the excitation of Raman transitions. Here one regards the elastic scattering.

The back-scattered field is determined by the reverse Fresnel transmission factor 210 instead of 012 which contains the same resonance denominator,
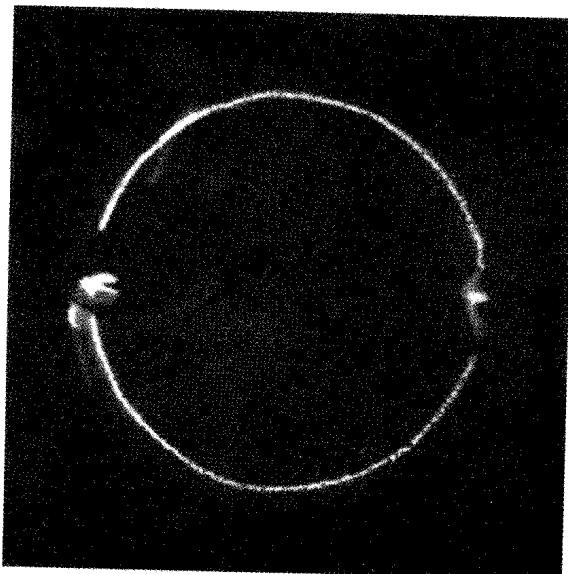

Fig. 3.11.The light circle emitted from the SPs back into the quartz. The SPs are scattered in the rough surface of the thin silver film. It is photographed directly exposing the (photographic) film. From [3.10]

since $r_{21} = -r_{12}$, see (2.17), so that its relative intensity is proportional to $[1 + r_{01}r_{12}\exp{(i2k_{z1}d_1)}]^{-4}$. Comparing the relative intensity scattered into the air space (3.1) and into the glass side, one must notice that the angular functions $W(\theta, \phi)$ and $|s(\Delta k)|^2$ are not identical. Choosing special experimental conditions, good agreement of both the intensities, calculated and observed, has been found [3.10].

In addition this back-reflected light is strong on account of the rather narrow resonance width, at least in silver, so that the angular width of the circle is

$$\theta^{1/2} = 2\Delta\theta = 2k_x''(\omega/c\cos\theta)^{-1} \tag{3.9}$$

e.g., at $\lambda = 5500\,\text{Å}$, $\varepsilon_1'' = 0.5$, $\varepsilon_1' = -12$, amounts to $10^{-3}\,\text{rad}$.

It is thus possible to photograph the light circle directly on a photographic film, see Fig. 3.11.

3.4 Surface Roughness and "Volume" Roughness

Ideal surface roughness has been assumed, i.e., it is taken for granted that the radiating dipoles fed by the polarization current are distributed on a surface (the fictive surface $z = 0$ in Fig. 2.34). It is, however, possible that the "roughness" is due to inhomogeneities in the bulk [3.18,19] which can be described as spatial fluctuations of the dielectric function $\varepsilon_1(\omega)$:

$$\varepsilon_1(x, y, z) = \bar{\varepsilon}_1 + \Delta\varepsilon_1(x, y, z) \tag{3.10}$$

with $\bar{\varepsilon}_1$ the average dielectric function and $\Delta\varepsilon_1$ the fluctuations about $\bar{\varepsilon}_1$.

A detailed theoretical study [3.19,20,21] has shown that for volume scattering, the z component of the dipole $W : W_z$ has to be replaced by $W_z' = W_z/|\varepsilon_1'|$ due to the continuity condition at the boundary for the field $D_z = \varepsilon_1' E_z$. Working with wavelengths of $\lambda = 5000\,\text{Å}$, where $\varepsilon_1(\omega) = -9.4 + i0.37$ in silver, a strong difference is expected for W_z' in the case of surface scattering with $|\varepsilon_1'| = 1$ and volume scattering with $|\varepsilon_1'| = 9.4$. This difference has a strong influence on the quotient $I(\Psi = 90°/I(\Psi = 0°) = I_p/I_s$ measured in the $\phi = 90°$ configuration, see Fig. 3.12. The calculated quotients are

$$\left(\frac{I_p}{I_s}\right)_{\text{surf.}} = \frac{\text{tg}^2\theta}{1 + \frac{1}{|\varepsilon_1'|}\text{tg}^2\theta}$$

$$\left(\frac{I_p}{I_s}\right)_{\text{vol.}} = \left(\frac{I_p}{I_s}\right)_{\text{surf.}}\frac{1}{|\varepsilon_1'|^2} \cdot \tag{3.11}$$

The observed data in Fig. 3.12 demonstrate that the light is produced by surface roughness. Figure 3.12a further demonstrates that the value I_p/I_s does not go to zero with $\theta \to 0°$. The reason for this deviation is the multiple scattering
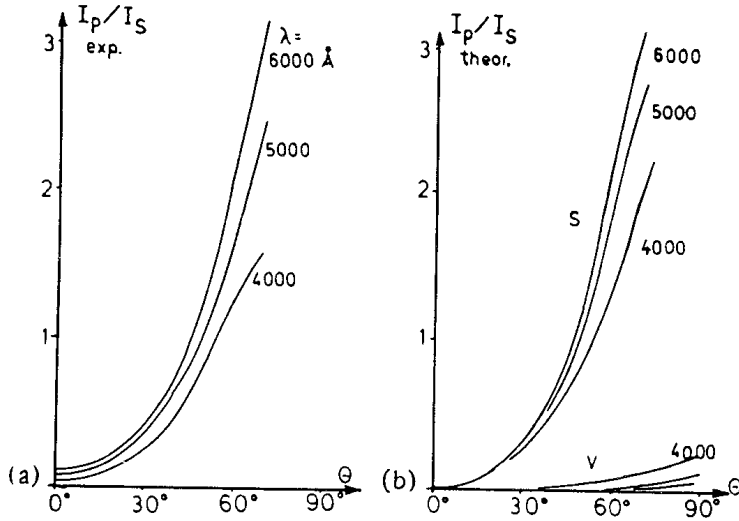
Fig. 3.12. The ratio $I(\psi = 90°)/I(\psi = 0°)$ at $\phi = 90°$ or I_p/I_s, is plotted as function of θ, measured against the z direction, for surface (s) and volume (v) scattering at different wavelengths. The experimental data agree with the surface scattering concept confirming that (nonradiative) SPs are responsible for a light emission. From [3.2,3]

of SPs; this has been confirmed by the observation that the "rest intensity" increases with δ^2 [3.21].

The experimental results demonstrated that the nonradiative SPs interact with surface roughness.

Volume Roughness and Radiative SPs

The dispersion relation of the radiative SPs lies left of the light line, see Fig. 2.2. It starts at small k_x with $\omega = \omega_p$ and increases for $\frac{1}{2}k_p d \ll 1$ as

$$\omega = \omega_p \left[1 + \frac{1}{2} \left(\frac{k_p d}{2} \right)^2 \left(\frac{k_x}{k_p} \right)^2 \right] . \tag{3.12}$$

Its damping grows with k_x

$$\frac{1}{\omega\tau} = \left(\frac{k_x d}{2} \right)^2 \left(\frac{k_x}{k_p} \right)^2 \tag{3.13}$$

(see [2.3b]). One recognizes these properties in Fig. 2.2.

The damping is due to light emission since the radiative SPs are directly coupled with photons lying inside the light cone, so that k_x of the SPs is identical with k_x of the light.

These radiative SPs are observed in transmission of a thin film of silver scanning the frequency of a p-polarized light beam, which passes a silver film, see Fig. 3.13, a pronounced dip in the transmitted light is seen for $\hbar\omega = \hbar\omega_p = 3.8\,\mathrm{eV}$ ($\lambda = 3250\,\text{Å}$) indicating the resonance excitation of radiative SPs [3.22]. The film has to be inclined against the direction of the incoming beam, so
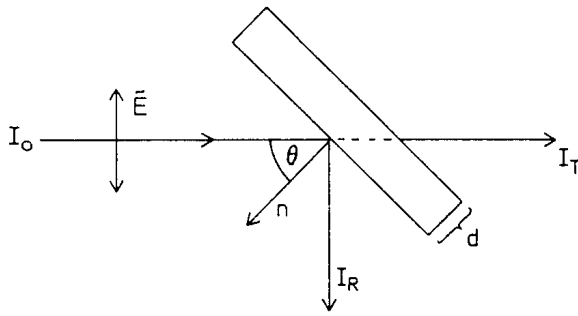
Fig. 3.13. Schematic figure of the experimental arrangement to observe plasma resonance absorption and emission. From [2.3b]

that the E_z component of the E vector of the light (the z direction is the direction normal to the film) can excite the radiative SPs. It corresponds to the high-frequency mode ω^+ of the nonradiative SPs.

These modes are also observed in reflection: If a p-polarized light beam is incident on a silver film under the angle θ_0, one expects a specular reflected beam at θ_0. The experiments, however, show that in addition radiation is detected in a large angular region if the frequency exceeds $\omega = \omega_p$. The explanation is given in Fig. 2.2: a continuum of roughness vectors distributes the light emission inside the light cone, due to the nearly horizontal dispersion relation $\omega = \omega_p$ for $k_x < k_p$ [3.23–25].

The detailed study of this phenomenon had the result that the roughness is due to volume or interior roughness mentioned above: The theoretical considerations show that in this case the z component of $W(\theta)$ has to be replaced by $W(\theta)' = W(\theta)/|\varepsilon_1'|$, which predominates for $|\varepsilon_1'|$ being very small at $\omega = \omega_p$. This has the consequence (a) that the scattered intensity I_p/I_s comes out as a function of $1/|\varepsilon_1'|^4$ which produces a strong intensity maximum at $\omega = \omega_p$ in agreement with the observations [3.24,25], see Fig. 3.14, and (b) that the angular distribution of the scattered light is essentially determined by a dipole in the z direction, the normal of the surface. It follows that I_p/I_s, the quotient of the scattered p-polarized intensity and the s-polarized light, as a function fo the angle of observation θ has larger values than for surface scattering [3.26].
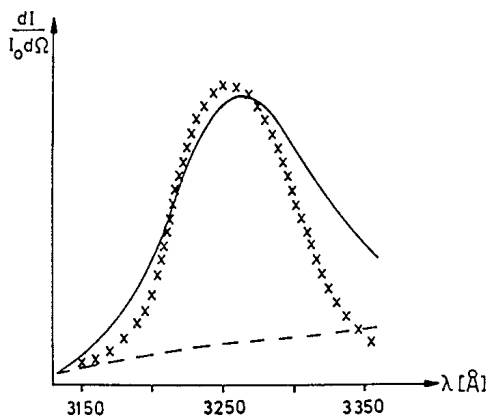

Fig. 3.14. Light intensity of scattered (radiative) SPs around the plasma frequency (3250 Å) of silver (500 Å thick). $\theta = \theta_0 = 30°$. (———): calculated volume contribution; (- - -): calculated surface contribution; (x x x): observed data. From [3.26]

Both dependences, the intensity as a function of λ as well as its angular distribution are in agreement with the concept of volume roughness responsible for the emitted radiation.

3.5 Roughness Measurement
with the Tunnel Electron Microscope

The small values of the r.m.s. height δ on silver films evaporated on glass or quartz substrates obtained with light scattering methods can be controlled by direct methods. The application of the tunnel electron microscope which has a resolution of ≈ 1 Å perpendicular to the surface, and in the surface of about 10 Å, confirms the mean roughness of ≈ 5 Å obtained from light scattering, as Fig. 3.15 displays [2.19].

This method can be extended to surfaces of higher roughness and promises to become a useful nondestructive procedure to determine surface corrugations. It further allows comparison of roughness data with those obtained by the light scattering method.
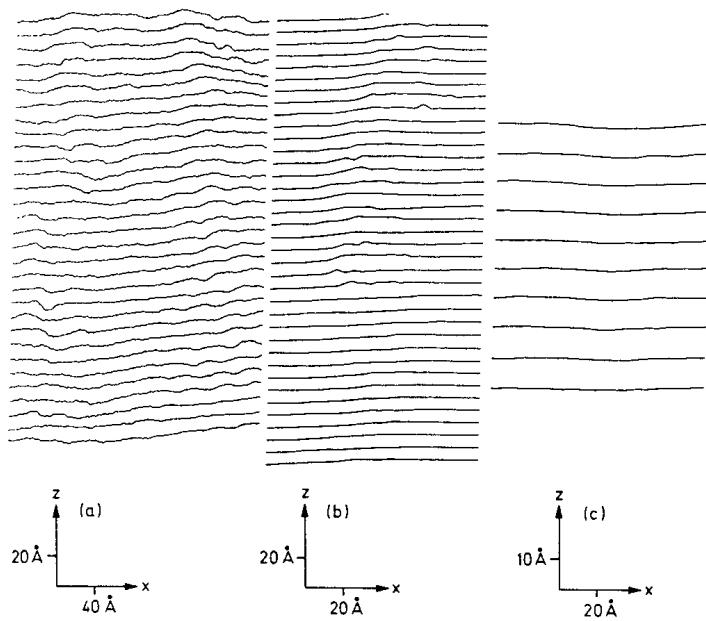
Fig. 3.15a–c. Tunnel microscope picture of a vaporized silver film, 500 Å thick. Along the lines the tunnel current is constant. The scale in the z and x directions is indicated; the different lines in the y direction are registered within a distance of 5–10 Å. Each reproduced section correlates to about 250 Å. The sections show regions of smoothness of in general 5–10 Å (a) alternating with regions smaller than 5 Å (b). Large areas are very smooth (c). Sometimes irregularities around a dust particle, probably, are observed. From [2.19]

3.6 Roughness on Planar Wave Guides

As mentioned in Sect. 2.6. the ATR method can be used to excite modes in a wave guide which is built up as a layer system, e.g., quartz/silver, 350 Å thick/LiF 1.39 μ thick/air. When resonance occurs, the excitation can be detected by the light reflection minimum or the light scattering maximum via roughness, see Fig. 3.1. A detailed study showed that the source of light emission is essentially the interface LiF/air [3.27]. The evaluation of the angular distribution of the scattered light as it has been described above, yields values of $\delta = 40$–50 Å independent on λ and $\sigma = 500$ Å. The authors point out that the field in a wave guide has its maximum not in the surface but more in the interior; thus it is possible that the first-order approximation is more suitable for rougher surfaces with light modes than for such with SPs. This result is supported by the good agreement of observed and calculated positions and half widths of the modes using this linear approximation. An effect of the roughness on the dispersion relation is not observed.

As an example the observed reflection curves at a layered system are reproduced for different modes in Fig. 3.16. The narrow minima belong to the s or TE modes, the electric field being perpendicular to the plane of incidence, the broader minima belong to the p or TM modes. This difference stems from
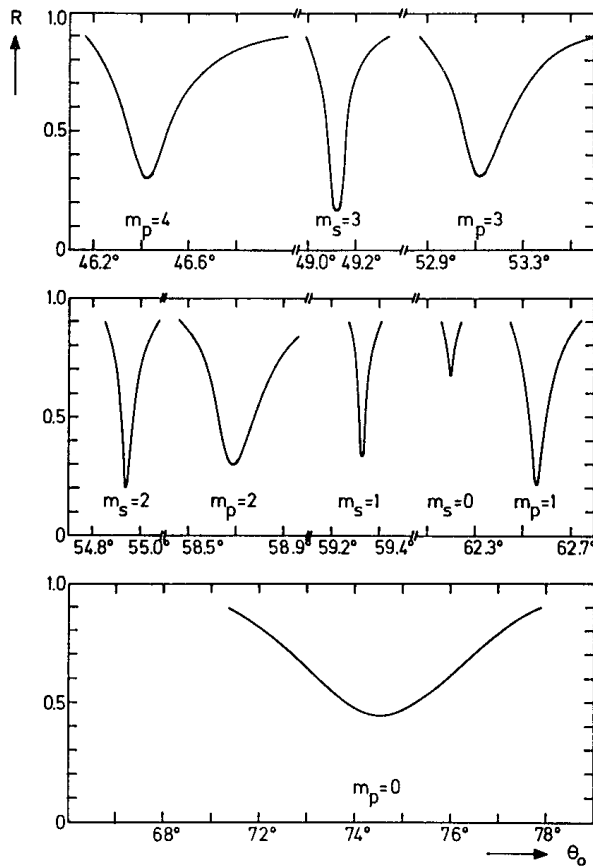
Fig. 3.16. Measured reflection curves at a layered system: quartz/silver/LiF, produced by resonance excitation of different planar waveguide modes in LiF: TE_0–TE_3 and TM_0–TM_4. From [3.27]

55

the field distribution: the fields of the p modes dip more into the metal than the fields of the s modes, so they are absorbed more strongly. A comparison of observed values of θ_0 and $\Delta\theta_0^{1/2}$, position and half width of the resonance minima, and calculated values gives good agreement, see Table 3.3.

Table 3.3. Comparison between experimental and convoluted data of the resonance minima for the s modes at the wavelength $\lambda = 5309\,\text{Å}$; conv. means that the calculated data are convoluted with the laser beam divergence of $0.03°$

m_s	θ_0 (deg)		$\theta_0^{1/2}$ (deg)	
	exp.	conv.	exp.	conv.
0	62.20	62.20	0.05	0.05
1	59.34	59.31	0.05	0.07
2	54.94	54.86	0.08	0.08
3	49.11	49.14	0.11	0.11

Light scattering experiments on planar glass wave guides of $0.65\,\mu$ thickness have been reported in [3.28]. As expected they are somewhat smoother than the crystalline LiF films at the boundary air/glass.

A similar result comes out for wave guides with sinusoidally corrugated surfaces [3.29], see also Sect. 6.6.

3.7 Enhancement of Inelastic Light Scattering (Brillouin Scattering)

Thermally excited surface acoustic waves produce surface ripples on surfaces of different materials, the transverse component of the Rayleigh modes. These surface phonons with frequency ω_R and wave vector q_R have been observed using light inelastically scattered at these moving gratings (Brillouin scattering) [3.30]. A phonon of this type at a frequency $\nu_R = 6 \times 10^9\,\text{s}^{-1}$ has a wave vector of q_R of several $10^{-3}\,\text{Å}^{-1}$ and a wavelength of some $10^3\,\text{Å}$. Surface plasmons on an ideally smooth surface do not radiate. However, when Rayleigh waves are switched on the SPs couple with them so that surface waves of $\bar{k}_x \pm \bar{q}_R$ with an energy $\hbar\omega \pm \hbar\omega_R$ are produced. Since the wave vectors q_R are comparable to those of the SPs (e.g., SPs with $\lambda = 5000\,\text{Å}$ or $\hbar\omega \sim 2.5\,\text{eV}$ have a $k_x = 6 \times 10^{-3}\,\text{Å}^{-1}$), the SPs are scattered into the light cone, for each phonon q_R into another direction, with an energy change of $\pm\hbar\omega_R$ (a few $10\,\text{meV}$). In the resonance maximum of the SP excitation, a strong enhancement of the emitted light is therefore expected. The unavoidable roughness of the surface yields an elastic component which has been discussed in this chapter.

The experiments were performed with a five-pass interferometer, to separate the small frequency difference of several $10\,\text{GHz}$ of the elastic and inelastic component [3.31]. When the ATR minimum showed maximum excitation, the

inelastic as well as the elastic scattered light exhibited a maximum. The enhancement comes out to be about 25. The comparison has been made against the intensity observed without ATR excitation, see Chap. 5, Fig. 5.1. Regarding the angular function of the devices with and without ATR, the value of the enhancement differs from $|t^p|^2$, see also the remark to (5.1).

4. Surfaces of Enhanced Roughness

In the following the results obtained on rougher surfaces are resumed: Besides the light emission, a change of the dispersion relation compared to that of a smooth surface is observed. Whereas the light emission comes out in the first-order approximation, a higher order approximation is necessary to describe the influence on the dispersion relation, which is a consequence of multiple scattering. How the enhancement changes at rougher surfaces is not yet known. The situation is clearer at very rough surfaces, here the model of "localized" plasmons allows a rather good understanding of the observations.

Rougher surfaces can be produced by evaporating crystalline films of CaF_2, MgF_2, Chiolit, etc., on the substrate as underlayers before the metal is deposited on it. This procedure, used in general as a qualitative roughening procedure, allows also a reproducible enhancement of the roughness of the metal films to be obtained. One obtains, for silver films, 500 Å thick, evaporated on CaF_2 layers, a linear relation of the r.m.s. height δ with the thickness d of the CaF_2 film. Instead of a CaF_2 underlayer, silver-island films have been used to roughen the silver film vaporized on them [3.8]. For more details see Sect. 4.2.

4.1 The Change of the Properties of the Surface Plasmons Due to Roughness

If the ATR minima of silver films are observed for different roughnesses produced by different thickness d of the CaF_2 film, the curves of Fig. 4.1 are obtained. It displays: at a given wavelength the resonance angle (ATR minimum) displaces to larger wave vectors and the width of the minimum increases strongly [4.1,2]. This effect is already measurable at $d(CaF_2)$ of 250 Å or $\delta \approx 10$ Å (total roughness) as Fig. 4.2 shows. Here the dependence $\omega(k_x)$ is replaced by the plot: λ (wavelength) against $\theta_0(k_x = \sqrt{\varepsilon}(\omega/c)\sin\theta_0)$ with λ decreasing from below to above. This $\lambda(\theta_0)$ representation allows small changes of the dispersion relation to be displayed much better. The values between $d(CaF_2)=0$ and 100 Å are within the error of measurements. Figure 4.2 demonstrates that the phase velocity ω/k_x of the SPs is reduced with increasing δ. The data are independent of whether they are derived from reflecting or scattering experiments [4.3]. The evaluation of the experiments yields Fig. 4.3a,b showing the rapid increase of $\Delta\theta_0$ and $\Delta\theta_0^{1/2}$ with δ; it demonstrates further

◄ **Fig. 4.1**

◄ **Fig. 4.2**
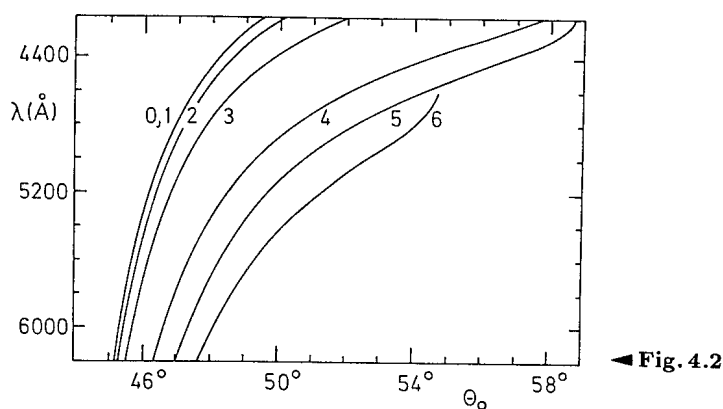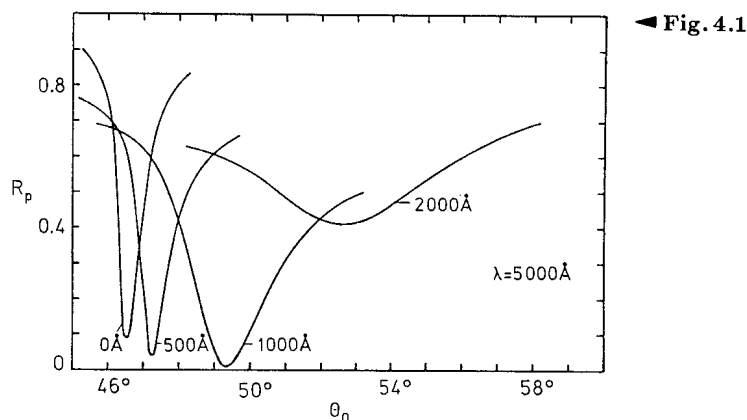
Fig. 4.1. Relative reflected light intensity R_p dependent on the angle of incidence θ_0 ($\lambda =$ 5000 Å) at silver films 540 Å thick, roughened by underlayers of CaF_2 of 0, 500, 1000, and 2000 Å thickness. The strong effect of roughness on the displacement of the ATR minimum and its width is obvious [4.1]. The reflection minimum reaches its lowest value at 1000 Å CaF_2; here the matching condition: internal damping equal to radiation damping is satisfied. The experimental device is shown in Fig. 3.1

Fig. 4.2. Displacement of the angular position of the reflection minimum at different wavelengths λ. The numbers on the curves represent different thicknesses of the underlying CaF_2 film: *0:* 0 Å; *1:* 100 Å; *2:* 250 Å; *3:* 500 Å; *4:* 1000 Å; *5:* 1500 Å; *6:* 2000 Å [4.3]. The curves *5* and *6* show a "backbending" at larger θ_0 which is produced by the strong damping of the mode, see [4.5–7]

the influence of the wavelength, especially the stronger effects at shorter wavelengths.

Similar results have been observed at gold surfaces; here, larger effects are observed [4.4].

Table 4.1 shows the observed numerical values of $\Delta\theta_0$ and $\Delta\theta_0^{1/2}$ for the different wavelengths and, in addition, the calculated values using the second-order approximation, see below. The latter are about a factor 10 smaller than the observed data.
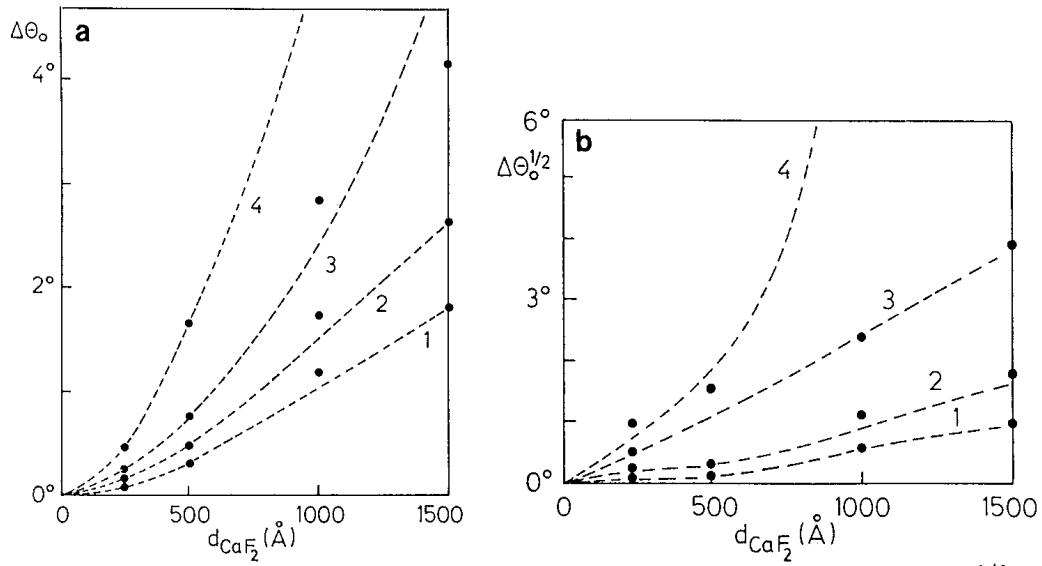
Fig. 4.3a,b. The angular displacement $\Delta\theta_0$ (a) and the increase of the half width $(\Delta\theta_0^{1/2})$ (b) of the reflection minimum at silver films (540 Å thick) at different wavelengths (λ) as function of the roughness. *(1)* $\lambda = 6200$ Å; *(2)* $\lambda = 5600$ Å; *(3)* $\lambda = 5000$ Å; *(4)* $\lambda = 4400$ Å. The roughness is given by the thickness of the underlying CaF_2 films, see Fig. 4.2. The observed values at $d > 1500$ Å CaF_2 and larger than $\Delta\theta_0^{1/2} = 6°$ and $\delta\theta_0 > 5°$ have been suppressed. From [4.3]

Table 4.1a. $\Delta\theta_0$ values (in degrees) of a Ag film of thickness 540 Å at different roughness and light wavelengths λ [3.12]

λ [Å]		$d\,(CaF_2)$ [Å]				
		0	250	500	1000	1500
4400	Obs.	0	0.5	1.8	5	8
	Calc.			0.05	0.1	0.2
5000	Obs.	0	0.25	0.8	2.5	4
	Calc.$\sigma = 1000$ Å			0.065	0.15	0.26
	$\sigma = 500$ Å			0.17	0.4	0.7
5600	Obs.	0		0.5	1.5	2.5
	Calc.			0.07	0.16	0.28
6200	Obs.	0		0.4	1	1.8
	Calc.			0.07	0.17	0.3

Table 4.1b. $\Delta\theta_0^{1/2}$ values (in degrees) of Ag film (540 Å thick) at different roughness and wavelengths

λ [Å]		$d(CaF_2)$ [Å]				
		0	250	500	1000	1500
4400	Obs.	0	1	2	8	–
5000	Obs.	0	0.5	0.9	2.3	4
5600	Obs.	0	–	0.3	1	1.5–2
6200	Obs.	0	–	<0.2	0.6	1
	Calc.	–	–	1.2×10^{-2}	2.7×10^{-2}	4.8×10^{-2}

In Fig. 4.4 a comparison is made between the dependence of $\Delta\theta_0$ on a rough silver surface as a function of δ ($\lambda = 5600\,\text{Å}$) and the same dependence on a grating with a grating constant $a = 4400\,\text{Å}$ ($\lambda = 5000\,\text{Å}$) as a function of the grating amplitude h. The choice of the grating to be compared with the rough surface is somewhat arbitrary; we choose a grating of $a = 4400\,\text{Å}$ which shows a relatively strong dependence of $\Delta\theta_0$ on the value of h, at $\lambda = 5000\,\text{Å}$. The comparison demonstrates that a sinusoidal profile has a much weaker influence on the dispersion relation than a rough surface. This is understandable, but it is surprising that the difference is so strong.
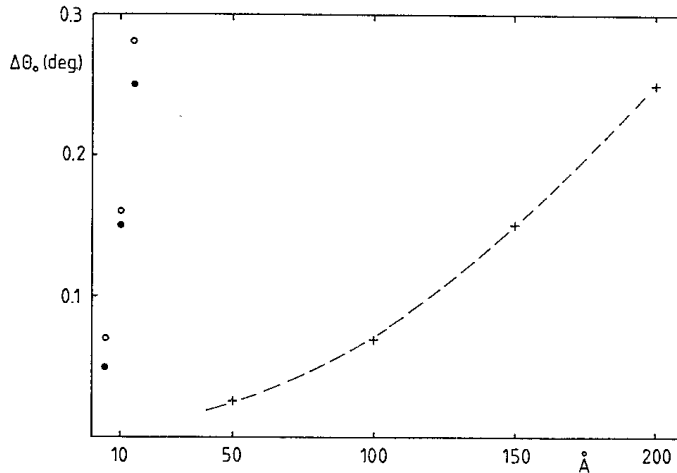

Fig. 4.4. Comparison of the observed displacement $\Delta\theta_0$ (in degrees) on a sinusoidal grating ($a = 4400\,\text{Å}$) and on a rough surface of a silver film, $540\,\text{Å}$ thick, as a function of the grating amplitude h (+) resp. of the roughness height δ(•). The data (•) have to be multiplied by the factor 10(!). For the calculated (o) and the grating data (+) the given scale is valid

4.2 Determination of the Enhanced Roughness

To get the correlation of the r.m.s. height δ with the thickness $d(\text{CaF}_2)$, the angular distribution of the scattered light $(1/I_0)dI/d\Omega$ has been measured at silver films deposited on CaF_2 layers of varying thickness. Figure 4.5 shows an example of this distribution at a silver film deposited on a $1000\,\text{Å}$ CaF_2 underlayer. Characteristic is the pronounced backward lobe compared to the forward lobe; the latter is reduced by the $1000\,\text{Å}$ CaF_2 underlayer which diminishes the effect of the waviness of the substrate [3.8]. The wavelength dependence is relatively small.

If we had at our disposal a light scattering theory of higher order, the evaluation to get δ should be possible. The linear approximation (3.1) loses its validity with larger roughness. Therefore an empirical way has been applied to get the δ values. As described in Sect. 2.5 the fitting of the ATR minima with Fresnel's equation is used to derive the values of $\varepsilon(\omega)$. As long as the thickness of the CaF_2 film is small, less than about $200\,\text{Å}$, the values of $\varepsilon(\omega)$
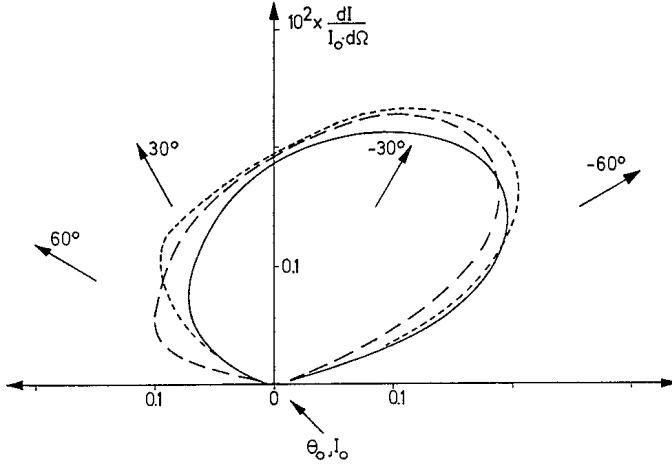
Fig. 4.5. Scattered p-polarized intensity per solid angle element $d\Omega$ and per incident intensity I_0 versus angle of observation θ in polar coordinates for different wavelengths: (———) $\lambda = 5500\,\text{Å}$; (———) $\lambda = 5000\,\text{Å}$; (---) $\lambda = 4500\,\text{Å}$, $d\,(\text{CaF}_2) = 1000\,\text{Å}$; $d\,(\text{Ag}) = 500\,\text{Å}$. In contrast to Fig. 3.5 the light I_0 comes from the right. From [4.3]

obtained with this procedure do not differ from those in the literature. With larger thickness of the CaF_2 film the data deviate more and more at constant frequency ω as Fig. 4.6 shows. The values of $\text{Im}\{\varepsilon\}$ show fluctuations between $d(\text{CaF}_2)=0$ and $500\,\text{Å}$ which have been smoothened.

These "effective" $\varepsilon(\omega)$ are now introduced into (3.1), a procedure which represents a correction of the linear approximation of (3.1). Thus all terms in (3.1) are known in order to calculate $|s(\Delta k_x)|^2$. Assuming a Gaussian correlation function the roughness parameters are obtained for Δk_x of $1-6 \times 10^{-3}\,\text{Å}^{-1}$. With these δ values a linear relation of δ and $d(\text{CaF}_2)$ results, see Fig. 4.7 [3.7], curve (a). Curve (b) of Fig. 4.7 presents interferometric data [4.8] obtained with the FECO method, see [4.9]. Curve (a) gives the values of δ so that $d(\text{CaF}_2)=0$ means the "natural" roughness of the silver surface whereas curve (b) means the increase of δ due to an increase of $d(\text{CaF}_2)$; the starting values of δ_0 are not reported in [4.8]. If we assume $\delta_0 = 5\,\text{Å}$, both plots agree. This relation is nearly independent of the wavelength as the observations at $4500\,\text{Å}$, $5000\,\text{Å}$ and $5500\,\text{Å}$ show. These values are reproducible within about $25\,\%$.

4.3 Discussion of the Theoretical Situation

Whereas the radiation due to photon-SP coupling results from the first-order approximation (3.1), the displacement $\Delta\theta_0$ does not come out, it needs a higher order approximation of the dispersion relation, as has been shown with different methods by *Kröger* and *Kretschmann* [4.10] and *Maradudin* and *Zierau* [4.11]. The solution of this dispersion relation is given by $k_x^0 + \Delta k_x$ with complex Δk_x which is proportional to the r.m.s. height δ^2
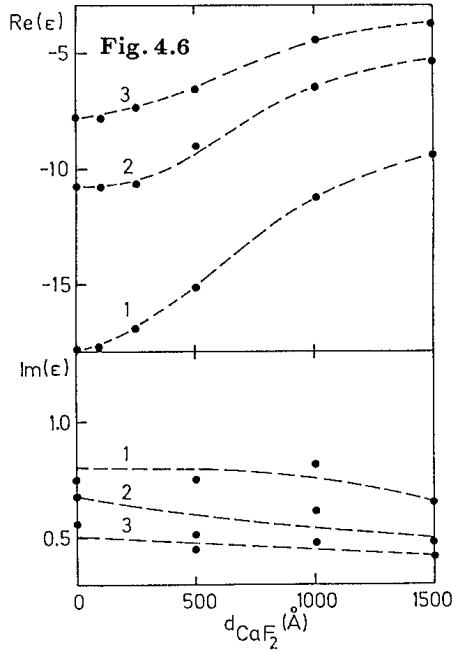
Fig. 4.6. The "effective" dielectric function dependent on $d\,(\mathrm{CaF}_2)$ at different wavelengths: *(1)* $\lambda = 6471$ Å, *(2)* $\lambda = 5309$ Å, *(3)* $\lambda = 4762$ Å. From [4.3]

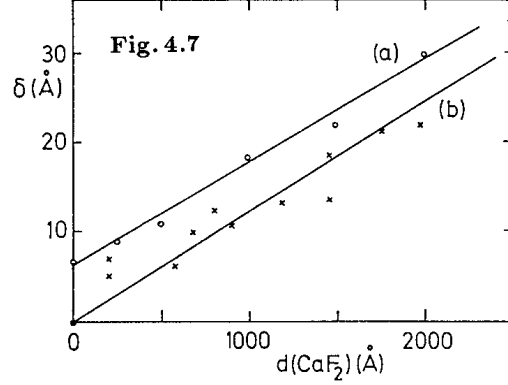**Fig. 4.7.** Relation between the r.m.s. height δ and the thickness of the underlayed CaF_2 film for silver films of 500 Å thickness. *(a)* results from light emission; *(b)* increase of the roughness by underlayers of CaF_2 (FECO − Figures of Equal Chromatic Order − method). From [2.19]

$$\tilde{A} = \left(\frac{\omega_0}{c}\right)^3 \int d^2k \cdot g(\mathbf{k} - \mathbf{k}^0) \cdot A(\mathbf{k}, \mathbf{k}^0)$$

$$\tilde{B} = \left(\frac{\omega_0}{c}\right)^3 \int_0^{2\pi} d\mathbf{k} \cdot g(\mathbf{k} - \mathbf{k}^0) \cdot B(\mathbf{k}^0, \phi) \qquad \text{with} \tag{4.1}$$

$$\Delta \tilde{k}_x = \delta^2 (\tilde{A} + i\tilde{B}) \ . \tag{4.2}$$

The real part of $\Delta \tilde{k}_x$ produces the displacement $(\Delta\theta_0)$ whereas the imaginary part of $\Delta \tilde{k}_x$ is responsible for the damping: $(\Delta\theta_0^{1/2})$. The product $\delta^2 g(\mathbf{k} - \mathbf{k}^0)$ means $|s|^2$. More details and the relations for $\tilde{A}$ and $\tilde{B}$ can be found in [4.10–12]. Here ω_0 is taken as constant. In the case where k_x is taken as constant, the frequency changes as

$$\Delta \tilde{\omega}_0 = -v_{\mathrm{g}} \Delta \tilde{k}_x \tag{4.3}$$

with v_{g} the group velocity of the unperturbed SPs.

The dispersion relation in this approximation which gives the above solutions of $\Delta \tilde{k}_x$, has the form [4.12,13]

$$D_r = \varepsilon D_0 - \delta^2 \left(\frac{\omega}{c}\right)^2 (\varepsilon - 1)^2 \left(\frac{\omega}{c}\right)^2 \int d^2 k'_x g\left(\frac{\omega}{c}|k_x - k'_x|\right) H(k'_x) \quad (4.4)$$

with D_0 the dispersion relation for smooth surfaces (2.2), $\varepsilon_0 = 1$ and $\varepsilon_1 = \varepsilon$ (metal) and

$$H(k'_x) = \frac{1}{D_0 \varepsilon}[\boldsymbol{k}_x \cdot \boldsymbol{k}'_x - k_{z0} k_{z1}(k'_x)]\cdot[\boldsymbol{k}_x \cdot \boldsymbol{k}'_x - k_{z0}(k'_x) k_{z1}] . \quad (4.5)$$

In this relation the k values are given in units of ω/c.

Physically, the lower phase velocity of the SPs on rough surfaces is a consequence of multiple scattering; in the simplest case

(1) $\boldsymbol{k}_x^0 \rightarrow \boldsymbol{k}_x^0 + \Delta \boldsymbol{k}_x = \boldsymbol{k}'_x$

(2) $\boldsymbol{k}'_x \rightarrow \boldsymbol{k}'_x - \Delta \boldsymbol{k}_x = \boldsymbol{k}_x^0$. $\quad (4.6)$

It means: (1) scattering in a new direction, followed by a rescattering (2) into the original direction. Thus a field in the original direction, built up by the scattered waves propagates with a reduced phase velocity whereas the original field is quickly extinguished (Ewald-Oseen extinction theorem).

If (4.2) is applied to rough surfaces assuming a Gaussian function for $|s|^2$ [4.14], data for $\Delta\theta_0$ and $\Delta\theta_0^{1/2}$ are obtained which are much smaller than the observed [3.12], see Table 3.1. The effect of sinusoidal profile on the properties of the SPs, however, is rather well described with a second-order approximation, see Chap. 6. Apparently, multiple scattering on rough surfaces comes already into play at rather low δ which cannot be calculated as yet.

Recently, however, a theoretical treatment has been published that includes all higher orders [4.15]. Applications to experimental results do not yet exist.

A suggestion to understand the strong effect of the roughness can be the following: Discussing the influence of the roughness, we had assumed $\delta/\sigma \ll 1$ to get the first approximation; this condition is valid for the average profile. But Fig. 3.15 demonstrates that the structure at an atomic scale reveals some regions of the profile which have steeper slopes h/a than about 0.4 ($h \sim 5$ Å, $a \sim 20$ Å). Since the number of such regions is probably relatively small on the rather smooth surfaces of $\delta \sim 5$ Å, their influence is weak. But if their number increases rapidly with increasing roughness, they can have a strong effect. It is therefore understandable that, e.g., the second-order approximation fails.

Concerning Fresnel's equations, we have seen that the small roughness assumed in the first-order approximation produces negligible power loss by the diffuse light emission and leaves Fresnel's equations unchanged. Second-order approximation, however, leads to changes as calculations for normal incidence have shown [4.16]. These relations have been extended to oblique incidence in order to evaluate the roughness of evaporated Al films, irradiated with electrons of 15 KeV (~ 0.2 W/cm^2) [2.16]. A higher order approximation, however, is lacking for a quantitative evaluation.

4.4 The Attenuated Total Reflection Minimum as a Function of Damping

Figure 4.1 displays the influence of the increasing roughness on the ATR minima or the SP modes. In addition, it shows that the height of the reflection minimum passes a value of nearly $R_{\min} = 0$. This happens at $d(\text{CaF}_2)$ about $1000\,\text{Å}$ or a roughness height (total) of about $15\,\text{Å}$. This resembles the situation at smooth surfaces if one chooses the thickness d of the metal film, so that (2.24) is fulfilled. Here, in the case of rough surfaces, one has to introduce into (2.24), in addition to the radiation damping term Γ_{rad}, a further term Γ_{rad}^* which describes the damping by light emission into the air space; it increases approximately with δ^2 and contributes to the displacement of θ_0. At

$$\Gamma_{\text{i}} = \Gamma_{\text{rad}} + \Gamma_{\text{rad}}^* \qquad (4.7)$$

the matching condition is fulfilled and the maximum field enhancement is expected. In silver film thicker than about $1000\,\text{Å}$, Γ_{rad} can be neglected and Γ_{rad}^* is determinative.

The same behavior as shown in Fig. 4.1 has been observed at the reflection minima on gratings: if, e.g., the amplitude of the sinusoidal profile is increased, the height of the reflection minimum goes through zero, see Chap. 6.

In order to understand the curves of Fig. 4.1, at least qualitatively, we calculate L_{i} and L_{rad} for different roughnesses. In Sect. 2.9 the values of $L_{\text{i}} = 22\mu$ and $L_{\text{rad}} = 1400\mu$ have been obtained for $\delta = 5\,\text{Å}$ and $\sigma = 1500\,\text{Å}$; this means that $\Gamma_{\text{i}} > \Gamma_{\text{rad}}$ for the curve $d(\text{CaF}_2) = 0$ in Fig. 4.1. Roughening the surface increases Γ_{rad}^*, so that the minimum gets deeper. At $d(\text{CaF}_2) \approx 1000\,\text{Å}$ or $\delta \approx 15\,\text{Å}$ (total roughness) one expects $L_{\text{i}} \approx L_{\text{rad}}$. Applying (2.57) we obtain a value of $\delta \approx 40\,\text{Å}$. ($\sigma = 1500\,\text{Å}$), which is somewhat larger than $15\,\text{Å}$. Here one needs more experimental material.

4.5 Enhancement and Roughness; Second Harmonic Generation (SHG)

The field enhancement $|t_{012}^p|^2$, (2.25), has been applied to describe the strong light emission from rough surfaces in the linear approximation, see (3.1). In this approximation one assumes that the average field in the surface is enhanced by the same factor $|t_{012}^p|^2$ as on a smooth surface.

For larger roughness, $\delta > \sim 20\,\text{Å}$, the light scattering experiments could be evaluated approximately: they showed that the ε' values have to be reduced for larger roughness. It follows, using (3.1), that the enhancement factor (2.27), decreases with larger δ values. For example, with $\lambda = 6000\,\text{Å}$ and silver the term $|t^p|^2$ decreases from 80 to ≈ 50 at $\delta \approx 15\,\text{Å}$. See also Fig. 16, Chap. 9 in [2.4]. This result can be formulated thus: that the quotient P_{sc}/δ^2 decreases with larger δ, here $P_{\text{sc}} = (1/I_0)dI/d\Omega$. It would be interesting to verify this experimentally and theoretically.

It is remarkable that the same behavior has been found on gratings: the diffracted intensity enhanced by SP excitation divided by the grating amplitude T/h^2 decreases with h for $\lambda \gtrsim 70$ Å, see Chap. 6.

In this context we shall discuss a proposal to determine the roughness by measuring the intensity of the 2ω light [4.17]. If an intense light beam of frequency $\omega < \omega_s$ hits a rough surface at an angle θ_0 the photon can take up Δk_x from the roughness spectrum, so that $k_x = \Delta k_x + (\omega/c)\sin\theta_0 = (\omega/c)\sqrt{\varepsilon/(\varepsilon + 1)}$ is fulfilled (grating coupler). A strong electric field is built up in which a second incoming photon of frequency ω produces via the quadratic term of the susceptibility light of frequency 2ω; its intensity is proportional to $|D_0(\omega)|^{-2}$ (for D_0 see (2.2), [4.17]). This process corresponds to the SHG in the ATR device, see Fig. 2.30. The calculated intensity of the 2ω radiation based on a linear approximation $(2\pi/\lambda)\delta \ll 1$ shows a strongly peaked 2ω intensity at certain angles on a 2ω broad-band background. The roughness parameters were chosen in [4.17] as $\delta = 100$ Å and $\sigma = 500$ Å; but the results remain valid if one reduces δ to 10 Å, so that the region of the linear approximation is reached and the assumption that the dispersion relation is not changed by the roughness, is fulfilled. The intensity is thus reduced by a factor of 100, but it should be high enough to be measurable. Experiments with extended SPs on rough surfaces to detect this angular distribution of the 2ω intensity have not yet been published.

## Large Roughness and SHG Generation. Localized Plasmons. SERS.

Up to now there exist no ATR experiments at larger roughness of more than 20–30 Å.

Without ATR a number of interesting results on rougher surfaces have been found which will be discussed in Chap. 5.

Here we present results obtained for very rough surfaces consisting of particles of about 500 Å radius. They are treated here, since the central concept is the localized collective oscillation of electrons or localized plasmons in contrast to the extended or propagating modes. Such localized modes are well known e.g., as the eigen modes of small spheres.

In the following, a series of such experiments is described and explained.

Experiments on silver surfaces, roughened in an electrolyte ($H_2O + KCl$) by a reduction-oxidation cycle are desribed by *Chen* et al. [4.18]. By the way: With such a device *Fleischmann* et al. have discovered the SERS. Electron micrographs indicate that the roughness consists of particles of about 500 Å diameter separated from each other by a distance of 1500 Å–3000 Å. In these experiments a laser beam ($\lambda = 1.06\mu$) is directed towards the rough surface at an angle of 45°. The scattered light is diffuse and nearly isotropic in the angular distribution. Its spectral distribution, displayed in Fig. 4.8, shows a strong peak at 2ω on a broad-band background. In contrast, the signal from a smooth silver foil is well collimated in the specularly reflected beam. The total 2ω intensity emitted from the rough surface into the air space is about 10^4 times stronger than the 2ω intensity in the beam specularly reflected at the smooth surface. In gold this enhancement is about 10 times weaker. The authors estimate that
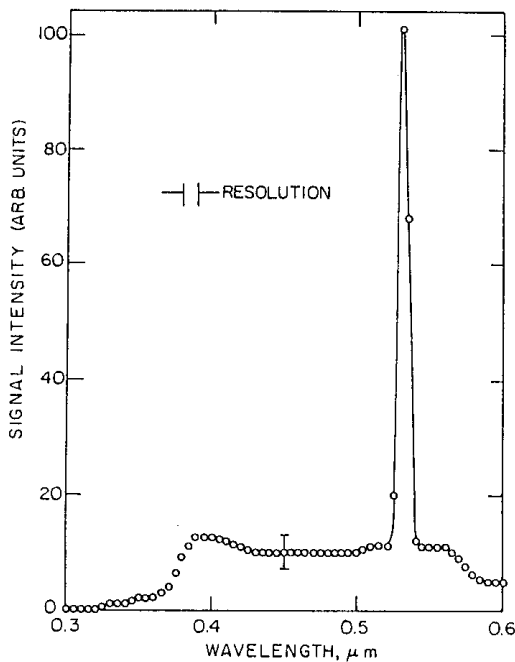
Fig. 4.8. The spectrum of the light signal reflected at a very rough silver film. The incoming light frequency amounts to $1.06\,\mu$; the spectral distribution shows a strong signal at the double frequency. From [4.18]

— depending on the intensity — the local field in silver is enhanced by about a factor of 20 to 400.

Further experiments have been published on very rough surfaces by *Boyd* et al. [4.19], which were produced by vaporizing different metals on a strongly etched glass substrate. The surface consists in this case of protrusions of different thickness $(100-1000\,\text{Å})$, varying heights and distances; the tips are regarded as hemispheroids and have thus varying eigen modes depending on a/b, see Sect. 2.10.

If this roughness structure is irradiated with monochromatic light, here 1.06μ, the tips with a suitable geometry a/b are excited in resonance and emit a certain amount of 2ω light intensity. This SH intensity is compared with that produced on a smooth silver surface.

The quotient of both intensities has been measured for a large number of metals and germanium. The observed data are plotted against calculated quotients using the assumptions just mentioned and averaging over the surface; they lie better than an order of magnitude on a straight line with a 45° slope. This supports the interpretation of the observed SHG light as due to the high local electromagnetic fields in the resonance case.

The theoretical dependence of the SERS intensity on the field enhancement is essentially the same as the dependence of the SH generation on the field enhancement. It has been confirmed by experiment, see [4.19], and implies that under these conditions the SERS is mainly an electromagnetic effect (the chemical interaction between the absorbed molecule and the metal plays no important role).

These examples and a number of similar experiments lead to the result that the strong enhancement of SERS of about 5×10^4 can be obtained on

surfaces which are composed of more or less isolated silver particles of about 500 Å radius separated by distances of about 1500–3000 Å. Samples with larger particles, e.g., 2000 Å radius which are in contact with each other give Raman signals about 10 × times smaller [4.32].

This interpretation of SERS as collective electron resonances in small particles has been proposed by *Moskowitz* who stated that "this behavior may be explained by taking the effect to originate in adsorbate covered metal bumps on the metal surface" [4.33].

Surfaces, which have a roughness of 150 Å height under the Scanning Electron Microscope, show no enhancement. In this context "no enhancement" means a value below about 100 for one monolayer of pyridine on silver. However, this does not say that the "conventional surface plasmon model" has to be modified [4.32]. As we mentioned earlier, an enhancement of about 100 is expected at a roughness of $\delta<20$–30 Å and has also been measured in the experiments of *Girlando* et al., see [4.34], so that more sensitive methods would have detected a Raman signal in the experiment of [4.32].

It is remarkable that the strong enhancement is not limited to the first layer of adsorbed molecules which is in contact with silver. The enhancement of certain Raman lines of pyridine on silver in SERS experiments at $\lambda = 4880$ Å increases with coverages up to seven monolayers which corresponds to a distance of about 50 Å, by a factor 3 [4.32].

An interesting step towards better defined experimental conditions concerning the roughness structure has been realized by constructing a controlled roughness structure, see *Liao* et al. [4.20]. This progress is realized by producing with microlithographic techniques a regular array of posts with nearly hemispheroid-like tips, see Fig. 4.9, so that the wide variety of shapes and sizes is very much reduced. The posts, about 5000 Å high, less than about 1000 Å in diameter and at a distance of about 3000 Å apart, consist of SiO_2 standing on a Si surface. Then silver is vaporized on them at grazing incidence, so that the tips are mainly covered with the metal and thus are more or less isolated from each other. Irradiating this array with laser light, the eigen modes of these metal tips are excited in resonance and thus produce strong fields. To a first approximation the modes vibrate independently: "localized" plasmons.
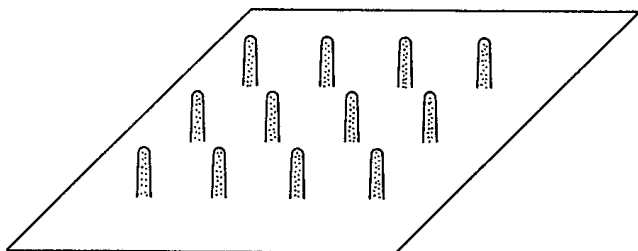

Fig. 4.9. On the tips of the SiO_2 posts of this regular array which have the shape of a hemiellipsoid a silver film is deposited. Their eigen frequency is given by the quotient b/a of the tip. Irradiation of this array with light of variable frequency shows a resonance in the SERS intensity as Fig. 4.10 displays

68

This idealized structure allows one to calculate the expected enhancement values taking the a/b ratios of the ellipsoidal shape of the tips from electron micrographs [4.21].

As a detector of the field enhancement, the intensity of the surface enhanced Raman scattering (SERS) of CN molecules adsorbed at the silver surface has been used, which increases by many orders of magnitude if high-electric fields act on the adsorbed molecules.

The advantage of this controlled roughness structure with a rather well-known value of its eigen mode becomes evident, if one measures the SERS intensity as a function of the incoming wave light: it displays a pronounced resonance character as demonstrated in Fig. 40 of [4.22].

In Fig. 4.10 the full line (silver curve) is obtained by fitting the measured data with A and V as adjustable parameters, see (2.69); $A = 0.08$ and $V = 3.1 \times 10^{16}$ cm^3 give the best fit. With the same parameters the curve observed at gold (dashed line) is calculated which agrees surprisingly well with the observed data. This supports the assumptions. The calculated averaged enhancement is about 5×10^4 whereas the observed value is $100 \times$ larger, a point still under discussion.

Here a number of questions arises: e.g., what happens if the tips are rather close together so that they are not isolated but coupled with each other. Another coupling is possible if an array of tips is covered with a continuous film. Here a continuous transition into the extended SP is expected.
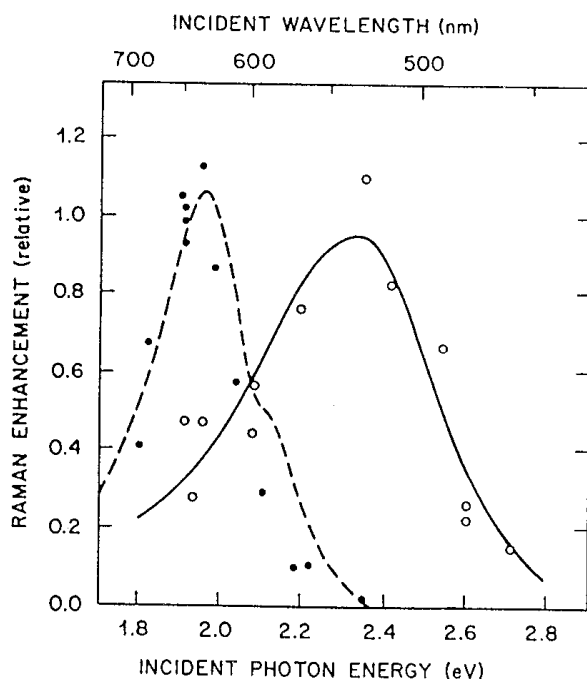
Fig. 4.10. Resonance-like dependence of the Raman signal as a function of the photon energy measured at an array of tips covered with two different metals. Gold: ●●●, Silver: ooo. From [4.22]

4.6 Efficiency of the Plasmon-Photon Coupling

For certain purposes it is of interest to know at least approximately the number of photons emitted per second from the decay of SPs into the whole air-side space (2π) divided by the absorbed light power or the "efficiency" of this process. In the matching case $(R = 0)$ the incoming light power I_0 is completely absorbed; if this condition is not fulfilled, $I_0(1-R)$ is the absorbed power. For a smooth surface this efficiency is zero. A silver surface with δ of a few angstroms has an efficiency of $\approx 1\%$ which can be derived from the values of $(1/I_0)dI/d\Omega$ as a function of θ, the angle of emission against the surface normal. This agrees with observations using the photoacoustic detector [2.14] which show that the efficiency of a similar silver film has a value of 2%, the lowest limit of detection. On similar films [4.23] the whole light emission, $\int(1/I_0)(dI/d\Omega)d\Omega$, and the absorbed power, $I_0(1-R)$, were measured and gave an efficiecy of $\approx 5\%$ at silver films of $500\,\text{Å}$. These data agree roughly considering the different conditions of preparation.

If the roughness is increased by underlying CaF_2 films, the efficiency increases as is expected. Values up to 9% are published for $d(CaF_2) > 1000\,\text{Å}$ [4.23]. One obtaines similar values by integration over $d\Omega$ for $d(CaF_2) = 1000\,\text{Å}$ as after actual observation. Larger figures have been found using the photoacoustic method [4.24] at $d(CaF_2) = 0\,\text{Å}$: the efficiency is measured as $\approx 15\%$ which increases up to $\approx 35\%$ at $d(CaF_2) = 800\,\text{Å}$. The reason for the discrepancy between the efficiencies of the rougher surfaces from those measured with a light detector is unknown.

4.7 Light Emission from Inelastic Electron Tunneling in MOM and MIS Junctions

Another experiment demonstrates the SP-photon coupling in a tunnel junction [4.25]. A voltage V_1 is applied to a metal/metal oxide/metal system, e.g., Al/Al-oxide (about $30\,\text{Å}$ thick)/Ag (silver is vaporized onto the Al-oxide), so that a tunnel current crosses the oxide barrier. If the surface of the silver film, thickness about $100\,\text{Å}$, is roughened by mild etching or by CaF_2 underlayers, the SPs produced by the tunneling electrons, couple via roughness with light.

The spectrum of this radiation shows a broad band; its upper limit is given by the quantum relation $\hbar\omega = e|V_1|$. Light emission between $2000\,\text{Å}$ $(6\,\text{eV})$ and $10\,000\,\text{Å}$ $(1.2\,\text{eV})$ can easily be observed. This effect is independent of the polarity of the applied voltage. The efficiency of this light source is, at best, 10^{-4}, which is rather low.

For applications, e.g., as a light source which can be modulated, one needs a higher efficiency. A possibility is to improve the coupling electron-photon by a special microstructure of the counter-electrode.

An interesting version is displayed in Fig. 4.11: there the rough surface is replaced by an (unroughened) gold counter-electrode ($80\,\text{Å}$ thick). This sys-
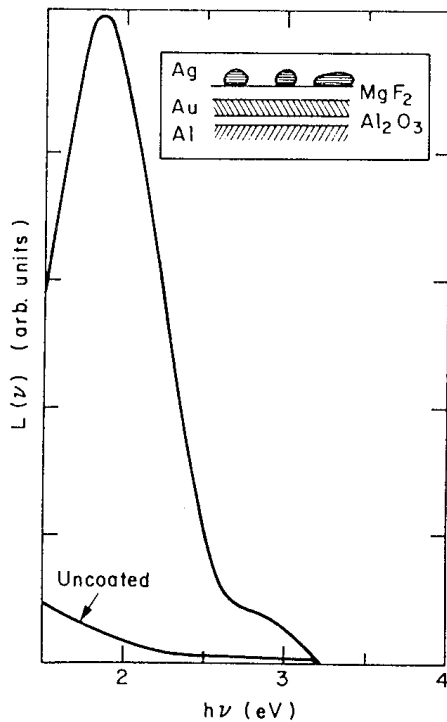
Fig. 4.11. The emission spectrum (photon flux) of the junction: Ag+MgF$_2$+Au/Al-oxide/Al at a voltage of V_1 = 3.22 eV without the MgF$_2$+Ag structure (uncoated) and with it, see insert. From [4.25]

tem and its emission spectrum is called an "uncoated" junction; it extends up to 3.22 eV given by the applied voltage. The gold electrode is then covered with a 50 Å MgF$_2$ film and there upon a silver film of about 100 Å thickness is deposited. Heat treatment transforms the silver film into an assembly of silver particles of about 100 Å diameter, so that the configuration in Fig. 4.11 is produced. The emitted spectrum changes drastically into a peaked one. The resonance-like shape indicates the excitation of "localized" modes, see also [4.26]. The MgF$_2$ film serves a spacer, its thickness has a strong influence on the emitted intensity, demonstrating the decay of the coupling field. For theoretical considerations see [4.27].

Experiments with metal/insulator/semiconductor or MIS junctions have been performed, too. As a semiconductor Sn-doped indiumoxide has been used, the efficiency, however, was not improved [4.25].

This device has been modified in so far as the rough profile is replaced by a grating profile which couples with the field of the tunnel electrons as is discussed in more detail in Chap. 6. The tunnel junction, here Al/Al-oxide/Ag, is laid down on the silver grating as shown in Fig. 4.12 [4.28,29]. In this case the light emitted from the junction is concentrated in a few diffraction maxima as displayed in Fig. 4.13. This is similar as demonstrated in Fig. 6.3 where the SPs are excited by an exterior light source and not by slow electrons as in Fig. 4.13 or by fast electrons as in Fig. 6.14. This junction has been explored in more detail in [4.30]. Although the quantum efficiency is still rather low, about 10^{-7} with a bias voltage of 2.3 eV, there is the possibility of increasing the bias voltage by about 1 eV to get a quantum efficiency comparable to those
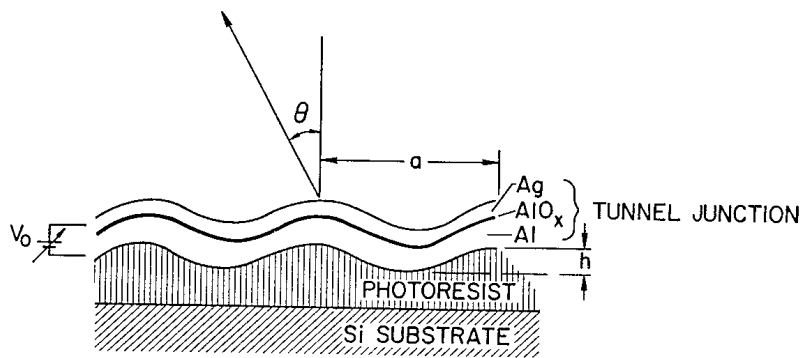
Fig. 4.12. The tunnel junction Al/Al-oxide/Ag is placed on a sinusoidal grating of photoresist, which couples out the nonradiative SP field into light. From [4.28]
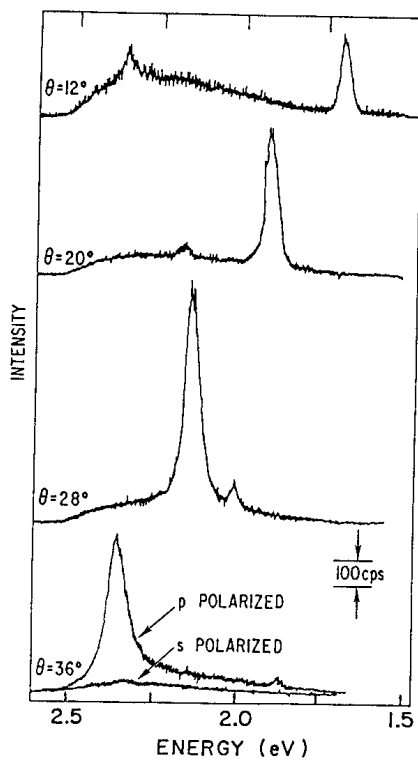

Fig. 4.13. The out-coupled light is emitted into different diffraction directions θ. The wavelength and the take-off angle θ are related by $(2\pi/\lambda)\sin\theta = \nu 2\pi/a + k_{sp}$. The large peak, which moves to higher energies with increasing θ, belongs to $\nu = 1$ whereas the opposite behavior of the small peak is described by $\nu = 2$. $a = 8200$ Å, grating amplitude $h = 50$ Å. From [4.28]

junctions with roughened electrodes. It is a technical problem to fabricate such junctions.

The question is discussed where the coupling of the electrons and SPs happens. The early idea has been that the tunnel electrons suffer in inelastic collision in the barrier and thus produce the SPs in the metal electrodes, e.g., in the silver film.

Another concept proposes that the tunnel electrons penetrate into the metal (silver) as hot electrons, where they relax and excite SPs besides phonons etc. This proposal is discussed in more detail in [4.30]. For theoretical considerations see [4.31].

5. Light Scattering at Rough Surfaces Without an ATR Device

In the following, the results of experiments are described in which light hits the rough surface directly, see Fig. 5.1, and is scattered into all directions θ. In order to derive the roughness parameters of the surface, two methods have been developed:

1) Measurements of the angular distribution of the light scattered into the light cone ($k_x < \omega/c$). The light intensity is measured which is scattered into the solid angle $d\Omega$ out of the specularly reflected beam. It is the well-known diffusion of light produced by the roughness which is represented in Fig. 2.4 by all the scattering processes starting at the point 1 with k_x, the wave vector of the incoming beam, and ending at all points inside the light cone, transferring Δk_x. Surface plasmons become involved if the roughness is increased and thus larger Δk_x become more frequent. This process is demonstrated by 1→4 (grating coupler). The excitation is visible in the angular distribution of the scattered light.

2) Measurements of the deficit of the intensity of the specularly reflected light ΔR due to the loss of light scattered out of the beam and exciting SPs via a grating coupling. This deficit is hardly to be seen at low roughness. To get a pronounced dip ΔR which can be evaluated, a greater roughness is needed, see below.

The first method registers $(1/I_0)dI/d\Omega$, the second integrates over all angles θ so that one loses important details.
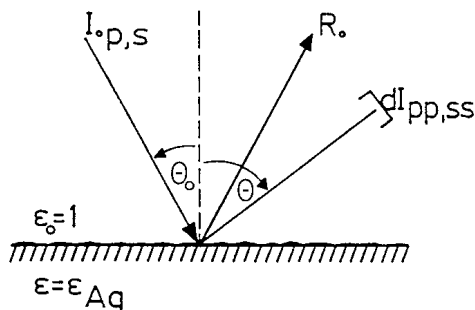
Fig. 5.1. Scheme of the light-scattering experiment at a rough surface. Besides the reflected beam (R_0) diffusely scattered light is observed

73

5.1 The Angular Distribution of Light Scattered at a Rough Surface

The phenomenon of diffusely scattered light at rough surfaces is well known. Since SPs are not involved, i.e., no resonant enhancement interferes, p as well as s polarization has to be looked at. The experimental arrangement is that in Fig. 5.1, the detector, however, does not register R_0 but the light scattered into the solid angle $d\Omega$. It is an angle discriminating procedure.

Theoretical Considerations

This effect has been calculated first for the scattering of radio waves by the waves of the ocean [5.1]. The same relations result when applying different approaches assuming $\delta \ll \lambda$ and $\delta \ll \sigma$ (first-order approximation) [5.2–5]. The relative intensity scattered into the solid angle $d\Omega$, in the plane of incidence $\phi = 0$, comes out as

$$P_{\rm sc}^{ik} = \frac{1}{I_0^{ik}} \frac{dI^{ik}}{d\Omega} = \frac{1}{4}\left(\frac{\omega}{c}\right)^4 \frac{|W_{ik}|^2}{\cos\theta_0} |s(\Delta k_x)|^2 \ . \tag{5.1}$$

It contains no enhancement by SPs; however, it cannot be said generally how strong the numerical intensity reduction comes out without this factor $|t_{012}^p|^2$, since the angular functions $|W_{ik}|^2$ (5.2,3) and $|W(\Theta)|^2$ (3.1) depend on the experimental configuration. Furthermore, one has to consider that $|s(\Delta k_x)|^2$ may be different except Δk_x is identical comparing both configurations. The indices i, k indicate the polarization p or s.

One obtaines for W_{ii} at $\phi = 0°$ with complex $\varepsilon(\omega)$ and assuming surface roughness:

$$W_{pp} = \frac{4(\varepsilon_1 - 1)\cos\theta_0\cos\theta}{(\varepsilon_1\cos\theta_0 + \sqrt{\varepsilon_1 - \sin^2\theta_0})(\varepsilon_1\cos\theta + \sqrt{\varepsilon_1 - \sin^2\theta})}$$
$$\times \ (\varepsilon_1\sin\theta_0\sin\theta - \sqrt{\varepsilon_1 - \sin^2\theta_0}\sqrt{\varepsilon_1 - \sin^2\theta}) \quad \text{and} \tag{5.2}$$

$$W_{ss} = \frac{4(\varepsilon_1 - 1)\cos\theta_0\cos\theta}{(\cos\theta_0 + \sqrt{\varepsilon_1 - \sin^2\theta_0})(\cos\theta + \sqrt{\varepsilon_1 - \sin^2\theta})} \tag{5.3}$$

or, more general, for any ϕ, the angle between the plane of incidence and the plane of observation, instead of $|W_{ik}|^2$

$$|W_{pp}|^2 \cos^2\phi + |W_{ss}|^2 \sin^2\phi \ . \tag{5.1a}$$

Figure 5.2 displays the functions W_{ii}; p-polarized light is stronger than the s-polarized. ($W_{pp} = 0$ gives the Brewster condition), W_{ps} and W_{sp} are zero in the linear approximation (for $\phi = 0$ as is evident looking at the radiating dipoles in Fig. 3.3). The $|W(\theta)|^2$ for $\theta_0 = 0$ is symmetric about $\theta_0 = 0$, while it becomes asymmetric for $\theta_0 > 0$.

74
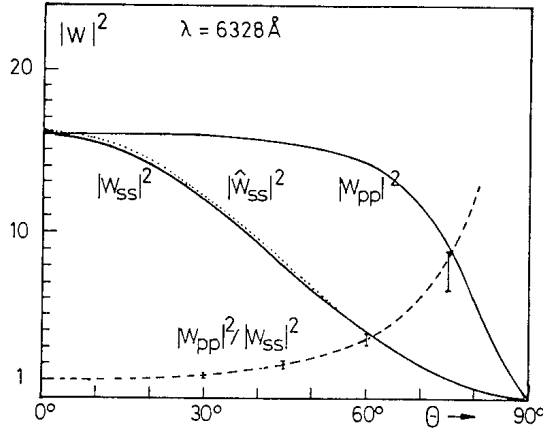
Fig. 5.2. The dipole functions $|W_{ii}(\theta)|^2$ calculated for $\theta_0 = 0$, $\lambda = 6328\,\text{Å}$ and silver. From [5.8]

The denominator of W_{pp} is identical with the dispersion relation (2.2) for SPs; it cannot be fulfilled since the observation takes place inside the light cone, $k_x = (\omega/c)\sin\theta_0 < (\omega/c)$.

The value of W_{ss} can be approximated for $\mathrm{Im}\,\{\varepsilon_1(\omega)\} \ll \mathrm{Re}\,\{\varepsilon_1(\omega)\}$ by

$$\hat{W}_{ss} = 4\cos\theta_0\cos\theta \qquad\qquad (5.4)$$

see Fig. 5.2 which is independent on λ, whereas W_{pp} is weakly dependent on it.

We shall see that second-order processes come into play already at rather small roughness: (a) the appearance of SP and PS intensities and (b) the excitation of SPs via grating coupling with subsequent emission of radiation, see process $1\rightarrow2\rightarrow1$ in Fig. 2.4.

Experimental Results

Experimental data for the angular distribution at normal incidence are shown in Fig. 5.3. The intensity decreases monotonically, whereby the pp intensity lies above the ss intensity. This difference is apparently due to the different angular functions, since $|W_{pp}|^2 > |W_{ss}|^2$ whereas the decrease of the reflectivity is caused by the roughness function.

The comparison of the quotient $I_{pp}/I_{ss} = |W_{pp}|^2/|W_{ss}|^2$ with the calculated quotient as a function of θ shows good agreement and the consistency of the assumptions, see Fig. 5.2.

The roughness function $|s|^2$ can be deduced as described in Chap. 3; it is displayed in Fig. 5.4 for two angles θ_0 and demonstrates that the linear part is better defined for $\theta_0 = 60°$; it gives a value of $\delta = 14\,\text{Å}$ and $\sigma = 1550\,\text{Å}$ [5.7]. A comparison with Fig. 3.8 shows that in the ATR device the $|s|^2$ function can be observed up to larger Δk_x values, so that the longer linear part allows a more precise determination of the roughness parameters. The nonlinear part of the $|s|^2$ function at small k_x values is interpreted as being due to a waviness of the substrate as in the experiments with SPs. Some data δ and σ obtained on films of different thickness d_{Ag} are shown in Table 5.1. It confirms also the
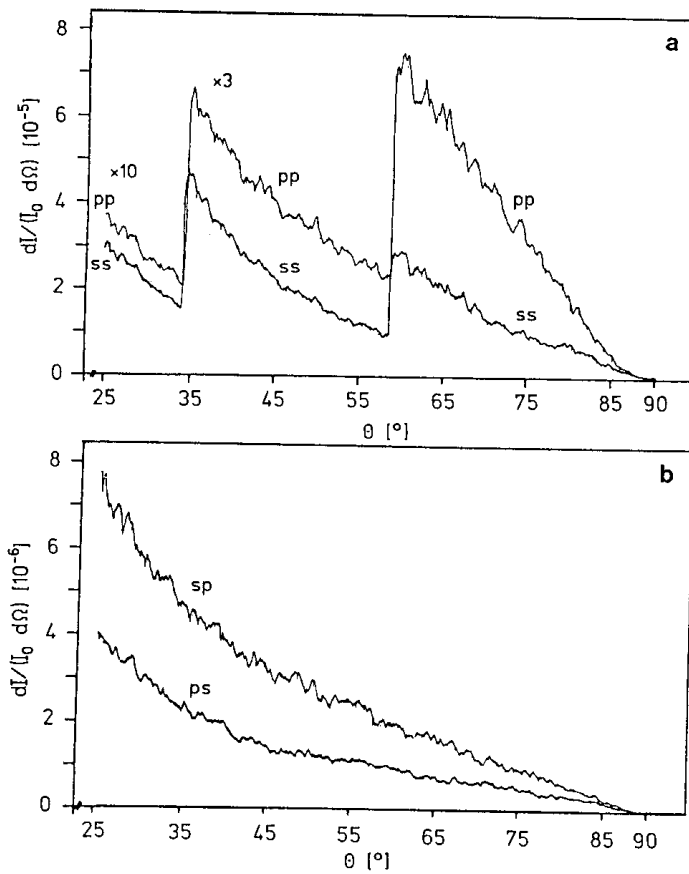
Fig. 5.3. Angular distribution of diffusely scattered light ($\lambda = 5145\,\text{Å}$) at a silver surface of $4000\,\text{Å}$ thickness and $\delta \approx 10\text{--}15\,\text{Å}$ at normal incidence. p and s indicate the different polarizations. The depolarized intensity (sp and ps) is about 10 times smaller. The solid angle of the detector amounts to $d\Omega : 8 \times 10^{-5}$ sr. From [5.6]
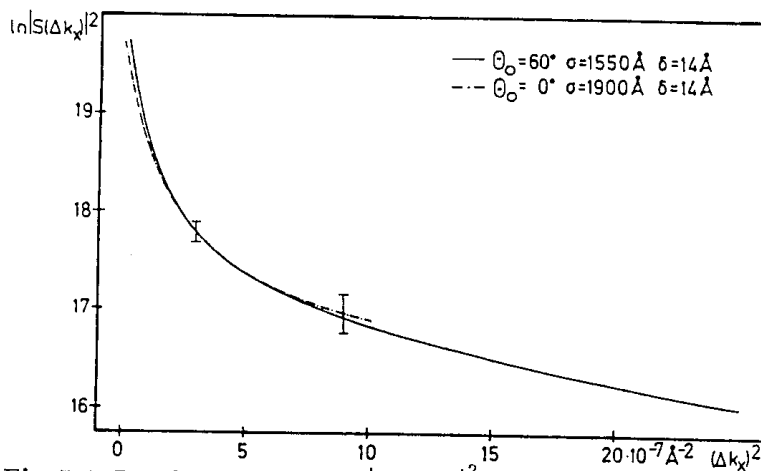

Fig. 5.4. Roughness function $\ln|s(\Delta k_x)|^2$ versus $(\Delta k_x)^2$ of a silver film, $4000\,\text{Å}$ thick. $\theta_0 = 0°$, normal incidence (—•—); $\theta_0 = 60°$ incidence (——); $\lambda = 5000\,\text{Å}$. The evaluation yields $\delta = 14\,\text{Å}$ and $\sigma = 1550\,\text{Å}$. From [5.7]

Table 5.1. Roughness parameters of silver films of different thickness ($\lambda = 6328$ Å) [5.8]

d_{Ag} [Å]	δ [Å]	σ [Å]
500	4	2050
1000	7	1900
4000	9	2300

observation that the roughness increases with the thickness of the films. Further data of roughness of silver films, 4000 Å thick, as a function of the thickness of CaF_2 underlayers can be found in [5.8][1].

The experimental arrangement of Figs. 3.7,1 allows one to compare the determination of $|s(\Delta k_x)|^2$ of the film surface with both methods, with and without SPs by turning the half cylinder by 180°. A good agreement has been stated for film thicknesses of 500–700 Å with $\delta \approx 5$ Å, as Fig. 5.5 displays [5.9]. In addition it demonstrates the independence of δ on λ.

Measurements of the angular distribution of the light intensity on evaporated thick silver and gold films at normal incidence were first published by *Beaglehole* and *Hunderi* [5.10]. They observed an angular distribution of scattered light as Fig. 5.6a shows; δ has not been evaluated. A comparison of the relative reflectivity values, however, demonstrates that these surfaces are rougher than those of Fig. 5.3. Further, there is a difference between the observed (dots) and calculated values (with the first-order approximation, dashed line). The authors show that the full curve can be obtained by regarding a double process: with increasing roughness, the pp scattering excites SPs which are scattered into the light cone and produce an excess of radiation of pp light. This explanation is supported by using photon energies above the surface plasma energy (3.7 eV) so that SP excitation cannot take place, see Fig. 5.6b. This second-order ef-
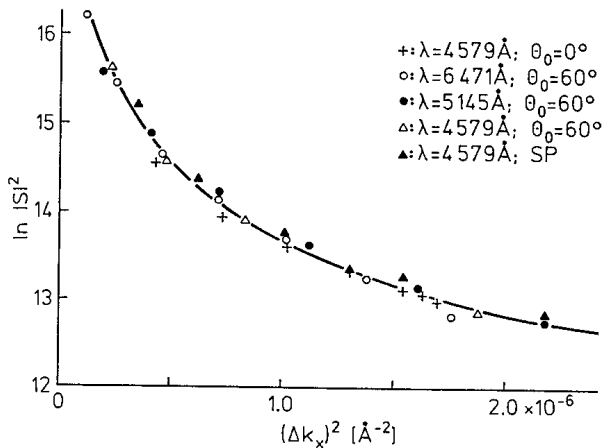
Fig. 5.5. Roughness functions of a silver film, 500 Å thick, obtained at different angles of incidence θ_0 and wavelengths up to $\Delta k_x = 1.5 \times 10^{-3}$ Å^{-1}. For comparison, data obtained on the same sample using the SP resonance are shown. From [5.9]

+: $\lambda = 4579$ Å; $\theta_0 = 0°$
o: $\lambda = 6471$ Å; $\theta_0 = 60°$
•: $\lambda = 5145$ Å; $\theta_0 = 60°$
△: $\lambda = 4579$ Å; $\theta_0 = 60°$
▲: $\lambda = 4579$ Å; SP

[1] The ordinate of Fig. 2 in [5.8] has to be divided by $d\Omega = 1.4 \times 10^{-3}$ sr in order to give the right $(1/I_0)dI/d\Omega$ values.
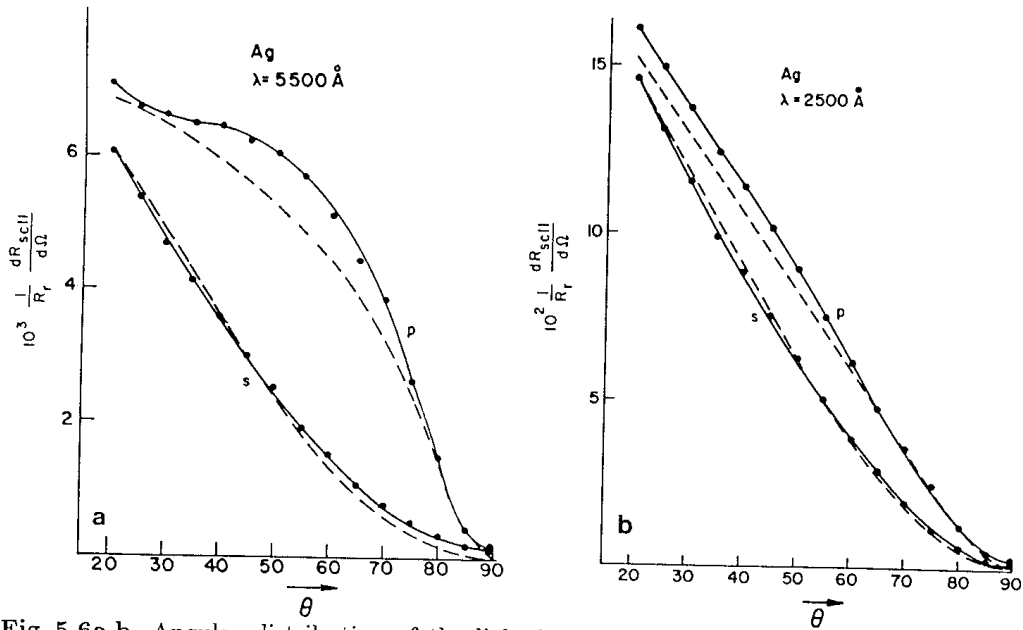
Fig. 5.6a,b. Angular distribution of the light intensity scattered at rough silver surfaces measured below (a) and above $\hbar\omega_{sp}$ (b). The *dashed line* shows the shape of the curves in the linear approximation. From [5.10]

fect is seen to be stronger in Fig. 5.6a than that in Fig. 5.3 due to a larger value of δ of the sample. The larger roughness is displayed by a comparison of $P_{sc} = (1/I_0)dI/d\Omega$ in both figures; e.g., at $\theta = 40°$ one observes in Fig. 5.3: $P_{sc}^p \cong 1.4 \times 10^{-4}$ whereas in Fig. 5.6 $P_{sc}^{pp} \cong 60 \times 10^{-4}$ is registered. If one assumes that (5.1) or $P \sim \delta^2$ is still valid, a value of δ of about 60–70 Å results for the film referred to in Fig. 5.6a which seems reasonable. *Beaglehole* and *Hunderi* [5.10] have made a calculation of this second-order scattering intensity which fits the observed behavior.

A further argument for such double-order processes is the observation of reflectivities with crossed polarizers: incoming light p polarized, outgoing light s polarized or vice versa. In case of normal incidence s-polarized light means: E vector perpendicular to the plane of observation and p-polarized light: E vector in this plane.

These observations display that there is an intensity of sp and ps scattering which in the case of Fig. 5.3 is more than an order weaker than the pp intensity. It is characteristic for the sp intensity that it is a maximum at a θ value of about 50°, see Fig. 5.7, whereas the ps intensity decreases monotonically as the ss scattering. This bulge in the sp scattering is because of the double process just mentioned, i.e., transformation of the incoming light into p light and excitation of SPs which de-excite into radiation.

This explanation is confirmed by the same experiment as presented in Fig. 5.6b: measurements with light of frequency $\omega > \omega_s$ demonstrate that the bulge disappears under these conditions.
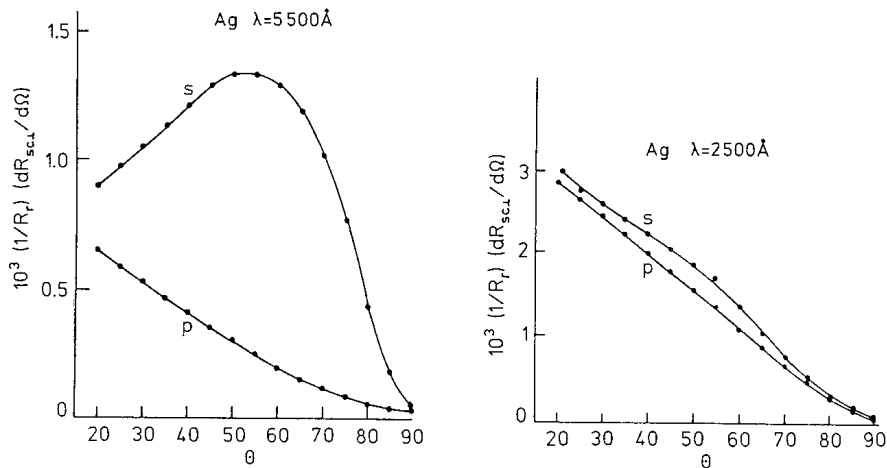
78

Fig. 5.7. Angular distribution of the crossed intensities (sp and ps). The left figure shows the bulge which disappears if the incoming light has a frequency $\omega > \omega_s$. From [5.10]

It is informative to note that these characteristics due to the double processes are still more striking on a silver film deposited on latex spheres of 890 Å diameter [5.11], see Fig. 5.8.

Similar experiments with diffusely scattered light form silver films, 5000 Å thick, roughened by underlayers of CaF_2 of some 1000 Å thickness have been reported [5.11]. The results confirm the measurements just described as, e.g., the different shape of the angular distributions of the pp and ss light and of sp and ps light.
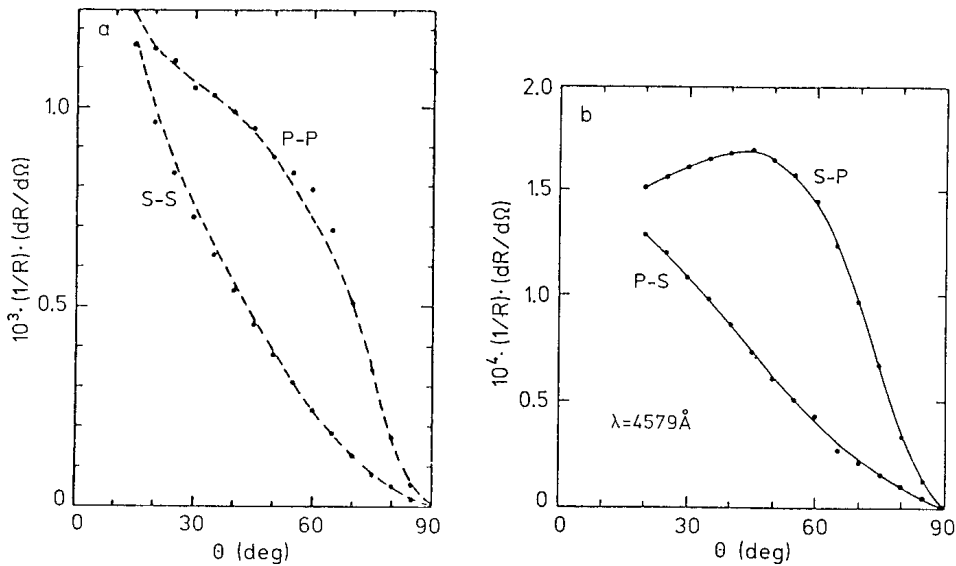

Fig. 5.8. (a) The intensity $(1/I_0)dI/d\Omega$ scattered from a rough silver film as a function of the scattering angle θ. Normal incidence ($\theta_0 = 0$). $\lambda = 4579$ Å. A four parameter fit gives $\delta = 40$ Å and $\sigma = 790$ Å and for the waviness 4 Å and 7000 Å. (b) The same sample yields the angular distribution for the s-p and p-s intensities. $\lambda = 4579$ Å. From [5.12]

79

In these experiments as well as in those mentioned before, the observed intensity rises for smaller Δk_x values in the region of $\theta = 20$–$30°$ instead of approaching the ordinate much smoother, as expected from Fig. 5.2. These long wavelength correlations are reduced on rougher surfaces.

If the scattered intensity would be described by one Gaussian function in the whole Δk_x region, the dependency (5.1) could be written at small Δk_x values

$$P = \frac{1}{I_0}\frac{dI}{d\Omega} = \text{const.}\left(1 - \frac{k_x^2\sigma^2}{4}\right) \tag{5.5}$$

for $k_x^2 < 4/\sigma^2$, whereby $\Delta k_x = k_x$ at normal incidence. The constant contains the k_x dependent term W_{ik}, but as Fig. 5.2 demonstrates, W_{pp} can be regarded as constant for the k_x region discussed above. The curve (5.5) approaches the ordinate nearly horizontally if P is plotted against k_x for $\theta < \approx 30°$. The observed P values, however, increase steeply at small k_x, see Fig. 5.3 etc. This indicates that the region of small k_x or of the long wavelength components (Λ) of the profile ($k_x = 2\pi/\Lambda$) stem from another roughness structure, very probably of the substrate profile.

This long wavelength component at $\Delta k_x < 1 \times 10^{-3}\,\text{Å}^{-1}$ can be evaluated and yields a Λ of about $1\,\text{m}\mu$ [3.1,18]; δ values of about $2\,\text{Å}$ and $\sigma = 7500\,\text{Å}$ are reported in [5.11].

Comment on the Double Processes

The above experiments demonstrate the influence of secondary processes. Recently, the linear relation (3.1) which yields the dependence of the scattered intensities P_{pp} and P_{ss} on δ^2 has been extended by using terms with δ^4. Thus, double processes can be taken into account in P_{pp} and P_{ss} and further for the crossed intensities, P_{sp} and P_{ps}. These calculations are based on the theory of *Brown* et al. [4.15].

Calculations have been performed with one Gaussian function and different δ values: 5, 15, 25, 40, 70, 120, and $150\,\text{Å}$, $\sigma = 1000\,\text{Å}$ and $\lambda = 5145\,\text{Å}$. Figure 5.9 demonstrates an example for $\delta = 40\,\text{Å}$. It shows the characteristic bulges: the pp curve is larger than the ss curve for two reasons: (1) the angular function W_{pp} is larger than W_{ss}; this is valid already in the linear approximation. (2) The double process: SP excitation followed by de-excitation and emission of light, which produces additional p light. Furthermore, in contrast to the monotonically decreasing ps light, here the strong bulges in the sp curve are recognized in the crossed intensities.

Comparing the curves of this model with different δ values the following results can be derived:

1. the quotient $(ss/pp)_{\text{max}}$ at $\theta \approx 52°$, the maximum of the sp intensity, is nearly constant, 2.5 ± 0.3, independent on δ,
2. the quotient $(sp/ps)_{\text{max}}$ decreases very slowly from 6.7 to 3,
3. the quotient ss/ps, taken at $\theta = 52°$, decreases rapidly by about 10^3 with increasing roughness.

80
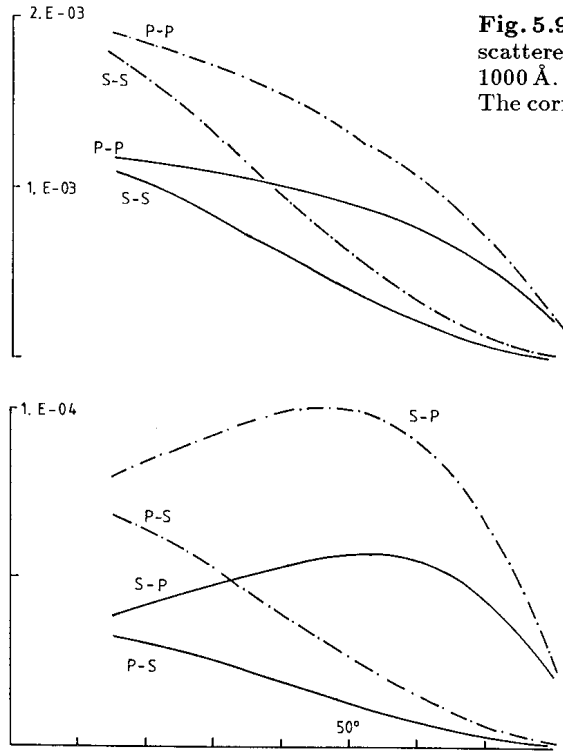
Fig. 5.9. Calculated angular distribution of light scattered at a surface with $\delta = 40\,\text{Å}$ and $\sigma = 1000\,\text{Å}$. (——): $\lambda = 5145\,\text{Å}$, (—·—): $\lambda = 4579\,\text{Å}$. The correlation function $|s(\Delta k_x)|^2$ is a Gaussian

Results (1) and (2) are a consequence of the fact the P_{pp} and P_{ss} are essentially dependent on δ^2, whereas P_{sp} and P_{ps} depend on δ^4. Result (3) comes from the different dependence on δ, so that $ss/ps{\sim}1/\delta^2$.

Very schematically the result of these calculations can be condensed in the following relations: For normal incidence with $\theta_0 = 0°$, the relative scattering intensity (or the relative reflectivity) follows

$$R^{pp} = [\text{first order term}] \quad \{1 - \delta^2 A B_1\}$$
$$R^{sp} = [\text{first order term}] \quad \{ - \delta^2 A B_1\}$$
$$R^{ss} = [\text{first order term}] \quad \{1 - \delta^2 A B_2\}$$
$$R^{ps} = [\text{first order term}] \quad \{ - \delta^2 A B_2\} \ ,$$

$\{\ \}$ represent the corrections to the first order terms. The relations for A, B_1, B_2 are too cumbersome to be reproduced here, see [4.15].

It remains to understand that Fig. 5.3 shows no bulge in sp scattering at small roughness. A possibility is that the long wavelength scattering at small $k_x{<}10^{-3}\,\text{Å}^{-1}$ which depends on the structure of the substrate given by δ_s and σ_s is more or less independent of the roughness of the silver film as has been already mentioned. Apparently the bulge intensity sp disappears in this "background" of the long wavelength scattering at small roughness. Since P_{sp} (and P_{ps}) increase rapidly with δ^4, the bulge structure will become visible at

larger δ values. One can estimate that this will happen at a δ value of about 50 Å.

Further experiments with supersmooth substrates could clarify this issue.

5.2 Scattering of X-Rays

In the context of scattering without SPs the experiments with x-rays and their results shall be mentioned, based on the same equations. The observation with x-rays is performed at grazing incidence to fulfill the condition $\delta \ll \lambda$. With θ_0 the angle of specular reflection, this condition is more precisely

$$\cos \theta_0 \cdot \delta \ll \lambda \tag{5.6}$$

or the projection of the roughness on the beam direction has to be $\ll \lambda$. If $\lambda \approx 5$–10 Å and δ is comparable to λ or smaller, θ_0 has to be near $90°$. For example, $\lambda = 8.3$ Å (Al,K) and $\theta_0 = 89°$ fulfills this condition and thus allows the application of the linear scattering theory. Further, the reflected intensity will be high. The grazing incidence has the advantage that $\theta_0 \lesssim 1°$ is smaller than the critical angle of total reflection which guarantees a reflectivity of at least 20 %.

The interest of such x-ray experiments lies in the feasibility of constructing telescopes of the Wolter type for x-ray astronomy. These need very smooth mirrors to reduce the losses due to roughness scattering since the x-ray objects emit at a very weak intensity.

The scattered intensity is given by the relation (5.1)

$$P = \frac{1}{I_0} \frac{dI}{d\Omega} = \frac{1}{4} \left(\frac{\omega}{c} \right)^4 \frac{|W|^2}{\cos \theta_0} |s|^2 \ . \tag{5.7}$$

Since θ and θ_0 are nearly $90°$, the dipole function $|W|^2$, see (5.2,3) degenerates with $\varphi = 90 - \theta$ into [2.4, Chap. 9, p. 397, (48)].

$$W_{pp} = W_{ss} = 4\varphi_0 \varphi \tag{5.8}$$

$$P = \left(\frac{\omega}{c} \right)^4 \varphi_0^2 \varphi^2 |s|^2 \ . \tag{5.9}$$

This relation is valid for insulators as well as for metals if φ and φ_0 are smaller than $\sqrt{|\varepsilon - 1|} = \sqrt{2|n - 1|}$, see (5.3). For gold with $|n - 1| \approx 10^{-3}$ at $\lambda = 8.3$ Å; this means that φ_0 has to be smaller than $3°$. Under this condition the scattered intensity is practically concentrated around the specular reflected beam. This is a typical limiting case in which the result becomes independent of the polarization direction of the electromagnetic field, see (5.7). It is often called "scalar case".

82

An example of such a measurement is seen in Fig. 5.10a. The scattered intensity appears as a halo around the central beam. The latter is not well pronounced since the surface is not very smooth, but the wings around the center clearly display the intensity due to the scattering by the roughness. The best fit with (5.7) is obtained with an exponential function for $|s|^2$. In this case one assumes a correlation function

$$G(x) = \delta^2 \exp\left(-\frac{x}{\sigma}\right) \tag{5.10}$$

so that the Fourier transform
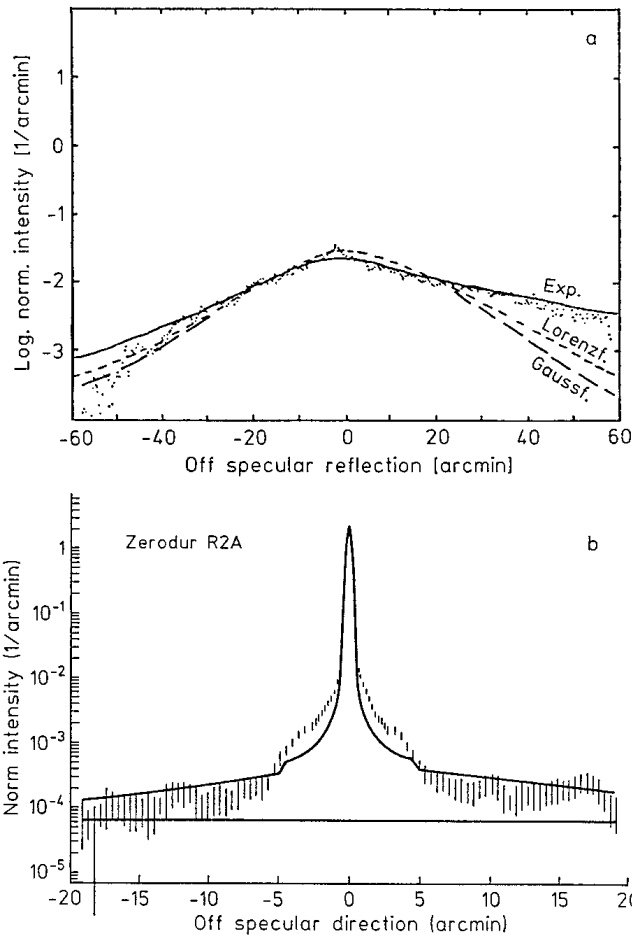
Fig. 5.10. (a) Diffuse scattering of x-rays, $\lambda = 8.3\,\text{Å}$, of a Kanigin surface around the specular reflected beam. Angle of incidence $98°$. Different roughness functions are fitted; the exponential function gives the best fit. The left-side intensity distribution is influenced for $\varphi - \varphi_0 > 40$ arc min by the reflecting surface. From [5.13]. (b) Intensity distribution around the specular beam reflected at a Zerodur mirror at a grazing angle of 60 arc min for $\lambda = 8.3\,\text{Å}$. This surface is essentially better polished (δ a few Å) so that the specular beam is much more intense. The halo is due to the diffuse scattering of the surface, whereas the intensity in the immediate environment of the specular beam at small k_x values points to long wavelength modulation similar to the phenomenon at light scattering, see Chap. 3. From [5.13]

$$|s(\Delta k_x)|^2 = \frac{1}{2\pi} \frac{\delta^2 \sigma}{|1 + (\sigma \Delta k_x)^2|^{3/2}} \tag{5.11}$$

comes out. The roughness parameters are $\delta = 86{\pm}10\,\text{Å}$ and $\sigma = 11{\pm}6\,\text{m}\mu$ [5.13].

Better polished surfaces of Zerodur glass overcoated with a gold film of several hundred angstrom thickness give values of $\delta = 2.7{\pm}0.1$ up to $4.9{\pm}0.1\,\text{Å}$ with $\sigma = 2.6{\pm}0.7$ up to $5.0{\pm}2.5\,\text{m}\mu$. These scattering patterns have a pronounced specular beam of nearly four orders higher than the halo intensity, see Fig. 5.10b [5.13]. It is remarkable that these patterns display very near to the primary beam (within ± 5 arc min) an excess intensity which has very probably the same origin as the intensity at low Δk_x values in Figs. 3.8 and 5.4, namely in the waviness of the substrate. It is surprising that Λ, its wavelength, in these examples has similar values of about several millimicrons. It stems probably from the fabrication of the surface.

These values of the r.m.s. height of the mirror surfaces have been confirmed by measurements on the same samples with the electron interference microscope which has a high spatial resolution normal to the surface; the lateral resolution is of the order of the light wavelength. For example, the mean roughness value of $\delta = 2.5{\pm}0.4\,\text{Å}$ obtained with x-rays agrees with the value of $2.7{\pm}0.9\,\text{Å}$ evaluated with the electron microscope from the same specimen [5.12].

The method of reflection of x-rays in grazing incidence has also been applied to investigate the "roughness" of a water surface; a r.m.s. height of $3.2\,\text{Å}$ has been measured, averaged over a surface of $3000\,\text{Å} \times 3000\,\text{Å}$ [5.14].

5.3 Measurement of the Reflectivity Deficit as a Function of the Wavelength

Earlier experiments on Al surfaces at nearly normal incidence, θ_0 several degrees, showed a dip in the reflected intensity as a function of λ near $\lambda = 1300\,\text{Å}$, see [5.15,16]. This "anomaly" has also been observed for silver and magnesium. It is due to the excitation of SPs via roughness by the incoming light (grating coupler) and reduces the reflected light in the energy region $\hbar\omega \lesssim \hbar\omega_{sp}$. This interpretation has been verified by depositing CaF_2 or MgF_2 layers on the substrate before vaporizing the metal films on it: The deficit increases with increasing thickness of the crystalline layers or with the roughness of the Al film, as Fig. 5.11 demonstrates at Al [5.17].

This dip ΔR causes a peak in the absorption A since in $1 = R + A + T$ the transmission T is zero so that a reduction in R implies an increase in A. It is seen in the dependence of ε'', the imaginary part of $\varepsilon(\omega)$, on the wavelength λ, in a silver film, see Fig. 5.12. The films 1–4 have been prepared with a vaporization rate of $\approx 100\,\text{Å/s}$ on an untreated glass substrate in four different preparations under equal conditions. The roughness has been enhanced by underlying MgF_2 films, $2000\,\text{Å}$ thick. The fluctuations are due to variations of the preparation parameters [5.18].

84
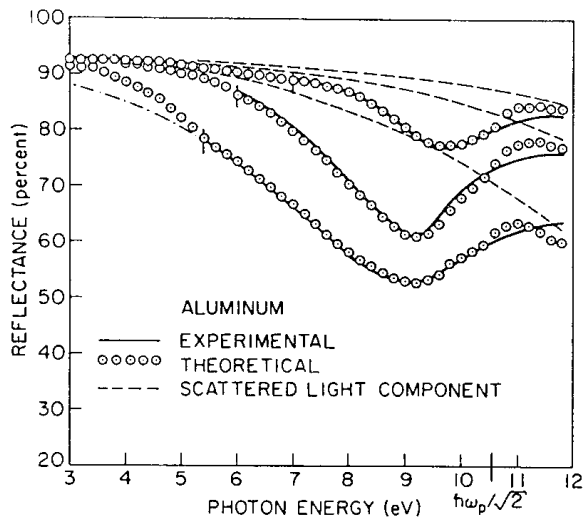
Fig. 5.11. Comparison of measured and calculated reflectivity of rough surfaces of evaporated Al films of 800–1000 Å thickness; angle of incidence 10°. For the calculated curves the parameter (δ, σ) in Å have been taken: (12.1; 918), (14.7; 744), and (37.7; 378), from top to bottom. From [5.17]
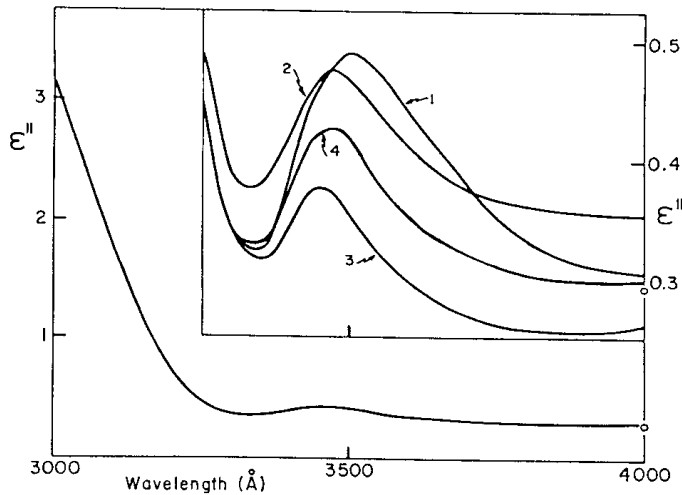
Fig. 5.12. The imaginary part of $\varepsilon(\omega)$ as a function of the wavelength of a silver film evaporated on a glass substrate coated with MgF$_2$. This additional absorption is due to surface roughness (excitation of SP). From [5.18]

Additional absorption in the region of ≈ 3500 Å on a rough surface of a thick silver film compared to the surface smoothened by annealing has been reported in [5.19].

Another proof of this explanation is given by the displacement of the dip to longer wavelengths if the silver film is coated with thin films of CaF$_2$, MgF$_2$, LiF, or carbon. An example is displayed in Fig. 5.13; here carbon leads to a nearly complete damping of the SPs [5.20]. More detailed measurements of this deficit have been made on different metals as Ag (*Stanford* in [5.21]), Al (*Endriz* and *Spicer* [5.17], *Daudé* et al. [5.21]), and Mg (*Gsell* et al. [5.22]), and compared with calculated results to obtain the roughness parameters.
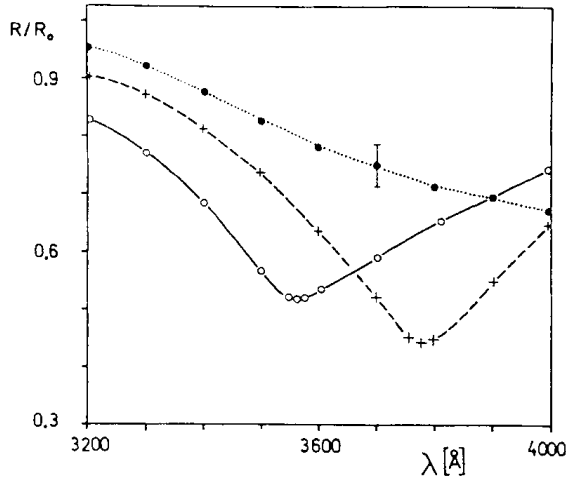
Fig. 5.13. The reflection deficit R/R_0, the ratio of the reflection of a rough and of a nearly smooth surface of a silver film, evaporated on a glass substrate, without coating (ooo), with a CaF_2 layer of $1\,\mu$ thickness (---) and with a carbon layer 50 Å thick ($\cdot\cdot\cdot$). The reflection minimum displaces and gets damped by coatings which change the SP dispersion. From [5.20]

Theoretical Considerations

Elson and *Ritchie* [5.23], using first-order perturbation theory, have calculated the intensity deficit ΔR_{SP} due to the SP excitation. They obtained the probability with which a photon produces one SP on a rough surface at normal incidence:

$$\tilde{P}_{SP} = \left(\frac{\omega}{c}\right)^4 |s(\Delta k_x)|^2 \frac{\varepsilon_1'^{\,2}}{(|\varepsilon_1'| - 1)^{5/2}} \ , \tag{5.12}$$

$|s(\Delta k_x)|^2 = |s(k_x)|^2$ because of the normal incidence $k_x^0 = 0$. To include damping the expression $\tilde{P}_{SP}$ is incorporated with a Lorentzian damping function, so that

$$P_{SP}(\omega) = \int\limits_0^{\omega_{sp}} \tilde{P}_{SP}(\omega') \frac{\gamma'/2}{(\omega - \omega')^2 + (\gamma'/2)^2} d\omega' \ , \tag{5.13}$$

γ' includes all effects damping the SPs. In the case of a free-electron gas with $\varepsilon'' = (1/\omega\tau)(\omega_p/\omega)^2$, γ' becomes $\gamma = 1/\tau$ with τ the relaxation time of the free-electron gas. The value of γ' will increase on rough surfaces by additional processes as radiation damping. The function $\tilde{P}_{SP}$ has no pole at $|\varepsilon_1'| = 1$ since the term $|s|^2$, an assumed Gaussian correlation function, goes to zero for $|\varepsilon_1'| \to 1$ or $k_x \to \infty$.

For $P_{SP} \ll 1$ (first-order approximation) one obtaines, see e.g., [5.22]

$$\Delta R_{SP}/R_0 = P_{SP} \ . \tag{5.14}$$

This value of P_{SP} has to be completed by the loss probability P_{sc} produced by the light scattered diffusely into the air space inside the light cone and is given by (5.1). Its contribution is about a factor 5–10 smaller than P_{SP} in the deepest part of the reflection minimum depending on the ratio σ/λ_p, where λ_p is the plasma wavelength, see Fig. 4 in [5.23].

The observed curves were fitted with the equation

$$\Delta R_{\text{tot}}/R_0 = P_{\text{SP}} + P_{\text{sc}} \tag{5.15}$$

and yield δ, σ, and γ.

Experimental Results

The observed reflectivities of Ag, Al, and Mg films, produced by evaporation, have been evaluated. The results of Al, measured in UH vacuum, are displayed in Fig. 5.11. The roughness has been increased by overcoating the substrate (quartz plates) with CaF_2 films of different thickness. The comparison of measured and calculated curves shows that the shape of the minimum and its change with increasing roughness can be reproduced using the Gauss model for $|s(k_x)|^2$ with the data given in Fig. 5.11. The value of γ' came out with a relaxation time of $\tau = 1.5 \times 10^{-15}$ s which is very near to $\tau = 1.4 \times 10^{-15}$ s measured from the width of the volume plasmon $\hbar\omega_p = 15$ eV with a half width $\Delta E^{1/2} = 500$ meV [2.3b] and $\tau = 1.3 \times 10^{-15}$ s from reflectivity measurements [5.24].

The reflectivity deficit at photon energies higher than $\hbar\omega_{\text{SP}}$ is due to light scattering into the light cone $k_x \leq \omega/c$, which is indicated in Fig. 5.11 by dashed curves and shows the strong increase with larger photon energies $(\sim\omega^4)$.

It is very probable that due to the relatively small δ values of the two upper curves, validity of the linear approximation can be assumed and the changes of the dispersion relation, $\Delta\theta_0$ and $\Delta\theta_0^{1/2}$, therefore remain small. Furthermore the agreement of γ and γ' is a good reason to believe that δ and σ represent real data of the surface. The value of $\delta = 37.7$ Å of the lowest curve lies probably at the limit of the linear approximation.

Similar experiments on Al films and the determination of their roughness parameters have been published with comparable results [5.21]. These authors found, for example, a δ of 8 Å and a value of $\sigma = 320$ Å on an Al film, 900 Å thick.

Furthermore, measurements have been published on magnesium films of different thickness d evaporated on glass microscope slides, which have been evaluated as just described for Al. The results for three films are:

d: 450 Å	δ: 27 Å	σ: 180 Å
450 Å	29 Å	160 Å
1000 Å	45 Å	375 Å

The value of γ' comes out as $\hbar\gamma' = 1.9$–2.4 eV whereas the metal has a value $\hbar\gamma = 0.4$ eV. This increase of γ' compared to γ indicates that roughness has a strong influence on the data, since they lie at the limit of the linear approximation.

Application of Measuring ΔR_{max} to Roughness Determination

The deficit in the reflectance offers a practical method to obtain the roughness rather quickly. *Cunningham* and *Braundmeier* [5.25] report that the maximum deficit ΔR_{max} of Ag at about $\lambda = 3500\,\text{Å}$ as a function of δ yields a linear dependence. The value of δ has been obtained by interferometric methods (FECO: observation of the Fringes of Equal Chromatic Order) [5.26], which allows measurement of δ values of about $10\,\text{Å}$ up to several $10^3\,\text{Å}$; its lateral resolution is of the order of the light wavelength. Using this calibration the roughness of a silver surface can be derived from ΔR_{max} without referring to theoretical formulas.

There is an uncertainty concerning the calibration: the correlation of ΔR_{max} as a function of δ agrees with that of Fig. 7 in [5.17] only in the region of about $15–20\,\text{Å}$ ($\Delta R_{max} \approx 15–20\,\%$); the reason for this is unknown. This discrepancy in the calibration should be resolved so that this method could have wider applications.

A further advantage of this method is that a silver film of $500–1000\,\text{Å}$ thickness overcoating surfaces of other materials, replicates their structure and thus allows measurement of their roughness. Measurements with the ΔR_{max} method have been made to study the roughness of undoped and phosphorus-doped polycrystalline Si films [5.27].

## Surface Plasmons on Metal-Electrolyte Interfaces

Experiments with SPs have been reported in which the metal surface is covered with an aqueous solution instead of a solid thin film as described in Chap. 2. A second electrode allows application of a bias voltage to the system.

For the physics of the metal-solution interface it is of interest to study the behavior of SPs under these conditions. Light reflection at different wavelengths has been used. Surface Plasmon excitation is possible by surface corrugation and will be observed by the intensity deficit of the reflected light, see Sect. 5.3. In order to improve the sensitivity of the electro-reflectance method the signal has been differentiated, so that small changes of the reflectivity $\Delta R/R$ can be detected.

Instead of roughening the silver surface by an anodic potential cycle (dissolving silver and redepositing it), a stepped (110) Ag plane has been used, tilted by $3°$ against the (110) plane with the steps along the [001] direction; this gives a better defined roughness than a statistical one [5.28]. Figure 5.14 shows the strong difference, between the measurements of $\Delta R/R$ perpendicular to the steps (full line), and parallel to the steps (dashed line). In the latter case a small statistical roughness is effective, whereas the pronounced corrugation of the steps is responsible for the SPs at around $= 3.5\,\text{eV}$ instead of $3.63\,\text{eV}$ at a free silver surface. An evaluation of the reflectivity deficit similar to that described in scattering experiments in air, see Sect. 5.1, is not reported.

For further experiments on such metal-solution interfaces and more detailed information see [5.29].
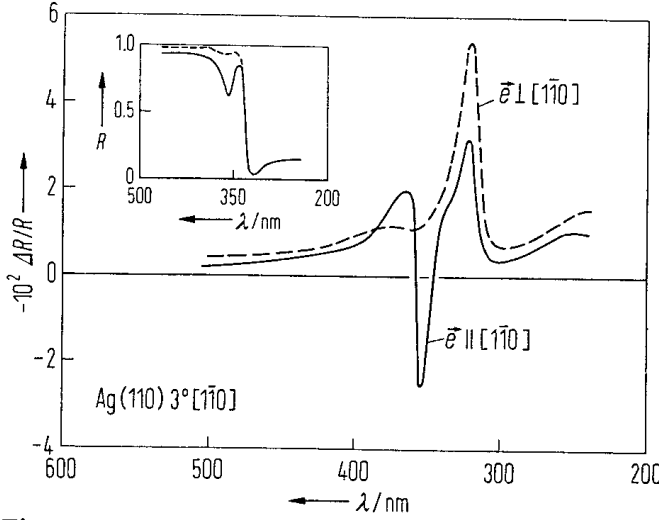
Fig. 5.14. The figure displays normal incidence electro-reflectance spectra $\Delta R/R(\lambda)$ and static reflectance spectra $R(\lambda)$ of a stepped Ag (110) surface in an aequeous solution (0.5 MNa-ClO$_4$) with p-polarized light. The *dashed curve* $\Delta R/R$ is measured parallel to the steps and shows only a weak structure besides the plasma edge. Perpendicular to the steps a remarkable additional structure is observed (——); it lies at around 3500 Å (3.5 eV) at which the condition ε' (Ag)$= - \varepsilon_0$ (H$_2$O) with $\varepsilon_0 = 2$ for SPs (with large k_x) is fulfilled. The excitation of SPs is possible due to the coupling of the light with the stepped metal surface. From [5.28]

Total Integrated Scattering (TIS)

In this context the procedure of determining the roughness by the "total integrated scattering" method will be discussed: a light beam hits the surface under investigation nearly in the normal direction, $\theta \approx 0°$. A hemisphere (Coblentz sphere) covering the rough surface, collects the diffusely scattered light R_{sc} on a light detector inside the half sphere. The specularly reflected light plus R_{sc} yields the total reflected light R_{tot}. The "total integrated scattering" is defined as TIS $= R_{sc}/R_{tot}$; where R_{sc} and R_{tot} are measured.

To determine the roughness one assumes first $|\varepsilon_1'|\gg1$ and $|\varepsilon_1'|>\varepsilon_1''$, together with a Gaussian correlation function. Then one introduces the condition that the illuminating λ is small compared to the correlation length $\sigma : k\sigma\gg1$. Large $|\varepsilon_1'|$ are identical with very long wavelengths, so that the angular functions (5.2) and (5.3) reduce to $|W_{pp}|^2 = |W_{ss}|^2 = (2\ \cos\theta)^2{=}4$, since $\theta_0{\simeq}0$, see Chap. 9 of [2.4].

The integration of the scattered light $(1/I_0)(dI/d\Omega)$ (5.1) over $d\Omega$ can be performed, since the roughness function $|s(\Delta k_x)|^2 = |s(k_x)|^2$ $(k_x^0 = 0)$ can be approximated by a Dirac delta function [4.16].

$$\frac{R_{sc}}{R_{tot}} = \left(\frac{4\pi\delta}{\lambda}\right)^2 .$$ (5.16)

The assumption $|\varepsilon_1'|\gg1$ implies that the relations (5.2) and (5.3) become independent of the polarization of the light $W_{pp} = W_{ss}$ (the so-called "scalar case").

89

Further SP excitation is excluded since the energy of the exciting photon is too small, see (5.4).

As (5.16) is valid only under the above restricting conditions, the application to visible light leads only to approximate results. The integration of the intensity over the half sphere prevents further control of the applied correlation function. The advantage of this method, however, is its simplicity to obtain quickly an approximate roughness value, which is important for practical purposes. A more detailed discussion can be found in *Elson* et al. [5.30].

6. Surface Plasmons on Gratings

In the following, experimental and theoretical results are reviewed which describe the effect of a grating on the propagation of SPs. Similar to Chap. 3 first the emission of light, enhanced by SP excitation, is discussed at smaller amplitudes of the grating; it is compared to that of gratings without SP excitation. Stronger corrugation leads to changes of the dispersion relation of the SPs which can be recognized by the changes in position of the reflection minima with increasing roughness. Correlated with the excitation of SPs, the electromagnetic field at the surface is enhanced in a similar fashion to smooth surfaces; the importance of the enhancement for the generation of the second harmonic and for the surface enhanced Raman scattering (SERS) is discussed. If SPs are reflected at the grating under special conditions, the reflected and the primary SPs couple with each other and energy gaps are produced.

A rough surface can be decomposed into its harmonic components with a continuum of $k_r = 2\pi/a$ values. It is therefore promising for a better understanding of the SP-phonon interaction to look at a surface containing only one of these components, i.e., gratings described by $S(x) = h\sin(2\pi/a)x$.

This restriction on a sinusoidal profile brings not only a simplification in the experiments since a holographic or interference grating can be better reproduced than a rough surface, the theoretical treatment is also easier.

The experiments can be performed in two ways:

a) The ATR Method. Here the silver/air interface has the profile of a grating, see Fig. 6.1. The gratings are produced by vaporizing a metal film, e.g., Ag of about 5×10^2 Å thickness, on a photoresist grating which has been prepared by illuminating a plane photoresist (Shipley AZ 1350) film, deposited on a glass
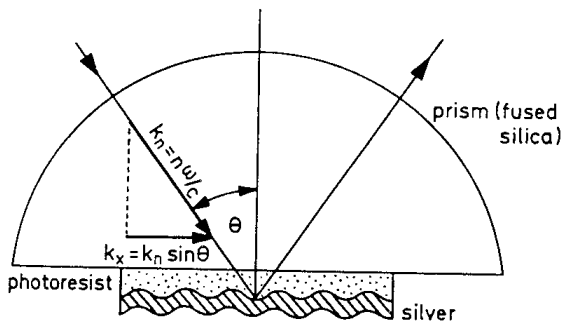
Fig. 6.1. Experimental device to study the properties of SPs on a sinusoidal surface. The grating constant a and the amplitude h can be varied independent of the light frequency and metal. From [6.1]

or quartz slide, with the interference pattern of light of wavelength λ. Chemical development of the illuminated photoresist film yields a sinusoidal profile [6.1–3]. The amplitude h of the profile, which depends on the time of exposure, is obtained by measuring the relative intensity of its first-order diffraction with s-polarized light using the relations given below.

This device can be used in two ways: either observing the reflected beam or looking at the light scattered from the grating surface, "scattering device".

b) Reflection Method. The light coming from the air side is reflected at the surface of the grating described above, see Fig. 6.2. This is the classical device for light spectroscopy with gratings. Here the SPs are produced via a grating coupler, see Sect. 2.7.

Both experimental devices have been used. The results are described in this chapter.
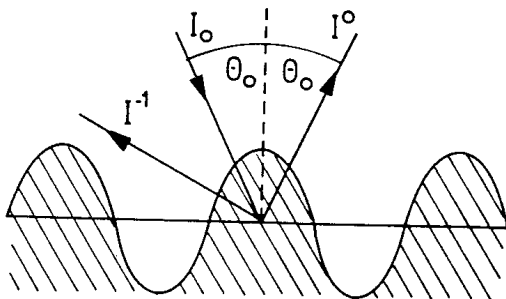

Fig. 6.2. Reflection of light at a grating

6.1 Emission of Light from Sinusoidal Gratings Supported by Surface Plasmons

Analogous to the observation on rough surfaces, the excitation of SPs on gratings can be observed by the emitted light. In the experimental arrangement, see Fig. 6.1, the rough surface has been replaced by a metal film with a sinusoidal surface. In contrast to rough surfaces the scattered intensity is concentrated in some needle-like diffraction maxima. Figure 6.3 demonstrates the light emission into the (-1)th diffraction order at the air side as a function of the angle of incidence θ_0 for two h values: $h = 3.3\,\text{Å}$ (above) and $h = 160\,\text{Å}$ (h is the amplitude of the sinus profile) [6.4]. On the left the correlated reflection curve is reproduced. Both (a) and (b) differ in position and width due to the different value of h. The maximum excitation produces maximum light emission. The resonance case is not completely adjusted in Fig. 6.3, since the reflection minimum does not reach zero.
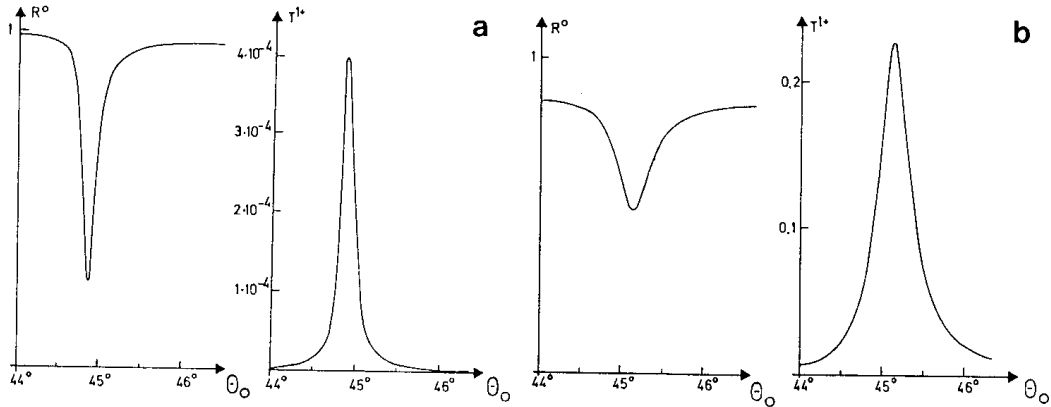
Fig. 6.3. Observed reflection R_0 and diffraction intensity T^{1+} ($n = +1$) at a grating with $a = 5930$ Å, $h = 3.3$ Å (a) and $h = 160$ Å (b) ($\lambda = 6471$ Å). The value of $d\Omega$ of the detector has been decreased to $d\Omega = 5 \times 10^{-4}$ sr in order to reduce the diffuse stray light produced by the statistical roughness of the grating. From [6.4]

Remark

It is surprising that a grating of $h = 3.3$ Å can produce such a pronounced signal, although the statistical roughness is $\delta \approx 5$ Å: The solid angle $d\Omega$ has been 5×10^{-4} sr in Fig. 6.3, 10 times smaller than in Fig. 3.8. This gives for the relative intensity scattered approximately $dT^{1+}/d\Omega = 4 \times 10^{-4}/5 \times 10^{-4} = 0.8$. In contrast to this the intensity due to the statistical roughness of $\delta \approx 5$ Å amounts to about 0.6×10^{-3}. The latter value, due to the background, can thus be neglected.

Whereas in the case of statistical roughness it is of interest to know $|s|^2$, the Fourier transform of the roughness function in order to derive the roughness parameters, here the corrugation parameter, amplitude h and the grating constant a, are known from other reliable experiments see below. We therefore have the possibility to control the calculated relation between light emission and the corrugation parameter and to determine the limits of its validity.

Analogous to (3.1) a relation of the light intensity, emitted from a grating into air, can be derived, if SPs propagate along its surface; it has a similar structure to (3.1). For example, the relative p-polarized intensity emitted into the diffraction maximum, e.g., $n = -1$, is given by the relative transmitted intensity

$$T^{(-1)} = I^{(-1)}/I^{(0)} = \text{const.} \frac{1}{4}\left(\frac{\omega}{c}\right)^2 |t^p_{0R12}(\theta)|^2 h^2 \qquad (6.1)$$

with h^2 the square of the amplitude of the grating or the Fourier transform of the profile function $S(x) = h \sin(2\pi/a)x$, see (2.52), and $|t^p|^2$ the enhancement of the field intensity in the surface metal/air. The value of the constant contains the angular function, see [6.5]. This relation is a first-order approximation as is (3.1): $h \ll a$ and $h \ll \lambda$. The important term in (6.1) is given by the factor $|t^p_{0R12}|^2$, the Fresnel transmission coefficient for smooth surfaces for the layer system quartz (0)/resist (R)/silver (1)/air (2) which does not differ

93

essentially from $|t^p_{012}|^2$ given in (2.27). It reaches a maximum for the resonance angle and produces the peaks in Fig. 6.3. The numerical evaluation for different wavelengths and $a = 5930$ Å is shown in Fig. 6.4, which displays $(T^{(-1)}/h^2)^{1/2}$ as a function of h. It should be constant as long as (6.1) is valid. Its value agrees with the calculated value with an error of less than about 10 %, up to an h of about 70 Å for a sinusoidal profile, apparently the limit of the linear approximation [6.4]. The numerical agreement for $h < 70$ Å demonstrates further that the enhancement is described by $|t^p_{012}|^2$ correctly. The observed decrease of $(T^{(-1)}/h^2)^{1/2}$ for larger values of h agrees formally with the result that the enhancement on rough surfaces decreases with increasing roughness. A theory for higher corrugations will bring a better insight, but this does not yet exist.

This value of about 70 Å for the limit of the validity of the linear approximation of (6.1) can be compared to δ, the r.m.s. height of a rough surface: this limit lies at $\delta = 15$–20 Å, about 5 times less than $h = 70$ Å.

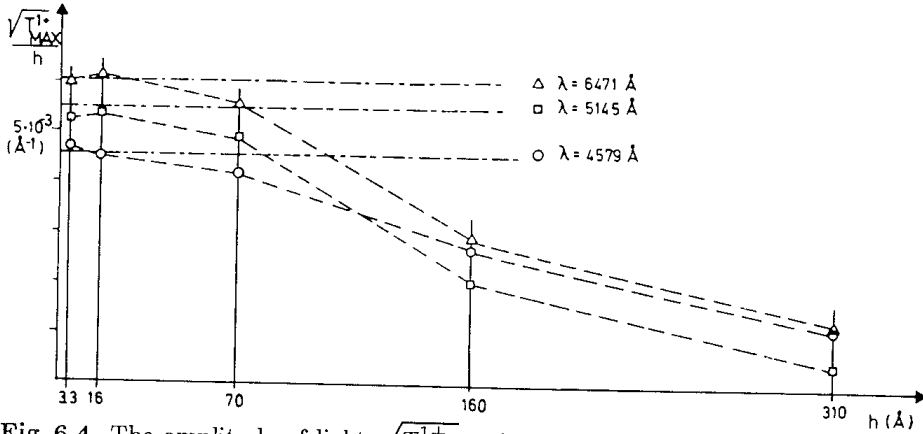**Fig. 6.4.** The amplitude of light $\sqrt{T^{1+}_{max}}$ emitted from a grating with $a = 5930$ Å into the first-order diffration divided by the amplitude h as a function of h at different wavelengths. The horizontal line (—·—) represents the result calculated with the first-order approximation. From [6.4]

Emission of Light From a Grating Without SPs

Irradiating gratings with light produces the specularly reflected beam $(n = 0)$ and in general diffraction maxima. The excitation of SP resonances can be avoided by using s light or p light outside of the resonance angles. It is of interest to look at the intensity of the diffraction maxima as a function of h, which is important for the determination of the amplitudes h of gratings. In the long wavelength approximation, ε'_1 large and $h/\lambda \ll 1$, the reflected intensity of the nth order at normal incidence for s- and p-polarized light ("scalar" case) is given by [6.6]:

$$R_n = \frac{I^{(n)}}{I_0} = J_1^2\left[\frac{2\pi h}{\lambda}(1 + \cos\theta_n)\right] \tag{6.2}$$

94

where J_1 denotes the Bessel function of the first kind. For $h/\lambda \ll 1$ one obtains

$$R_n = \frac{I^{(n)}}{I_0} = \frac{1}{4}\left[\frac{2\pi h}{\lambda}(1 + \cos\theta_n)\right]^2 \quad \text{or} \tag{6.3}$$

$$\frac{R_n}{h^2} = \text{const.} = \frac{1}{4}\left[\frac{2\pi}{\lambda}(1 + \cos\theta_n)\right]^2 . \tag{6.4}$$

This relation which is valid up to $h{\sim}300\,\text{Å}$, see Fig. 6.5 [6.7] gives the possibility to determine the value of h by measuring I_n/I_0 with s light to avoid the resonances, a procedure which has been used for the measurements of the amplitudes h [6.1,2]. The accuracy of the determination of h is $<4\,\%$ for silver, if $\theta_1 < 45°$ and $h/a < 0.1$ using $n = \pm 1$. This method has its advantage for small h values. At larger amplitudes h, the scanning electron microscope can be applied.
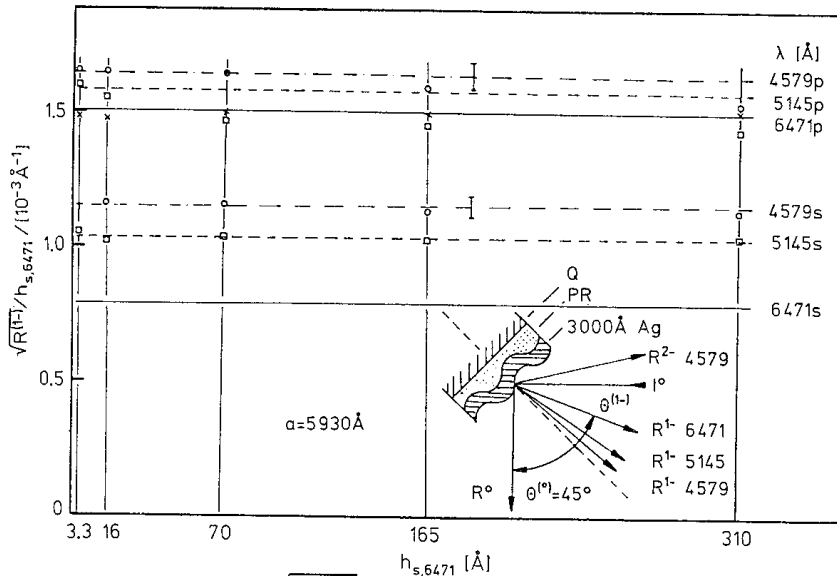

Fig. 6.5. The quotient $\sqrt{R^{(-1)}}/h$ measured on gratings with $a = 5930\,\text{Å}$ as a function of their amplitudes h at different wavelengths λ and with light of both polarizations. Angle of incidence $\theta^{(0)} = 45°$. The values of h have been determined with s-polarized light ($\lambda = 6471\,\text{Å}$). Horizontal lines: calculated; signs: experimental data. These observations show that the formulas are reliable up to values of $h \approx 300\,\text{Å}$. From [6.5]

If the values of ε_1' are not limited, Maxwell's equations give different expressions for s and p light. Again the quotient (R_n/h^2) is a function only of λ. The experimental control confirmed this behavior up to about $h = 300\,\text{Å}$ quantitatively for s and p light and different wavelengths at a silver grating of $a = 5930\,\text{Å}$ [6.7], see Fig. 6.6.

These measurements, especially those of R^0 and $R^{(-1)}$ have been extended up to about $h = 2500\,\text{Å}$ [6.8]. The results are displayed for s light in Fig. 6.6a
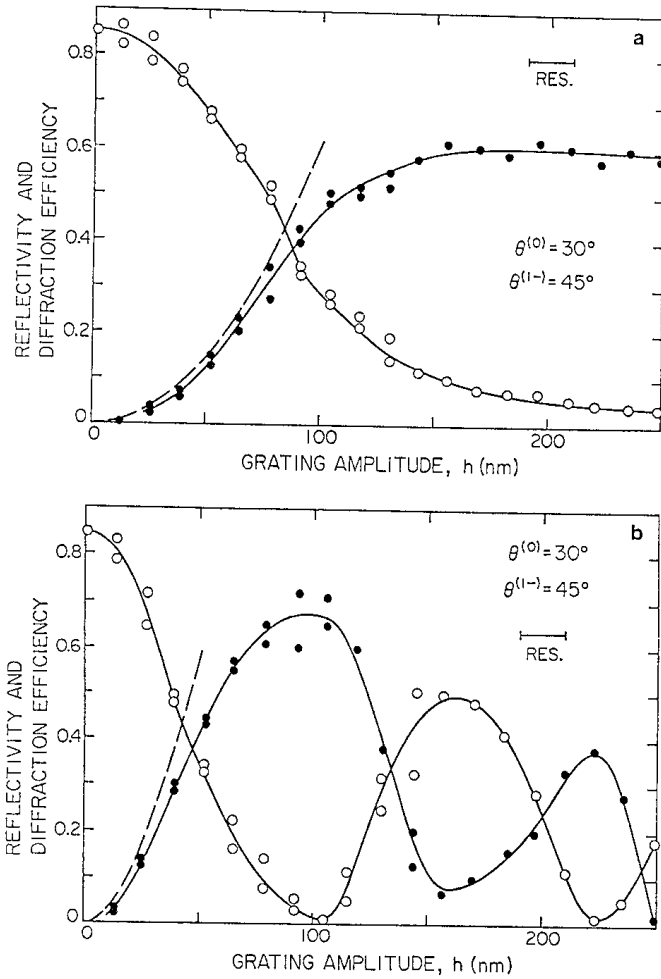
Fig. 6.6. (a) Relative reflected intensity R^0 (o) and diffracted intensity $R^{(-1)}$ (•) of s-polarized light ($\lambda = 6328$ Å) as a function of the amplitude of the sinusoidal grating with $a = 5200$ Å. (- - -): the linear approximation which is not valid beyond about 10 nm. (b) The same for p-polarized light. From [6.8]

at $\theta^0 = 30°$ and $\theta^{(-1)} = 45°$ with $a = 5200$ Å, silver, whereas Fig. 6.6b shows the same for p light. The oscillations of R^0 and $R^{(-1)}$ as a function of h are remarkable; they are not yet explained. The dashed lines indicate the linear approximations for a qualitative comparison with the results described above. At these large amplitudes h, the skin depth (2.9) is smaller than h which complicates the situation.

6.2 Dispersion Relation of Surface Plasmons on Sinusoidal Surfaces

If the amplitude h of the grating is increased, the observations demonstrate that besides the light emission, changes of the dispersion relation due to the

sinusoidal perturbation of the surface become evident: These results are derived from the behavior of the reflection minimum as a function of the amplitude h whereby the minimum is either observed in an ATR device [6.1,2] or in direct reflection [6.9].

The results are displayed in Fig. 6.7 for gold and silver. The positions of the minima displace to larger resonance angles by $\Delta\theta_0$, and the half widths $\Delta\theta^{1/2}$ increase with increasing amplitudes h. In both cases an approximate dependence on h^2 has been found. The dependency of λ and a (grating constant) are not yet known in detail; a comparison of Fig. 6.7a and b (silver, $a = 14\,910\,\text{Å}$ and $a = 4400\,\text{Å}$) displays that at constant λ the dependence on h is much stronger at $4400\,\text{Å}$ than at $14\,910\,\text{Å}$. Apparently the steeper walls of the grooves at a smaller grating constant support multiple scattering. The increase of $\Delta\theta_0$ and $\Delta\theta_0^{1/2}$, however, with increasing perturbation is not as large as on a rough surface, see Fig. 4.4.

The results shown in Fig. 6.7 mean a decrease of the phase velocity with increasing perturbation of the surface similar to that obtained at a rough surface. There is, however, a quantitative difference: An amplitude $h \approx 10\,\text{Å}$ of a sinusoidal grating shows no detectable effect; at $h \approx 100\,\text{Å}$ ($a = 4400\,\text{Å}$, $\lambda = 5682\,\text{Å}$, silver) a value of $\Delta\theta_0 \sim 0.1°$ can be observed, see Fig. 2 in [6.9], whereas a statistical roughness of δ of about $10\,\text{Å}$ displaces the minimum by about $1°$ at $\lambda = 5000\,\text{Å}$. Similar results are received for $\Delta\theta_0^{1/2}$.

The qualitative interpretation of these effects is as follows: the increased damping arises from the radiation losses into the air space which increase with h^2 in the first-order approximation, i.e., up to $h = 70\,\text{Å}$; beyond this limit the increase is slower than h^2, see Fig. 6.3. The decrease of the phase velocity is due to multiple scattering as discussed in Chap. 3.

Theoretical Remarks

In Fig. 6.7c, besides the experimental data, calculated values are shown. These data are obtained with the well-known Rayleigh method. The development of the field above the grating into the eigenfunctions of up to 20 harmonics, regarding the complex character of the dielectric function, yields a remarkable good agreement between observed and calculated data for silver and gold. The convergence is satisfied and is in agreement with the theoretical considerations that the Rayleigh method can be applied up to $h/a \sim 0.07$ for real metals [6.10].

The Rayleigh method has had the same success in describing the effect of the secondary harmonic in the profile of the sinusoidal grating on the shape of the first-order reflection, see below.

A look at the curves for gold Fig. 6.7c shows that the observed curves (full lines) lie somewhat beyond the calculated curves (points). The reason of this discrepancy lies probably in the relatively large value of ε'' of gold [6.9]. If ε'' is reduced formally by a factor of 5 the convergence improves [6.11].

In Fig. 6.7c the result of the second-order approximation of *Kröger* and *Kretschmann* [4.10] has been added as dashed lines. It shows a qualitative agreement and reproduces the general trend rather well, but the quantitative

◄ Fig. 6.7. a-c
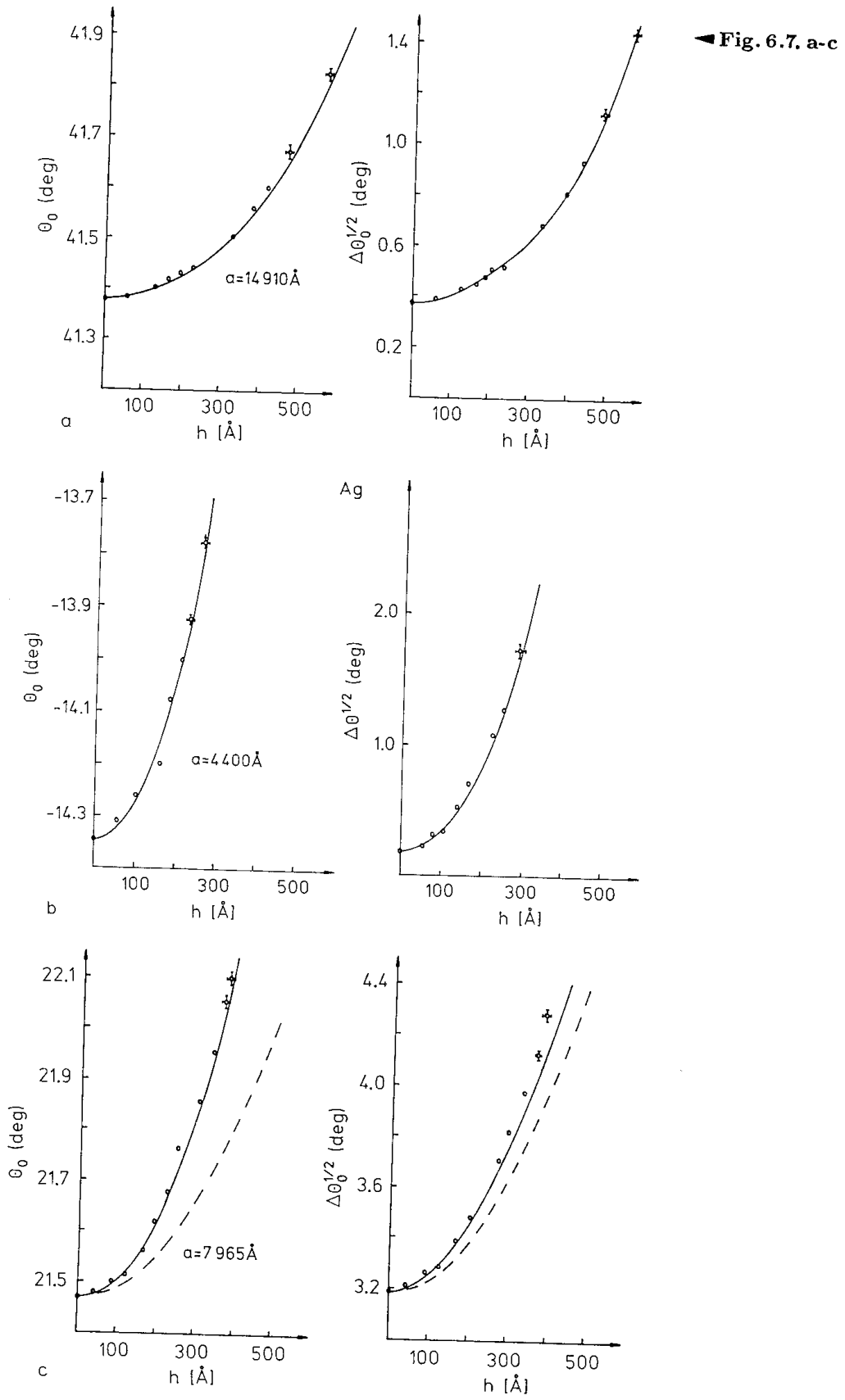
Fig. 6.7. The position of the resonance minima θ_0 *(left)* and their width $\Delta\theta_0^{1/2}$ *(right)* as a function of the amplitude h of the sinusoidal grating. **(a)** silver, $a = 14\,910$ Å, $\lambda = 5682$ Å; **(b)** silver, $a = 4400$ Å, $\lambda = 5682$ Å, **(c)** gold, $a = 7965$ Å, $\lambda = 5682$ Å. *Circles:* observed. *Full and broken lines:* calculated data. The values of $h = 0$ are obtained by extrapolation; the *dashed line* is calculated with the second-order approximation. From [6.9]

agreement is lacking. It is necessary to add many more higher orders to fit the observed values; this is accomplished by the Rayleigh method.

Another successful approach to calculate these observed curves has been developed: the exact integral formalism [6.12] which has been successfully applied to earlier measurements of the dispersion of SPs on sinusoidal profiles as a function of the amplitude of the grating [6.3].

6.3 Reflection of Light at Gratings with Excitation of Surface Plasmons

In Sects. 6.1,2 we have described the fundamental phenomena which occur by the interaction of SPs with a grating, especially a sinusoidal grating: the light emission in the resonance case and the change of the frequency and damping of the eigen modes by the grating.

In the following a more detailed description of some special effects are discussed which happen if SPs are excited by the grating coupler. The device is shown in Fig. 6.2; it is the classical method of light spectroscopy in reflection.

The interest comes from observations which state rapid variations of the intensity in a rather narrow region of the angle of incidence or of the wavelength. Such changes of intensity happen if diffraction maxima emerge or disappear and also if SPs are excited; the latter phenomenon is of special interest here. The results obtained at sinusoidal corrugations are rather clearly be described theoretically; if higher harmonics come into play, the situation gets complex.

Reflection of Light at a Sinusoidal Profile

If a grating is used for reflection experiments, see Sect. 6.2, which consists of a metal fulfilling the conditions for the excitation of SPs: $\varepsilon' < 0$ and $|\varepsilon'| > 1$ and $\varepsilon'' \ll \varepsilon'$, the intensity of the zero-order diffration ($n = 0$), the specular reflected beam, shows at the resonance angle given by (2.13) an intensity minimum see, Fig. 6.8 [6.13,14][1]. This is valid for p-polarized light, s light shows no minimum. The resonance appears for $k_x = (\omega/c)\sqrt{\varepsilon_1'/(\varepsilon_1' + 1)} = (\omega/c)\sin\theta \pm \nu g$, see Fig. 2.4 where $\Delta k_x = g$, provided we neglect the influence of the amplitude h.

This reflection minimum has been used as described already in Sect. 6.2 to determine the influence of the grating amplitude h on its position and its shape.

---

[1] A displacement of the ATR minimum with increasing amplitude of the gold grating up to $h = 600$ Å which should be at least 1° has not been observed in [6.14]. The reason of this discrepancy is not clear.
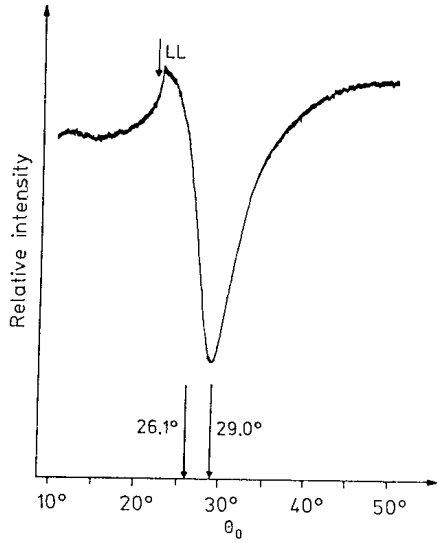
Fig. 6.8. Intensity of the zero-order reflection at a grating for p-polarized light. The minimum indicates the energy absorption due to SP excitation. LL means the positions of the light line. 26.1° is the calculated, 29.0° the observed position; the displacement is due to the corrugation of the silver surface. From [2.3b]

Furthermore, it is interesting that the depth of this minimum depends on the height h of the amplitude of the grating, see Fig. 6.9. There is a critical amplitude h_c at which the reflected intensity becomes zero, which indicates the strongest coupling of photons with SPs via corrugation. A similar situation has been found at rough (Fig. 4.1) and on smooth surfaces.

Another less pronounced structure "Wood's anomaly" is seen in Fig. 6.8; at $\theta_0 \approx 24°$ a discontinuity of the diffraction intensity is visible which is due to the disappearance of the diffraction order $n = +1$. The difference of the intensities above and below the break increases with h^2, since the diffraction intensity does so with h^2.

If the value of h passes the critical amplitude h_c, the minimum I^0 becomes rather asymmetric and the value of R above h_c no longer reaches the value below h_c as the points for I_0 in Fig. 6.10 demonstrate. Figure 6.10 shows, besides
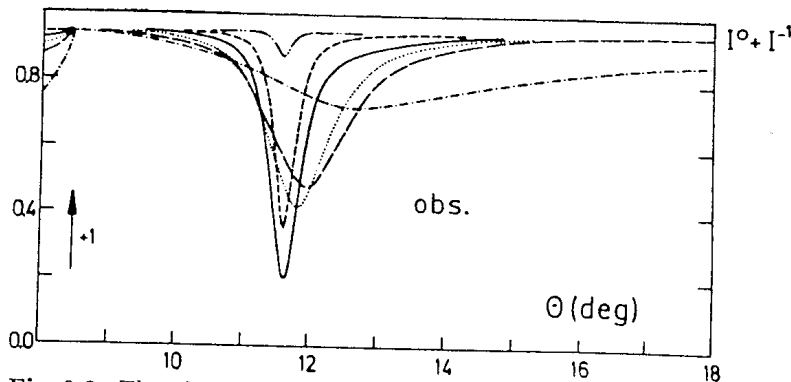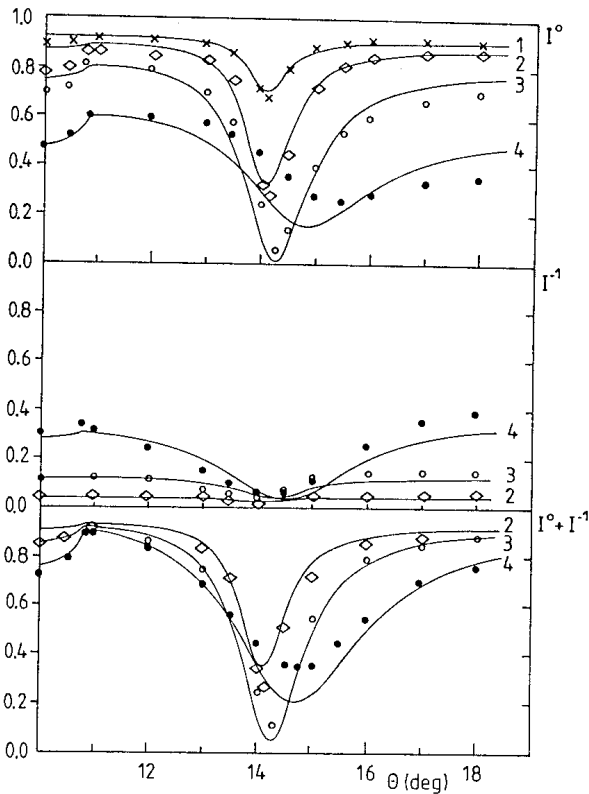

Fig. 6.9. The observed reflected $(I^0 + I^{-1})$ of a sinusoidal silver grating $(a = 6015\,\text{Å})$, the amplitude of the sinus profile as parameter as a function of the angle of incidence θ_0 $(\lambda = 5145\,\text{Å})$. At $h = 130\,\text{Å}$ the resonance is strongest leading to an enhancement of the electric field intensity of about 231. Values of h in [Å]: (—··—) 25; (---) 75; (——) 135; (···) 215; (—·—) 315; (———) 550. From [6.13]

100

Fig. 6.10. Observed *(points)* and calculated *(full lines)* intensity reflected at a sinusoidal gold (interference) grating with $a = 7965\,\text{Å}$ and $\lambda = 6471\,\text{Å}$. I^0 and I^{-1} are the intensities in the zeroth and (-1)st diffraction order; $I^0 + I^{-1}$ means the sum of both light intensities. These are relative intensities referred to the incoming intensity (I_0). The amplitude h of the profile is given as a parameter: *(1)* $89\,\text{Å}$, *(2)* $174\,\text{Å}$, *(3)* $308\,\text{Å}$, *(4)* $514\,\text{Å}$. The deepest minimum occurs at $h = 300\,\text{Å}$, at which an enhancement of $\left|t^p\right|^2 \approx 59$ is calculated using $(\varepsilon', \varepsilon'') = (-9.75; 1.1)$. the displacement of the minimum to higher angles and the increasing width of the minimum with larger h display the dependence of the dispersion relation of SP. (o) : amplitude h of the grating. From [6.16]

I^0, the data of I^{-1} reflected at a sinusoidal gold grating with $a = 7965\,\text{Å}$ at $\lambda = 6471\,\text{Å}$. If the intensities I^0 and I^{-1} are added, the intensities $I^0 + I^{-1}$ are lifted up so that a well-defined minimum is obtained, see Fig. 6.10 below.

These experimental results can be quantitatively described by existing theories. As we had explained in Sect. 6.2 the changes of the displacement $\Delta\theta_0$ of the ATR minimum as well as the increase of its width $\Delta\theta_0^{1/2}$ are quantitatively described by a Rayleigh method, which has its limit at $h/a = 0.07$. To calculate values at larger h/a, the extinction theorem of *Toigo* et al. [6.15] has been applied which enables sufficient convergence to be reached up to $h/a \sim 0.5$. A number of special grating questions have been treated which are discussed in Sect. 6.5.

Here in Fig. 6.10 the observed reflection curves as function of θ with h as parameter [6.9] are directly compared with the calculated curves of *Diaz* et al. [6.16]. The changes of the shape of the reflection minima are nearly quantitatively reproduced. Small discrepancies appear, e.g., on the silver grating at $\lambda = 5145$: the calculated minimum position comes out $0.5°$ smaller than the observed resonance angle. The ε values have to be taken $(-11/0.33)$ instead of the value of the literature $(-10.4/0.38)$; both ε values however are within the limits of the accuracy of the measurements.

Another example is shown in Fig. 6.11, in which the reflected intensity for a silver grating of $a = 20\,140\,\text{Å}$ and $h = 1200\,\text{Å}$ at a wavelength of $5682\,\text{Å}$ is displayed for different orders $n = 0$ up to $n = +4$ as a function of the angle
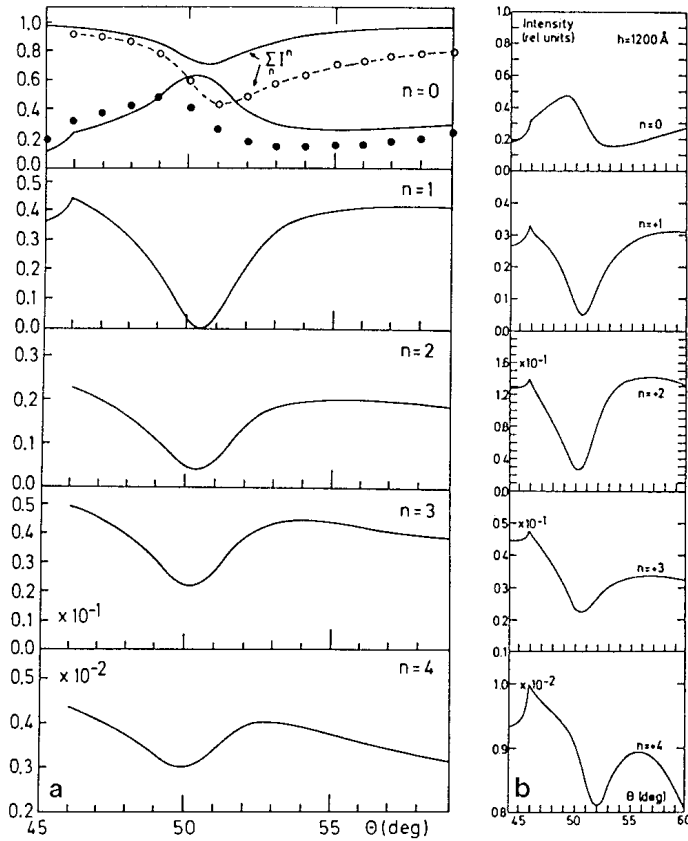
Fig. 6.11. Calculated reflectivities (a) (———) and experimental data (b) (———) of different diffraction orders n. The grating parameters are $h = 1200$ Å and $a = 20\,140$ Å; $\lambda = 5682$ Å. (●●●, ooo) in (a), $n = 0$, are observed data. From [6.16,17]

of incidence θ_0 [6.17]. Whereas the measured values, at right, demonstrate for $n = 0$ the deformation of I^0 similar to that in Fig. 6.10, the observed orders $n > 0$ show well-developed minima: At the top left, the measured values of $n = 0$ (dark dots, the same curve as $n = 0$ in Fig. 6.11b) are found to be in agreement with the calculated data (lower full line). In addition, the sum of the observed light intensities of all the orders $\Sigma I^{(n)}$, including $n = +5$ and $n = +6$ which are not reproduced in Fig. 6.11, is displayed by the open circles, showing a well-developed minimum. The upper full lines are the calculated values, in agreement with the observed data. At 45.9° the diffraction order disappears under the "horizon" so that the intensity has a discontinuity similar to that shown in Fig. 6.8. Further examples can be found in [6.17].

These direct comparisons of the calculated and observed data demonstrate that the extinction theorem is a very helpful procedure to reproduce the observed results. The physics, however, do not always become evident.

## Reflection of Light at Tunnel Junctions on Gratings

In the preceding parts of this section the reflection of light at metallic grating surfaces and their interaction with SPs has been reported. A variant has

been discussed in Sect. 4.7, where a tunnel junction has been laid down on the metal grating, see Fig. 4.12. But instead of looking at the light emitted from this junction, caused by the coupling of the tunnel electrons with the rough or sinusoidal metal layer, here the effect of the SPs excited by the light reflected at such a structured junction on the photocurrent through the junction is discussed. The enhanced field of the SPs influences the tunnel current in the MOM (metal-oxyd-metal) junction depending on the bias applied to both metal electrodes. Such junctions are Ag-Al_2O_3-Al and Al-Al_2O_3-Al [6.18]. The quantum efficiency, the number of electrons per photon, has a relatively small value of some 10^{-4}. The physical process of the described observations is in principal the same as the SP supported photoeffect, e.g., at a silver surface, which has a strong maximum in the resonance case, a phenomenon already described in [2.13] and later in [6.19].

Recently MIS junctions have been studied in which the metal e.g., silver, is replaced by a semiconductor as InP [6.20] and p-Si [6.21]. An interesting example is the Al (100–400 Å)-SiO_2(20 Å)-p-Si junction, see Fig. 6.12. If one observes the junction current through the Schottky barrier at a fixed angle of the incident light, strong and narrow light maxima are observed, if the take-off angle and the wavelength are varied (both depend on each other through the dispersion relation), see Fig. 6.13. This enhanced current is due to the strong field of the SPs on the Al surface, which produces electron-hole pairs in Si and thus the high current. The quantum efficiency depends on the thickness of the Al top layer; it amounts to 0.3 for a 110 Å Al top layer at $\lambda = 6328$ Å [6.21]. These devices are of interest for fast light detectors in narrow frequency bands.
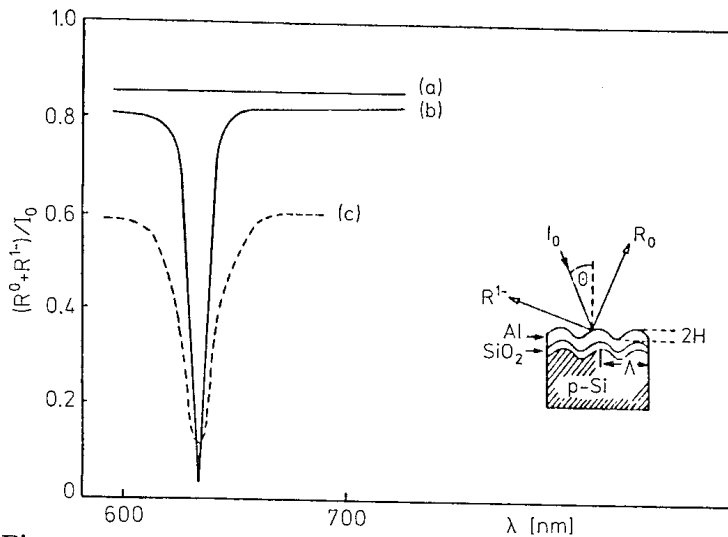
Fig. 6.12. The reflected intensity $R^{(-1)}$ at the MIS juntion, see insert. Curve (a) for a flat MIS structure, curve (b) for the junction Al (310 Å)-SiO_2-p-Si on a grating ($a = 3640$ Å, $h = 80$ Å), curve (c) for the junction Al (90 Å)-SiO_2-p-Si. At $\theta_i = 44°$ the reflection minimum at $\lambda = 6328$ Å indicates the SP resonance. From [6.18]
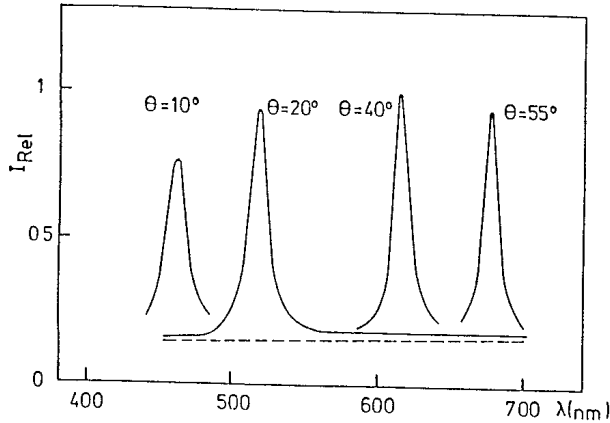
Fig. 6.13. The relative photocurrent (I_{Rel}) of the MIS junction Al (250 Å)-SiO$_2$-p-Si at different λ for various take-off angles (both are joined by the dispersion relation). The light intensity has been kept constant. The dashed line is observed with s-polarized light. Grating parameters: $a = 3640$ Å, $h = 80$ Å. From [6.18]

Light Emission from SPs Excited on Gratings by Electrons

If electrons hit a metallic surface, SPs are excited, see Fig. 2.3. This happens on a smooth surface too, since − in contrast to photons − the transferred momentum is sufficient to fulfill the dispersion relation of the SPs.

If the surface has periodic perturbations, e.g., a grating profile, the SPs interact with the grating and exchange multiples of the vector $g = 2\pi/a$. Those wave vectors $k_x^0 \pm \nu g$, where ν are integer numbers, $k_x^0 = (\omega/c)(\varepsilon_1/\varepsilon_1 + 1)^{1/2}$, which fall inside the light cone, give rise to strong p-polarized light maxima [6.22]. Figure 6.14 demonstrates these beams for different wavelengths, which are selected with a monochromator together with a polarizer and a photomultiplier. The silver grating has the parameters $a = 8850$ Å and $h = 500$ Å. The evaluation of Fig. 6.14 is shown in Fig. 6.15 and displays the periodic structure of the SP dispersion produced by multiple scattering processes. The accuracy
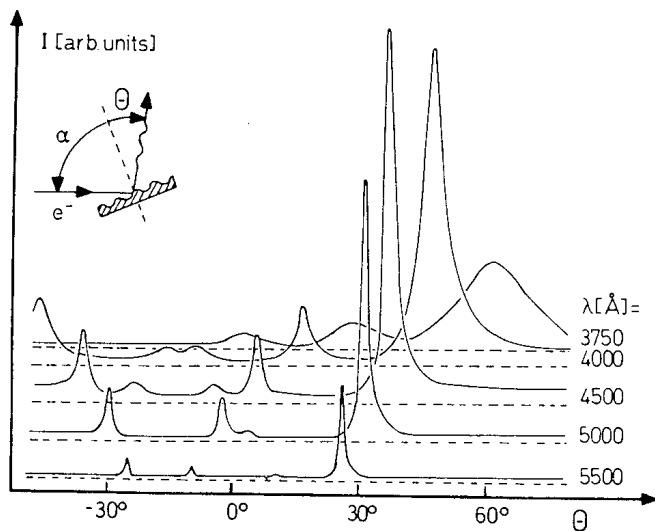
Fig. 6.14. Light of various wavelengths emitted from a sinusoidal grating ($a = 8850$ Å, $h = \sim500$ Å) which is irradiated with 80 KeV electrons at an angle of incidence of $\alpha = 70°$. From [6.22]
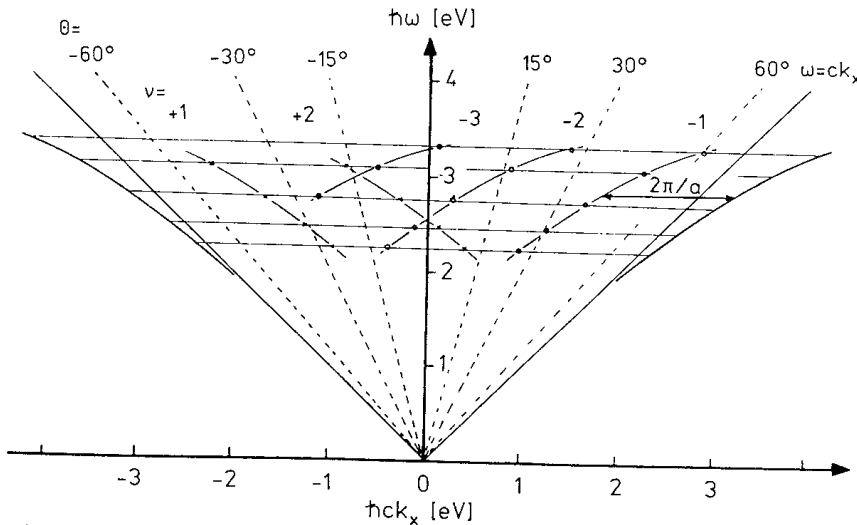
Fig. 6.15. $\omega - k_x$ diagram with the peak positions of Fig. 6.14 inserted. At a given $\hbar\omega$ of the SP, excitations occur at $k_x = k_x^0 \pm \nu g$ with $g = 2\pi/a$. The number of scattering processes is given by ν. From [6.22]

of the measurements allows detection of the position displacement of the light maxima as well as the increase of its width with increasing amplitude h of the sinusoidal grating, as has been described in Sect. 6.2. Both results agree. The difficulties and limitations in the electron experiments, in spite of many efforts, cannot reach the same accuracy as in the optical experiments.

6.4 Influence of a Second Harmonic in the Grating Profile

Since the photoresist has a nonlinear response characteristic, the sinusoidal grating profile can have contributions of higher harmonics. These can be varied by preexposing the resist uniformly. The amplitude $h^{(2)}$ of the second harmonic is measured by the intensity of the diffraction maximum $n = 2$ of s-polarized light as just described. Figure 6.16 shows the shape of the (-1)-order reflection with $h^{(2)}/h^{(1)}$ as parameter. The resonance minimum is nearly symmetric for small $h^{(2)}/h^{(1)} = 0.06$ and gets more asymmetric the larger the value of $h^{(2)}/h^{(1)}$. A maximum is formed; in addition a displacement of the minimum occurs. This result has been found at silver [6.23] as well as at gold gratings [6.9]. These results give a hint for an understanding of the observations with p-polarized light at silver gratings of different amplitudes h [6.19]. At values of h below about $700\,\text{Å}$ the intensity minimum in the resonance case at $n = 0$ remains a minimum nearly independent of h; the higher orders $n > 0$ however assume different shapes with increasing h, either a minimum or a maximum or an oscillator-like curve. These changes are due to the influence of higher harmonics which results from the production of gratings with large h values and to which the $n > 0$ orders are sensitive as just described. This is supported by the following example: Figure 6.17 [6.17] shows the shape of the reflection
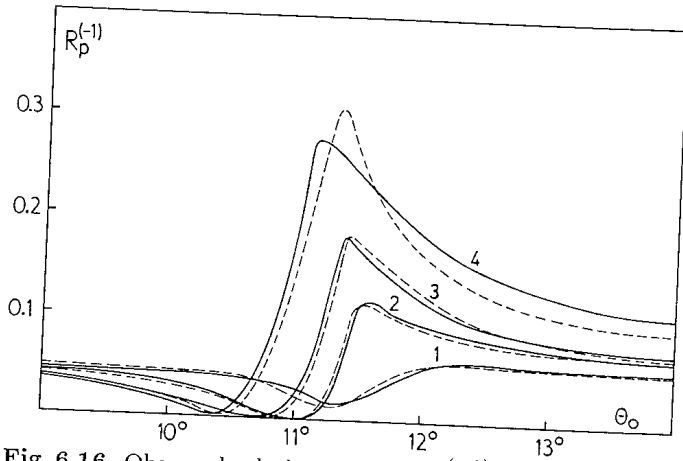
105

Fig. 6.16. Observed relative intensity $R_p^{(-1)}$ (——) of the $n = -1$ diffraction as a function of θ_0 at a grating with the profile $S(x) = h^{(1)} \cos (2\pi/a)x + h^{(2)} \cos (4\pi/a)x$. $a = 6000$ Å, $\lambda = 5145$ Å, $h^{(1)} = 150$ Å. Parameter: $h^{(2)}/h^{(1)} = 0.05$ *(1)*; $= -0.11$ *(2)*; $= -0.16$ *(3)*; $= -0.26$ *(4)*. Calculated curve: (- - -). The silver film had a thickness of 2000 Å. From [6.23]

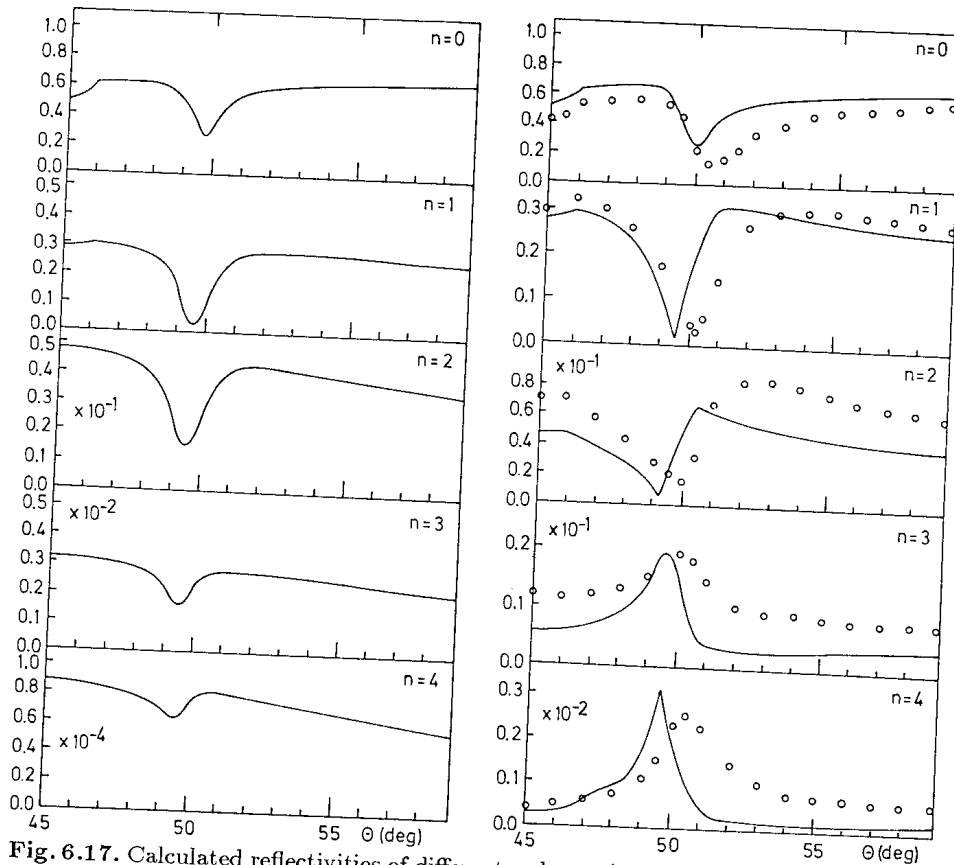**Fig. 6.17.** Calculated reflectivities of different orders n (——) at a silver grating of $h = 700$ Å. The left curves are calculated with a sinusoidal profile, the right ones are modified by adding a second harmonic component of $h^{(2)} = -84$ Å; $a = 20\,140$ Å and $\lambda = 5682$ Å. Open circles are observed data. From [6.16,17]

106

minima at different orders, $n = 0$ up to $n = 4$, at a grating with $h = 700$ Å; the other parameters are the same as in Fig. 6.11. The full lines (left) are calculated values, whereas the observed data are given by open circles. The shape of $n = 0$ − apart from a slight difference of the positions of the minima − is rather well reproduced. For $n > 2$ the discrepancies between calculated and observed curves are important, since maxima are observed instead of the calculated minima. If one recalculates the curves by adding a second harmonic $h^{(2)} = -84$ Å, the full lines at right are obtained. A rather good agreement can be noticed. Such a contribution of $h^{(2)}$ can arise during the preparation of the grating as we have seen in the example of Fig. 6.17.

In this context it shall be mentioned that in earlier experiments on (ruled) gratings of Al and Au the resonance positions are observed as peaks of intensities and not as intensity minima [6.24]; this observation can be explained similarly by the contribution of the higher orders in the grating profile.

6.5 Resonance Enhancement of the Electromagnetic Field

Theoretical Considerations

As we have seen in Sect. 2.4 the intensity of the electromagnetic field in the interface silver/air (at the air side) passes a maximum if resonance (zero reflectivity) is reached. This enhancement can be calculated for smooth surfaces using Fresnel's relations and has been experimentally confirmed at surfaces of small roughness. Such an enhancement exists on sinusoidal surfaces also and has been estimated using energy conservation in the same way as mentioned above, see Sect. 2.4, with the result [2.23]

$$T^{\text{el}} = \frac{2|\varepsilon_1'|^2 \cos\theta_0 \cdot (1 - R)}{\varepsilon_1''(|\varepsilon_1'| - 1)^{1/2}} \cdot \tag{6.5}$$

$\cos\theta_0$ can be derived from (2.13):

$$\sin\theta_0 = \left(\frac{\varepsilon_1'}{\varepsilon_1' + 1}\right)^{1/2} - \frac{\lambda}{a} \cdot$$

The maximum of T^{el} is given by $R = 0$, see (2.16) and (2.14). We obtain for a grating with $a = 8000$ Å and $\lambda = 6200$ Å ($\hbar\omega = 2\,\text{eV}$) a value of ~ 250 (Ag), ~ 60 (Au), ~ 35 (Cu). The dependence on $\varepsilon_1'(\omega)$ shows the strong influence of the wavelength: the value of 250 (Ag) at $\lambda = 6500$ Å decreases to 80 at $\lambda = 4200$ Å. More details can be seen in Fig. 2 of [2.23]. These values are somewhat larger than those obtained at smooth surfaces, if T^{el} is referred to air $\varepsilon_2 = 1$, see (2.30), so that $T^{\text{el}}_{\text{max}} = |t_{012}^p|^2$.

These data of enhancement on gratings due to SPs are maximum values to be expected. The advantage of (6.5) is that it gives a quick overview of the influence of the different parameters. The field enhancement varies by a factor

of more than 10 along a saw-tooth profile. Probably due to interference effects, its maximum value does not lie at the peak of the profile.

Further the calculations are applied to sinusoidal bigratings and to a bi-grating formed by a square lattice of hemiellipsoids on planar surfaces [6.25]. Especially the enhancement has been calculated as a function of the incident angle, it passes through a maximum if the reflectivity reaches its minium (zero) at the resonance angle. The values of the enhancement are comparable to those of a sinusoidal grating.

Calculations with the extinction theorem on the enhancement at sinusoidal and saw-tooth profiles of silver, gold and copper have been published. They demonstrate that the enhancement on sinusoidal and saw-tooth profiles are comparable [6.26].

In addition, this method has been applied to compute the attenuation and dispersion of SPs on sinusoidal and saw-tooth gratings. For detailed results see [6.27].

In Sect. 6.3 we have seen by direct comparison that a quantitative agreement of calculated and measured data exists and that the observed structure of the reflectivity at sinus-like gratings and its dependence on the grating parameters are obtained if the effective extinction theorem is applied. A first order approximation does not lead to these results. Such an approximation yields too large enhancements, if one exceeds the limits of the approximation (small h/a), see [6.28].

It is noteworthy that the enhancement values T^{el}_{max} from (6.5) agree rather well with the computer simulations on sinusoidal gratings, that use the extinction theorem. For example, the value of T^{el}_{max} for a Ag grating with $a = 6015$ Å and $\lambda = 5145$ Å, see Fig. 1 of [6.16], amounts to $T^{el} = 230$, the same value results as well from (6.5). The enhancement T^{el} of the Au grating, see Fig. 1 of [6.16] calculated with (6.5) is ≈ 60, using the ε-values $(-9.7; 1.1)$. This number is equal to the one due to the extinction theorem $(T_{el} = 59)$ using the same ε-values.

Experimental Results

There are a number of publications which can be used to compare these theortical data:

a) The good agreement of the calculated scattered light intensity $(1/I_0)$ $(dI/d\Omega)$ as function of h^2 (h amplitude of the grating) discussed in Sect. 6.2 shows that the enhancement factor $|t^p_{012}|^2$ introduced by Kretschmann into the expression for the intensity from rough surfaces, describes the results fairly well [6.4]. One concludes that the enhancement amounts to a value of about 80 under the referred conditions.

b) Another result has been derived from the enhancement of the Raman scattering (SERS) [4.34]: In order to measure the field increase, the grating (silver, $a = 4507$ Å, $2h = 326$ Å) has been covered with a thin polystyrene film 100 Å thick. The surface has been irradiated with light of 6328 Å and the intensity of the Raman line (1000 cm^{-1}) at resonance

is compared to the intensity out of SP resonance. A value of about 30 is obtained, which the authors correct to 80–100 due to the presence of the polystyrene film.

c) A similar method has been used in which the silver grating is doped with nitrobenzoic acid. The intensity quotient of the Raman line $1600\,\mathrm{cm^{-1}}$ in and out of resonance has been determined to be about 25–30 [6.29, 30].

Calculations of the enhancement at sinusoidal gratings have been performed using a special approach in order to be compared to the results of (b) and (c). The results obtained agree rather well with the calculated figures reported above [6.31].

Summarizing the results, we can say that the enhancement factors of these extended SPs confirm the assumptions. A better agreement would be more satisfying. But nowadays these low T^{el} values are not attractive compared to the high values of T^{el} of 10^4–10^7, obtained with localized SPs, see Chaps. 4, 5, which are of special interest for applications.

6.6 Second Harmonic Generation on Gratings

The excitation of SPs produces a strong enhancement of the electric field in the surface. Similar to the situation on smooth surfaces, see Sect. 2.8, the generation of second harmonics in these enhanced fields is also expected.

Experiments have been published on silver (interference) gratings ($a = 5500\,\text{Å}$) of different amplitudes h, at which laser light ($\lambda = 10.6\,\mu$) is reflected [6.28]. The scheme of the experimental device is shown in Fig. 6.18. One expects contributions of the second harmonic intensity at resonance in the direction of the diffraction maxima of the zeroth and ± first order of the ω light. If there were a dispersive medium on the silver grating, the two beams with the frequencies ω and 2ω would have different directions similar to those in the ATR device, Fig. 2.30. Since the grating of Fig. 6.18 is located in air, the conservation of momentum and energy $2(\hbar\omega/c)\sin\theta_2$ gives $\theta_1 = \theta_2$. In order to suppress the
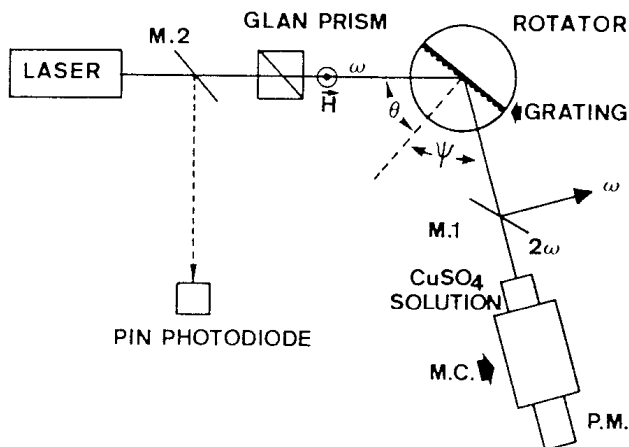
Fig. 6.18. Scheme of the experimental arrangement to measure the second harmonic signal in the light beam reflected at a grating. From [6.28]
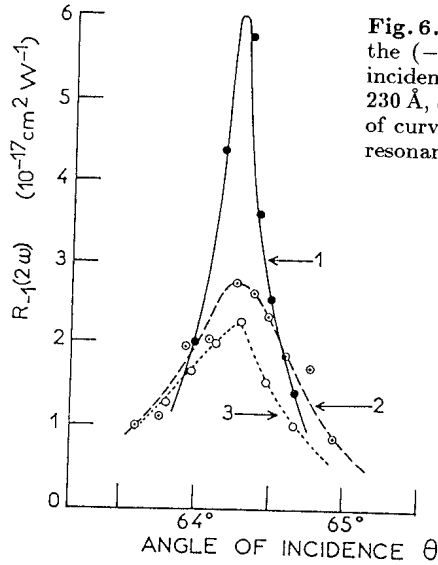
Fig. 6.19. The second harmonic intensity $R^{(-1)}(2\omega)$ in the (-1)st diffraction order as function of the angle of incidence at different amplitudes h of the grating: (1) 230 Å, (2) 350 Å, (3) 460 Å. One notices that the half width of curve (1) of 0.5° corresponds to the half width of the resonance of the fundamental frequency ω. From [6.28]

ω frequency, a filter ($CuSO_4$ solution) together with the monochromator (MC) are located before the photomultiplier. The result is displayed in Fig. 6.19 for the $R^{(-1)}(2\omega)$ as well as for the $R^0(2\omega)$ reflectivity as a function of the angle of incidence θ_0 at different heights h of the grating. One observes a resonance behavior as a function of θ_0 which shows a maximum of the 2ω intensity at the critical amplitude h_c. Here the fundamental SP excitation has its strongest value or the ATR minimum its lowest value. The observed values of h_c are 250 Å for $R^0(2\omega)$ and 300 Å for $R^{-1}(2\omega)$; both values should be equal, but it seems that measurements with smaller steps of h between 250 and 300 Å lead to the same value.

The enhancement of the second harmonic comes out as 15 for $R^0(2\omega)$ and 36 for $R^{-1}(2\omega)$ if the peak heights are compared to those obtained at a flat surface. Calculations lead to values of 5 and 11.5, respectively [6.32]. Perturbation calculations up to the second order of h/λ demonstrate strong peaks at those angles of incidence at which the maximum excitation of the fundamental SP occurs. The relative enhancement can be regarded as roughly in agreement with the observed values [6.33].

6.7 Coupling of Surface Plasmons Via Roughness

In Fig. 6.7, the effect of a grating on SPs has been described. A new situation appears if the SPs are scattered by the grating so that the scattered SPs (κ') together with the original SPs (κ) fulfill the reflection condition, see Fig. 6.20

$$\kappa - \kappa' = g \qquad \text{with} \tag{6.6}$$

$$|\kappa| = |\kappa'| \quad .$$

110
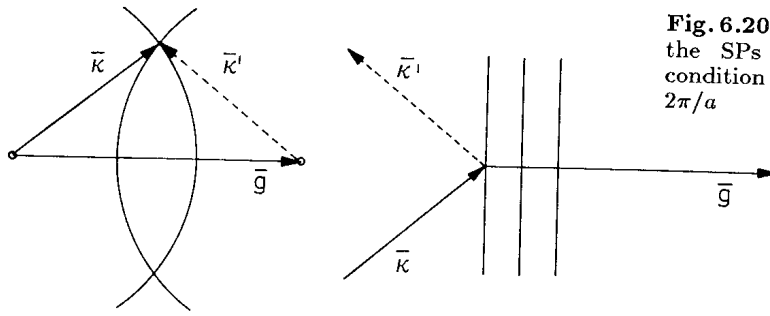
Fig. 6.20. The wave vectors of the SPs fulfill the reflection condition $\kappa - \kappa' = g$ with $|g| = 2\pi/a$

This gives

$$k_g = \tfrac{1}{2}g\nu \ ,$$ (6.7)

ν integers with k_g the projection of κ in the g direction.

If g lies in the x direction, we have

$$k_x = \pm\nu\frac{\pi}{a} \ ,$$ (6.8)

the SP suffers an Umklapp process and standing waves arise which produce an energy gap, as is well known in wave physics; the frequency becomes complex and SPs do not propagate. The dispersion relation has discontinuities at k_x given by (6.8) as Fig. 6.21a demonstrates.

Measurements with p-polarized light of varying wavelengths reflected at a commercial grating of gold and aluminum display these discontinuities at the (ω, k_x) values characterized by (6.8), see Fig. 6.21b; s-polarized light shows no anomalies [6.34].

Experiments with holographic (interference) gratings ($a = 6080\,\text{Å}$) of sinusoidal profiles have been performed to study the splitting, using the ATR device [6.35]. Here the observations were made in the plane of incidence also, but the vectors κ and g are no longer parallel, see Fig. 6.22. The angles α and θ_0 can be varied to determine the maximum excitation, both at constant ω. The detection of the excitation is measured by the light scattered from the statistical roughness on the grating, which is maximum if the excitation of the SPs is strongest. The results [6.35] are displayed in Fig. 6.23a. The half width is to be seen in Figs. 6.23b, 6.24; at the crossing point the half widths are nearly equal. If one follows the intensity on the dispersion circle SP (κ) which is primarily excited by the incoming light, the decrease of intensity near the gap is remarkable, see Fig. 6.24. The circle SP ($\kappa + g$) is weaker in general since it is excited indirectly by coupling with the g vector.

If the splitting δk of Fig. 6.23, is plotted as a function of the modulation height h, the coupling parameter, a nearly linear correlation is obtained up to h/a of about 0.14 as Table 6.1 demonstrates for $\lambda = 6328\,\text{Å}$ and $a = 6080\,\text{Å}$. Calculation of the splitting on sinusoidal gratings and saw-tooth profiles, using the extinction theorem, have been performed especially in the nonretarded
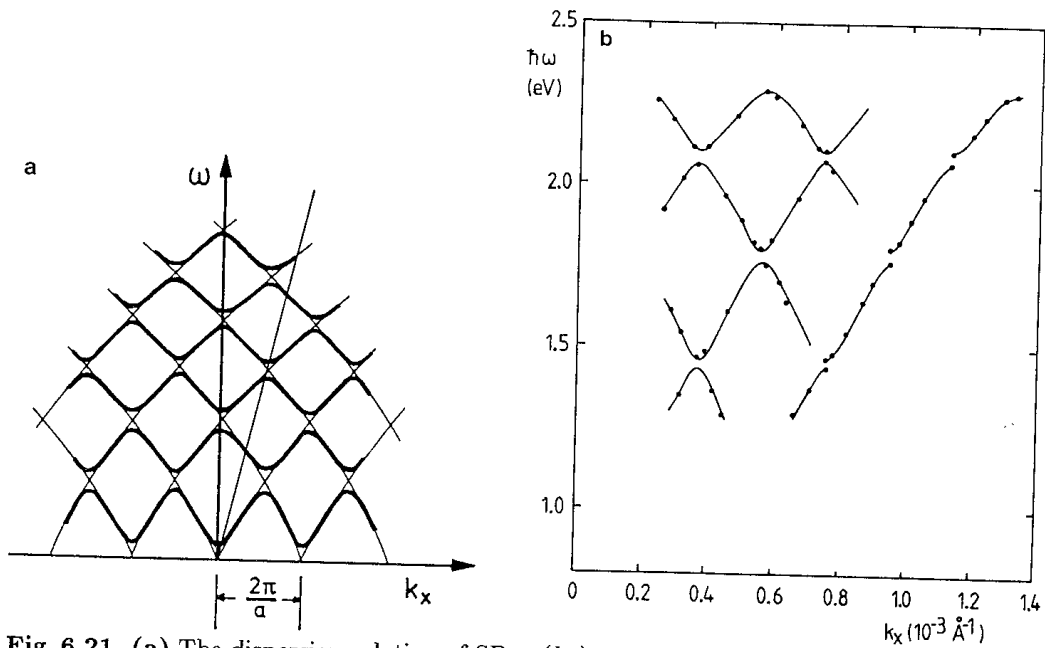
Fig. 6.21. (a) The dispersion relation of SPs $\omega(k_x)$ propagating on a grating splits at those k_x values where two branches cross each other. The straight line in the (ω, k_x) plane fixes an angle θ in real space on which the dispersion relation is fulfilled. For example, splitting can be observed when scanning the frequency ω at a given θ. (b) Observed dispersion relation of SPs on a gold grating. Commercial grating, ruled. At left of the figure the structure of Fig. 6.21a can be recognized; it demonstrates the periodic repetition in the extended Brillouin Zone. At right the branch (ω, k_x) as shown in Fig. 2.2 is split if the Bragg condition is fulfilled. From [6.34]
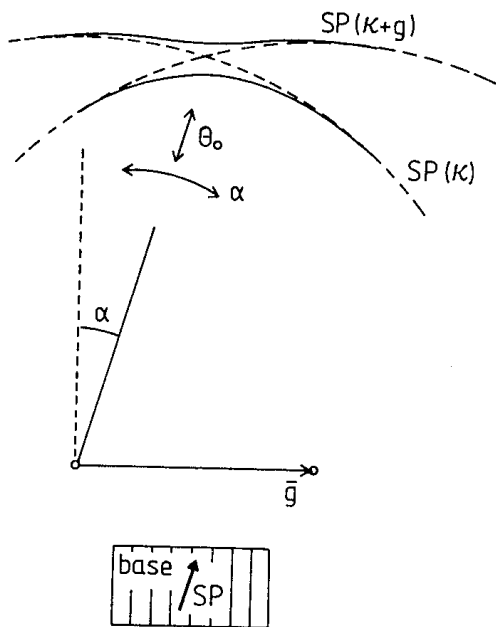
Fig. 6.22. Device to measure the surroundings of the crossing point of the two dispersion circles κ and $\kappa + g$ varying α and θ_0 : The quadrangle represents the grating sticking to the base of the ATR prism

112
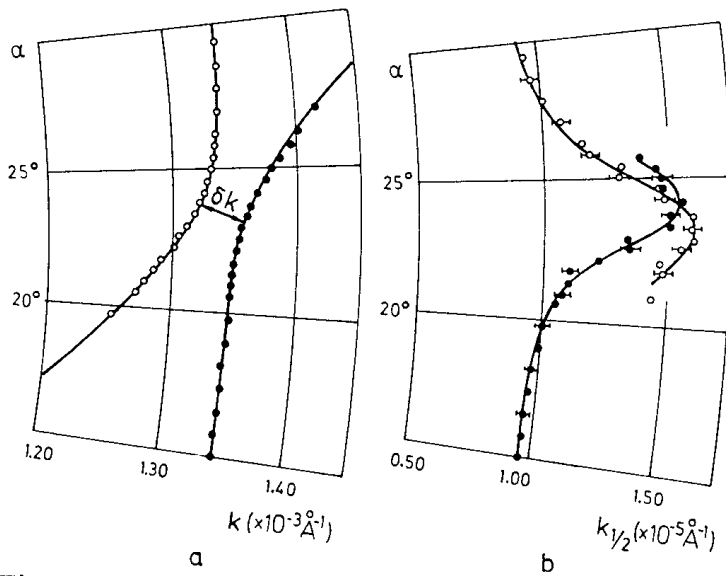
Fig. 6.23a,b. Experimental results of the coupling of two SPs via the reciprocal vector $g = 2\pi/a$. **(a)** the resonance positions $k = |\kappa|$ (•••) and $k = |\kappa + g|$ (ooo) and the halfwidths $k_{1/2}$ of the resonance as a function of the angle α between g and κ; $\alpha = 0$ means $g \| \kappa$. $\lambda = 6328\,\text{Å}$, $a = 6080\,\text{Å}$, and $h = 185\,\text{Å}$. From [6.35]
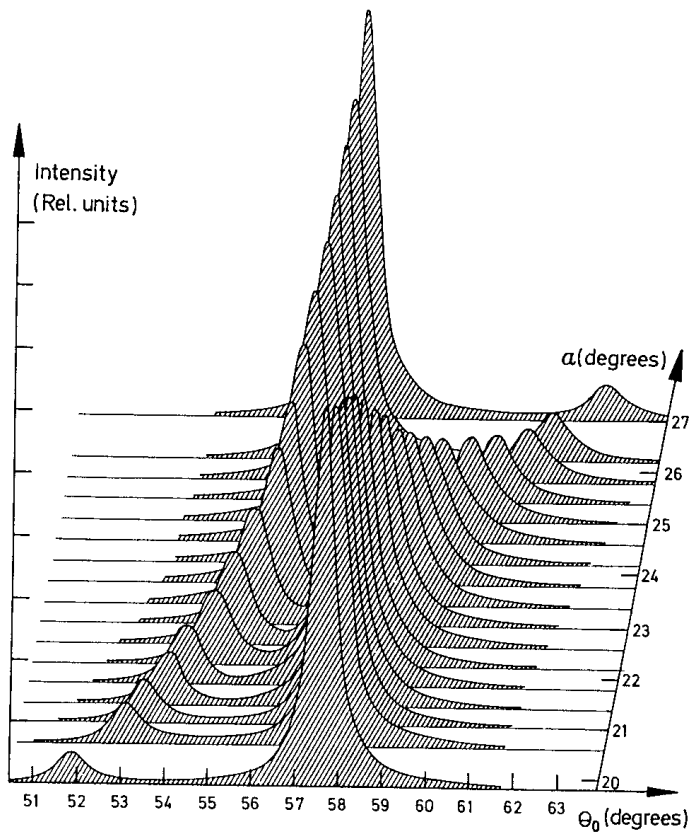
Fig. 6.24. The intensity of the two coupled SPs as a function of the angle α near the gap. θ_0 is the angle of incidence. From [6.35]

113

Table 6.1. Coupling strength measured by δk as function of the amplitude h [6.35]

| h [Å]	δk [$\times 10^{-4}$ Å^{-1}]
200	0.4
400	0.8
600	1.1
800	1.4

region [6.36]. (A calculation in the retarded region which is accessible to experiments would have allowed a comparison with these observed values). The calculations confirm the experimental results of Table 6.1 in so far as they also give in general a linear splitting δk with increasing h/a up to 0.2.

Experiments of the same type have been performed on two crossed gratings (angle 60°). Under special conditions three circles can meet in one point which leads to a pattern with three branches see Fig. 6.25 [6.37].

In the cases just described the coupling via the grating occurs *in* the silver grating/air interface. Besides this coupling there is also a coupling *through* the metal film. Surface plasmons cannot be excited on a smooth quartz/metal interface by light having passed the half cylinder (ε_0), since the dispersion relation of the SPs in these interfaces lies right of the light lines c/n, where n is the refractive index of the photoresist or quartz ($n = 1.6$, $n = 1.5$, respectively); ω_s is depressed to $\omega_s[1 + n^2(\text{quartz})]^{-1/2}$. If, however, this interface has a sinusoidal profile, its dispersion relation can be displaced in the reduced Brillouin zone, so that crossing of both dispersion relations takes place; both modes are thus coupled through the thin silver film of 600 Å thickness, so that a splitting can be observed [6.38], see Fig. 6.26.
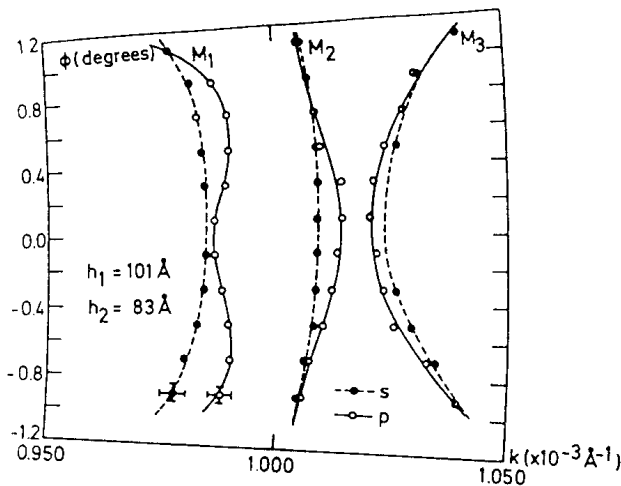
Fig. 6.25. Splitting at a crossing point of three dispersion circles produced by a sinusoidal bigrating (angle of 60°) of amplitudes h_1 and h_2 for p- and s-polarized scattered light. From [6.37]
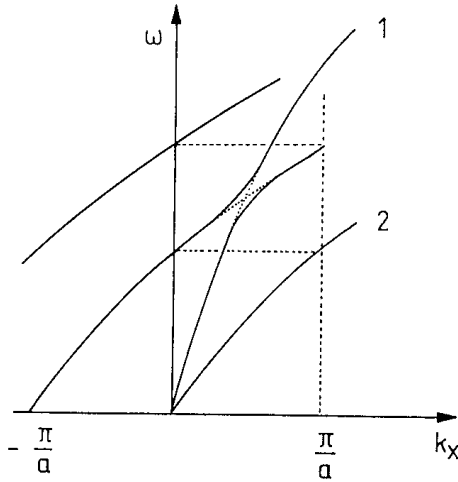
Fig. 6.26. The branches of the dispersion curves *(1)* and *(2)* of the SPs of the two surfaces of the silver film in e.g., an ATR device. In general both SPs cannot couple. If the surface has a sinusoidal profile, curve (2) can be displaced into the reduced Brillouin zone, so that they cross and a gap is observed. The coupling occurs *through* the thin silver film. From [6.38]

Crossing in Wave Guides

As we have seen in Sect. 2.6, guided light modes can be excited in the device Fig. 2.14. Figure 6.27 displays the behavior of the TM mode as a function of α, the angle between the wave vector κ and g, the reciprocal lattice vector. Rotating the lattice, see Fig. 6.22, a splitting at certain α values is observed due to the coupling of different modes via the grating. The position in which the horizontal line in Fig. 6.27 splits, one branch up, the other down, happens when two circles in k space at $\omega = $ constant cross each other, see also Fig. 6.21 or 6.23, e.g., the crossing of the circles of the dispersion of the TM_1 (κ) mode with the TM_1 $(\kappa + g)$ $(= TM_1^I)$ mode. It is also possible that the TM_1 mode couples via g with the $TE^I{}_0$ mode, since the crossing point of TM_1 (κ) and $TE_0(k + g)$ splits up.

Further, it is of interest, that the excitation maxima – neglecting the splitting at special angles α – do not change the excitation angle θ_0 in Fig. 6.27,
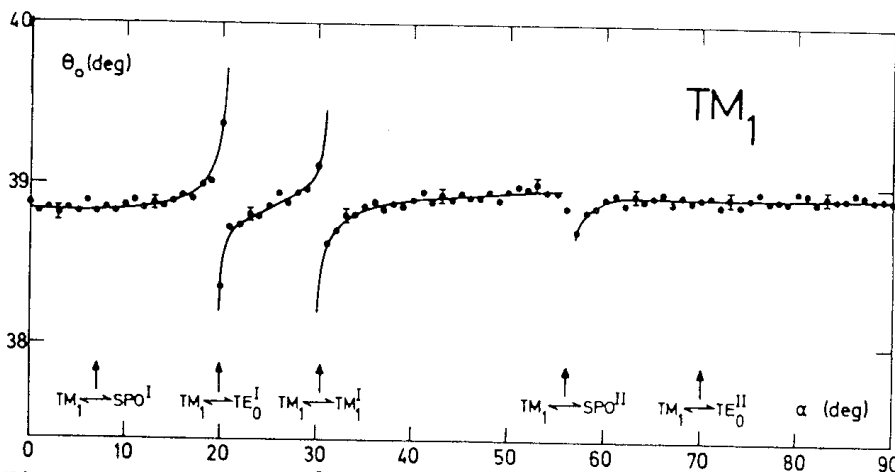
Fig. 6.27. A LiF film, 4000 Å thick, is deposited on a grating with $a = 6080$ Å and $h = 330$ Å. The planar guided light mode TM_1 is excited at θ_0. If this layer system is rotated by the angle α, see Fig. 6.22, θ_0 is registered as function of α. From [6.2]

115

$\theta_0 = 38.8°$, between $\alpha = 0°$ and $\alpha = 90°$. This means that the sinusoidal perturbation has no influence on the resonance angle θ_0. (This is in contrast to the behavior of the TM$_0$ mode which is displaced at an amplitude of $h = 300\,\text{Å}$ by about $1/2$ degree, see Fig. 6.7). This observation is in agreement with the result that a rough interface air/LiF does not influence the position of the light modes within the error of measurements, due to the fact that the planar guided modes have their field maximum in the interior of the material, further away from the surface.

Splitting of the Dispersion Relation on Rough Surfaces

Reflectivity measurements on potassium revealed a small splitting of $0.2\,\text{eV}$ of the $2.8\,\text{eV}$ SP [6.39]. The same value has been obtained on sodium [6.40]. A similar effect is reported from reflectivity measurements on silver roughened in an electrochemical cell [6.41]. Further experiments demonstrate this splitting in the emission spectra of potassium films which are irradiated with electrons of $1.5\,\text{KeV}$ at an angle of $35°$ [6.41]. It has been proposed that this splitting is due to the presence of high wave vector components in the roughness spectrum of the surface [6.42], see also [6.43, p. 501]. Since the frequency of the SPs lies near ω_s, we are in the horizontal or nonretarded region of the dispersion relation. A large wave vector in this region couples via roughness with all the wave vectors of different (k_x, k_y) around it, which have the same frequency and produce a frequency splitting proportional to the amplitude of the Fourier component of the roughness spectrum at which they are reflected, see Table 3.2. If one develops the function $|s|^2$ into delta functions and assumes that one (or some) of these functions have a higher amplitude than the others, the calculation yields reasonable results. Such a bump in the spectrum perhaps due to many crystals of equal dimensions, produced by special experimental conditions, may exist, but this question must remain open, since we have no access to this k_x region for the moment.

7. Conclusion

This review of experimental and theoretical work on the interaction of SPs with corrugated surfaces, which contains numerous interesting phenomena, has the intention of discussing the consistency of the material and discrepancies which demand reconsideration of the data. It is the hope that this review may induce experiments and calculations to clear up unanswered questions to settle the application of light scattering methods and to seek new viewpoints.

There is a rather good insight into the properties of the SPs concerning field enhancement, light emission from perturbated surfaces in the linear approximation. But since the limits of the validity of the first-order calculations are rather low, about $20\,\text{Å}$ for δ of the statistical roughness and about $70\,\text{Å}$ for the amplitudes h of a sinusoidal profile, many experiments or calculations use roughness beyond these limits. It is therefore important to have a better insight as to the dependences of the enhancement, the light emission, and the dispersion relation on δ or h, above the linear approximation. The first steps are complete, but it needs much more reliable experimental data, to get a thorough understanding of the subject.

Appendix

I) Derivation of the Dispersion Relation of SPs on a Surface of a Semi-Infinite Solid

The layer system, Fig. A.1, see also Fig. 2.1, has an interface (1/2), e.g., metal $(\varepsilon_1)|$air (ε_2), on which a p-polarized wave propagates in the x direction. There is no y dependence. We describe the fields in the media (1) and (2) as follows:

$$z>0 \quad \begin{aligned} \boldsymbol{H}_2 &= (0, H_{y2}, 0)\exp i(k_{x2}x + k_{z2}z - \omega t) \\ \boldsymbol{E}_2 &= (E_{x2}, 0, E_{z2})\exp i(k_{x2}x + k_{z2}z - \omega t) \end{aligned} \tag{A.1}$$

$$z<0 \quad \begin{aligned} \boldsymbol{H}_1 &= (0, H_{y1}, 0)\exp i(k_{x1}x - k_{z1}z - \omega t) \\ \boldsymbol{E}_1 &= (E_{x1}, 0, E_{z1})\exp i(k_{x1}x - k_{z1}z - \omega t) \ . \end{aligned} \tag{A.2}$$

These fields have to fulfill Maxwell's equations:

$$\mathrm{rot}\,\boldsymbol{H}_i = \varepsilon_i \frac{1}{c}\frac{\partial}{\partial t}\boldsymbol{E}_i \tag{A.3}$$

$$\mathrm{rot}\,\boldsymbol{E}_i = -\frac{1}{c}\frac{\partial \boldsymbol{H}_i}{\partial t} \tag{A.4}$$

$$\mathrm{div}\,\varepsilon_i \boldsymbol{E}_i = 0 \tag{A.5}$$

$$\mathrm{div}\,\boldsymbol{H}_i = 0 \ , \tag{A.6}$$

together with the continuity relations

$$E_{x1} = E_{x2} \tag{A.7}$$

$$H_{y1} = H_{y2} \tag{A.8}$$

$$\varepsilon_1 E_{z1} = \varepsilon_2 E_{z2} \ . \tag{A.9}$$

From (A.7,8) follows the continuity of

118

$$k_{x1} = k_{x2} = k_x \ . \tag{A.10}$$

Equation (A.3) gives

$$\frac{\partial H_{yi}}{\partial z} = -\varepsilon_i E_{xi} \frac{\omega}{c} \quad \text{or}$$

$$+k_{z1} H_{y1} = +\frac{\omega}{c} \varepsilon_1 E_{x1}$$

$$+k_{z2} H_{y2} = -\frac{\omega}{c} \varepsilon_2 E_{x2} \ . \tag{A.11}$$

Equation (A.11) together with (A.7,8) yield

$$H_{y1} - H_{y2} = 0$$

$$\frac{k_{z1}}{\varepsilon_1} H_{y1} + \frac{k_{z2}}{\varepsilon_2} H_{y2} = 0 \ . \tag{A.12}$$

To obtain a solution, the determinant D_0 has to be zero

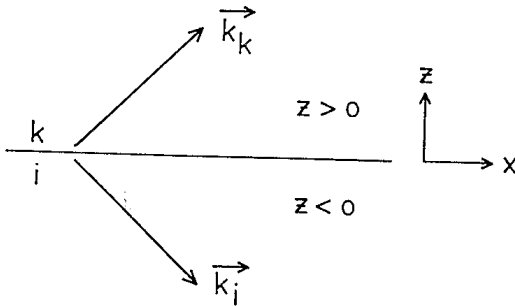$$D_0 = \frac{k_{z1}}{\varepsilon_1} + \frac{k_{z2}}{\varepsilon_2} = 0 \ . \tag{A.13}$$

This is the dispersion relation of the SPs in the system Fig. A.1. Further we get from (A.3,4,11)

$$k_x^2 + k_{zi}^2 = \varepsilon_i \left(\frac{\omega}{c} \right)^2 \ . \tag{A.14}$$

From (A.13) together with (A.14) follows

$$k_x = \frac{\omega}{c} \left(\frac{\varepsilon_1 \varepsilon_2}{\varepsilon_1 + \varepsilon_2} \right)^{1/2} \ . \tag{A.15}$$

Let us assume for the medium $\varepsilon_2 = 1$ (air) and for the medium ε_1 (metal) $\varepsilon_1 < 0$, $|\varepsilon_1| > 1$, then $k_x > \omega/c$ and k_{zi} becomes imaginary or complex. The fields have

Fig. A.1. Scheme of the interface between two media i and k on which the SP propagates. The wave vector k_i has the components k_x and k_{iz}, see (2.3)

their maxima in the surface $z = 0$ and decay in both z directions exponentially as is characteristic for surface waves.

Equations (A.13–15) here correspond to equations (2.2–4).

II) Derivation of the Dispersion Relation for SPs on a Thin Film (d_1) with Asymmetric Environment $(\varepsilon_0|\varepsilon_1|\varepsilon_2)$, e.g., Quartz/Metal Film/Air, See Also Fig. 2.1

One way is to proceed as in Appendix I, using Maxwell's equations together with the boundary conditions at the two interfaces. It is however simpler to calculate the reflectivity of an incoming light beam at the asymmetric layer system, see Fig. A.2, and to look at a resonance of the system.

The light beam is partially reflected at the interface (0/1) and partially it transmits through the interface (0/1) and is back reflected at the interface (1/2), see Fig. A.2. The amplitudes can be calculated with Fresnel's equations for p-polarized light

$$r_{ik}^p = \left(\frac{k_{zi}}{\varepsilon_i} - \frac{k_{zk}}{\varepsilon_k}\right) \bigg/ \left(\frac{k_{zi}}{\varepsilon_i} + \frac{k_{zk}}{\varepsilon_k}\right) \quad \text{and} \quad t_{ik}^p = 1 + r_{ik}^p \tag{A.16}$$

with k_{zi} given by (A.14).

The sum of the reflected beams or the total amplitude of the reflected wave comes out as

$$r_{012} = \frac{E_r^p}{E_0^p} = \frac{r_{01} + r_{12}e^{2i\alpha}}{1 + r_{01}r_{12}e^{2i\alpha}} , \tag{A.17}$$

with $\alpha = k_{z1}d_1$ ($2i\alpha < 0$, since $\varepsilon_1 < 0$).

The zero of the denominator of (A.17) represents the dispersion relation of the layer system. It can be written in different ways:

$$1 + r_{01}^p r_{12}^p e^{2i\alpha} = 0 \quad \text{or} \tag{A.18}$$

$$\left(\frac{k_{z1}}{\varepsilon_1} + \frac{k_{z0}}{\varepsilon_0}\right)\left(\frac{k_{z2}}{\varepsilon_2} + \frac{k_{z1}}{\varepsilon_1}\right) + \left(\frac{k_{z1}}{\varepsilon_1} - \frac{k_{z0}}{\varepsilon_0}\right)\left(\frac{k_{z2}}{\varepsilon_2} - \frac{k_{z1}}{\varepsilon_1}\right)e^{2i\alpha} = 0 . \tag{A.19}$$
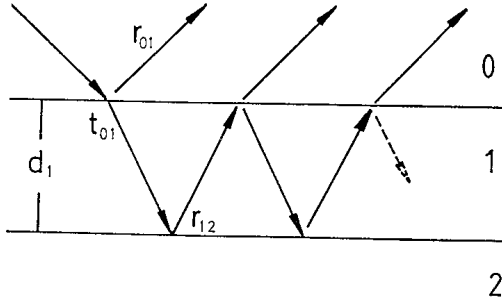

Fig. A.2. Calculation of $r_{012}^{(p)}$

120

If the two media ε_0 and ε_2 become equal, we obtain the dispersion relation of a symmetric layer system, used in (2.34,35):

$$\varepsilon_1 k_{z2} + \varepsilon_2 k_{z1} \tanh \frac{k_{z1} d_1}{2i} = 0$$

$$\varepsilon_1 k_{z2} + \varepsilon_2 k_{z1} \mathrm{ctgh} \frac{k_{z1} d_1}{2i} = 0 \ . \tag{A.20}$$

To recognize the resonance character of (A.18) and to have a better insight into the physics of this relation, we proceed as follows:

For large d_1, the above dispersion relation (A.18) transforms into the dispersion relation (A.13) with the solution $k_x' + i k_x''$ which shall be written for the moment as k_x^0. If the thickness d_1 of the metal film decreases, the medium ε_0 e.g., quartz, approaches the interface (1/2) and influences the value of k_x^0. The solution of (A.18) then becomes dependent on d_1.

The new resonance position may be called $k_x^0 + \Delta k_x$. For small Δk_x or $e^{2i\alpha} \ll 1$, k_{zi} can be developed around k_x^0 :

$$k_{zi} = \sqrt{\varepsilon_i \left(\frac{\omega}{c}\right)^2 - (k_x^0 + \Delta k_x)^2} = k_{zi}^0 - \frac{k_x^0}{k_{zi}^0} \Delta k_x \ . \tag{A.21}$$

If we use Fresnel's relations and introduce

$$r_{12}^p = z_{12}/n_{12} \ , \tag{A.22}$$

r_{012}^p can be written as

$$r_{012}^p = r_{01}^p \frac{n_{12} + z_{12}(r_{01})^{-1} e^{2i\alpha}}{n_{12} + z_{12} r_{01} e^{2i\alpha}} \ . \tag{A.23}$$

After some calculations and putting $n_{12}^0(k_x^0) = 0$, see (A.13), one obtains

$$\Delta k_x = r_{01}^p e^{2i\alpha} 2 \left(\frac{\omega}{c}\right) \left(\frac{\varepsilon_1 \varepsilon_2}{\varepsilon_1 + \varepsilon_2}\right)^{3/2} \frac{1}{\varepsilon_2 - \varepsilon_1} \quad \text{with} \tag{A.24}$$

$$r_{01}^p = \frac{a^2 - i\varepsilon_0^2}{a^2 + i\varepsilon_0^2} = \frac{a^2 - \varepsilon_0^2}{a^2 + \varepsilon_0^2} + i\frac{2a\varepsilon_0}{a^2 + \varepsilon_0^2} \tag{A.25}$$

if $k_x = k_x^0$ and with $a^2 = [-\varepsilon_1'(\varepsilon_0 - 1) - \varepsilon_0]$.

The factor of r_{01}^p can be regarded as real if $\varepsilon_1'' \ll \varepsilon_1'$. The term Δk_x is complex and we can call it $\Delta k_x^{\mathrm{rad}}$; it has a real part which displaces k_x^0 and more importantly, it has an imaginary part which causes an additional radiation damping, a consequence of the presence of the medium ε_0.

This damping is due to the radiation emitted from the SPs at the interface (1/2) back into the medium (ε_0) in the direction of the reflected beam, see

Fig. 3.11. An emission into the (ε_2) half space is forbidden in the case of a smooth surface. The new resonance position is then given by

$$k_x = k_x^0 + \Delta k_x^{\mathrm{rad}} = k_x' + \mathrm{Re}\,\{\Delta k_x^{\mathrm{rad}}\} + i k_x'' + \mathrm{Im}\,\{\Delta k_x^{\mathrm{rad}}\} \qquad (A.26)$$

or with (2.22,3)

$$k_x = k_x' + \mathrm{Re}\,\{\Delta k_x^{\mathrm{rad}}\} + i(\Gamma^{\mathrm{i}} + \Gamma^{\mathrm{rad}})\ . \qquad (A.27)$$

If $a^2 - \varepsilon_0^2 > 0$, the dispersion relation (A.18) lies to the right of the dispersion relation (A.13); it is in general small. The term Γ^{rad} however is of fundamental significance for the ATR device.

With these relations we get the expression for R, see (2.18): Using the relation (A.23,26,7), r_{012} can be written as

$$r_{012}^p = r_{01}^p \frac{k_x - (k_x' + \Delta k_x^{\mathrm{rad}}) - i(\Gamma^{\mathrm{i}} - \Gamma^{\mathrm{rad}})}{k_x - (k_x' + \Delta k_x^{\mathrm{rad}}) - i(\Gamma^{\mathrm{i}} + \Gamma^{\mathrm{rad}})}\ . \qquad (A.28)$$

It follows that

$$|r_{012}^p|^2 = |r_{01}^p|^2\, 1 - \frac{4\Gamma^{\mathrm{i}}\Gamma^{\mathrm{rad}}}{\{k_x - [k_x' + \mathrm{Re}\,\{\Delta k_x^{\mathrm{rad}}\}]\}^2 + (\Gamma_{\mathrm{i}} + \Gamma_{\mathrm{rad}})^2}\ . \qquad (A.29)$$

For the resonance case the braces $\{\ \}$ becomes zero, so that (2.18) follows; $|r_{01}^p|^2 = 1$, assumed. This is an approximation, since $\varepsilon_1'' = 0$ so that the reflection is not without loss and $|r_{01}^p|^2 < 1$.

III) Enhancement Factor

Applying the summation procedure, we calculate the field transmitted through the film d_1 into the interface (1/2) in the medium (ε_2) and obtain

$$t_{012}^p = \frac{t_{01}^p t_{12}^p e^{i\alpha}}{1 + r_{01}^p r_{12}^p e^{2i\alpha}}\ . \qquad (A.30)$$

With the same steps of calculation as above, and replacing k_{z1} in the denominator of (A.21), we get

$$t_{012}^p = 2 t_{01}^p \frac{\omega}{c} e^{i\alpha} \left(\frac{\varepsilon_1\varepsilon_2}{\varepsilon_1 + \varepsilon_2}\right)^{3/2} \frac{1}{\varepsilon_1 - \varepsilon_2} \frac{1}{k_x - (k_x^0 + \Delta k_x^{\mathrm{rad}})} \qquad \text{and} \qquad (A.31)$$

$$T = t_{012}^p{}^2 = 4\left(\frac{\omega}{c}\right)^2 |t_{01}^p|^2 e^{2i\alpha} \left(\frac{\varepsilon_1\varepsilon_2}{\varepsilon_1 + \varepsilon_2}\right)^3$$

$$\times \left(\frac{1}{\varepsilon_1 - \varepsilon_2}\right)^2 \frac{1}{|k_x - (k_x^0 + \Delta k_x^{\mathrm{rad}})|^2}\ . \qquad (A.32)$$

122

The shape of $|t^p_{012}|^2$ as a function of k_x is reproduced in Fig. 2.13. In most cases the value of T_{max} is of interest, that means the value of T at $k_x = k_x^0 + \text{Re}\{\Delta k_x^{rad}\}$. With

$$|t^p_{01}|^2_{max} = \frac{4a^4}{a^4 + \varepsilon_0^4} \, ,$$
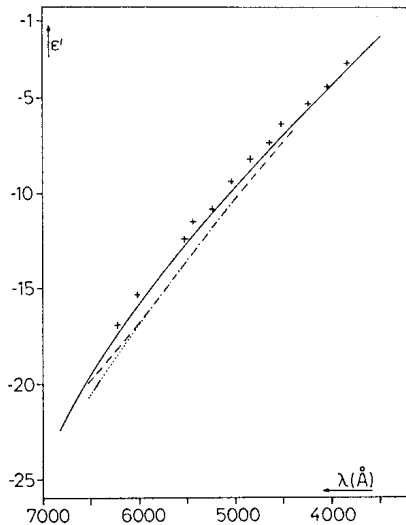
(A.24), and putting $\Gamma^i = \Gamma^{rad}$, using

$$\frac{1}{(\Gamma^i + \Gamma^{rad})^2} = \frac{1}{4\Gamma^i\Gamma^{rad}} \, , \quad \text{one gets}$$

$$T_{max} = \frac{1}{\varepsilon_0} \frac{a}{1 + |\varepsilon_1'|} \frac{2(\varepsilon_1')^2}{\varepsilon_1''} \qquad (A.33)$$

see (2.27).

IV) Collection of the Dielectric Functions of Gold and Silver

The following figures, A.3–6, and tables, A.1, 2, compare values of $\varepsilon' + i\varepsilon''$ obtained by different methods.
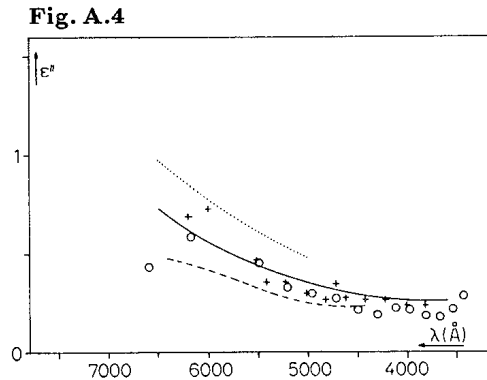

◀ Fig. A.3

Fig. A.4

Fig. A.3. ε' values of silver. (+++): measured with the ATR method. The films are vaporized at a pressure of about 6×10^{-6} Torr [A.2]. (——): derived from transmission and reflection (T_0, R_0, T_{60}^p) measurements, pressure $<4 \times 10^{-6}$ Torr [A.3]. On the same line lie a number of ATR data of other authors [A.2]. (- - -): ellipsometric measurements by reflection at surfaces of thick polycrystalline material [A.4]. (• • •): derived from transmission and reflection measurements. Pressure 5–10×10^{-7} Torr. Annealed films [A.5]

Fig. A.4. ε'' values of silver. (+++, ——): ATR method [A.2]. (ooo): (T_0, R_0, T_{60}^p) method [A.3]. (• • •): From transmission and reflection measurements [A.5]. (- - -): Ellipsometric method [A.4]

123
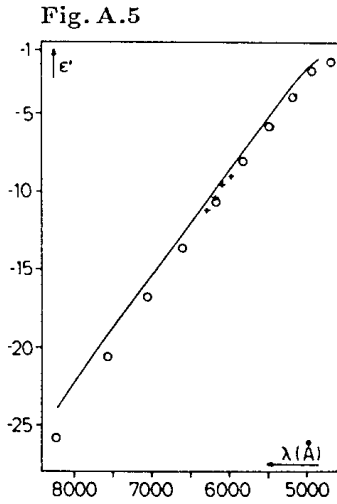
Fig. A.5. ε' data of gold films. $(+++, ---)$: ATR method [A.3]. (ooo): (T_0, R_0, T_{60}^p) method [A.3]. $(\cdot\cdot\cdot)$: From transmission and reflection measurements [A.5] and ellipsometric method [A.4]
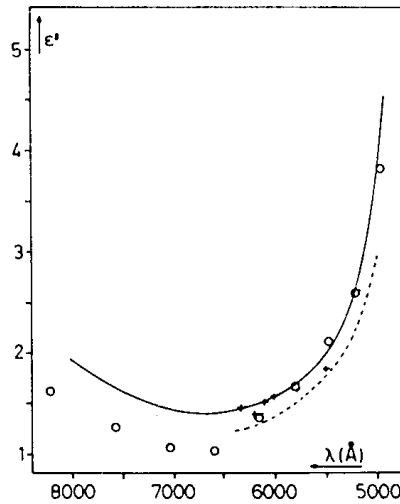
Fig. A.6. ε'' data of gold films. $(+++, ---)$: ATR method [A.2]. (ooo): (T_0, R_0, T_{60}^p) method [A.3]. $(---)$: Ellipsometric method [A.4]. $(\cdot\cdot\cdot)$: Transmission and reflection measurements [A.5]

The preceeding data of $\varepsilon(\omega)$, as far as thin films are concerned, have been obtained from measurements which differ according to the pressure under which the films are vaporized. Common to all is that the optical measurements are performed at open air.

It is therefore of interest to know which changes happen, if the preparation *and* the optical observations are made at the optimal ultrahigh vacuum conditions. Such measurements have been performed on silver by *Hincelin* with the ATR method at a pressure of $\leqslant 10^{-9}$ Torr [A.6].

Using a prism as shown in Fig. A.7 — it is half of the device in Fig. 2.8, configuration (b) — the maximum excitation of SPs on the metal/vacuum interface can be found by turning the prism in the vacuum. The reflected light returns into the direction of the incoming beam and leaves the high vacuum chamber through a window, so that the optical measurement, the registration of the ATR minimum, can be performed under UHV conditions. The determination of the dielectric function $\varepsilon(\omega)$ and the film thickness of lithium and sodium film at about 2×10^{-9} Torr was possible, *Bösenberg* [A.7].

The same procedure has been applied on silver; the data are collected in Table A.3. The values of $|\varepsilon'|$ of H and DT agree with one another. After 15 days under UHV, last column of numbers, brings the H data nearer to those of JC. The lowest values of $|\varepsilon'|$ are those of SCH whereas the highest are those of H; the data of JC lie inbetween.

The comparison for $|\varepsilon''|$ for the different methods is shown in Fig. A.8. The large values of DT come probably from the annealing of these films. The data of SCH are near to the values of H after an aging process of 15 days under UHV.

Table A.1. Dielectric function of silver. Notation:
PM ATR data [A.2]
JC T_0, R_0, T_{60}^p method (transmission and reflection measurements) [A.3]
DT transmission and reflection measurements [A.5]

λ [Å]	Real part			Imaginary part		
	PM	JC	DT	PM	JC	DT
7000	−22.4	−24.3		0.91	0.40	
6900	−21.7	−23.4		0.88	0.42	
6800	−21.0	−22.5		0.85	0.44	
6700	−20.3	−21.4		0.81	0.45	
6600	−19.7	−20.6		0.77	0.46	
6500	−19.0	−19.6	−20.6	0.74	0.47	0.97
6400	−18.3	−18.6	−19.9	0.69	0.49	0.93
6300	−17.6	−18.0	−19.2	0.67	0.50	0.89
6200	−16.9	−17.2	−18.4	0.65	0.50	0.86
6100	−16.3	−16.5	−17.6	0.62	0.50	0.82
6000	−15.6	−15.9	−16.9	0.59	0.50	0.78
5900	−14.9	−15.2	−16.2	0.55	0.49	0.74
5800	−14.3	−14.6	−15.5	0.52	0.48	0.71
5700	−13.6	−14.0	−14.8	0.49	0.47	0.68
5600	−13.0	−13.4	−14.1	0.47	0.47	0.65
5500	−12.4	−12.7	−13.5	0.45	0.46	0.62
5400	−11.8	−12.1	−12.8	0.43	0.45	0.59
5300	−11.2	−11.4	−12.2	0.41	0.42	0.56
5200	−10.6	−10.8	−11.6	0.39	0.39	0.53
5100	−10.0	−10.2	−10.9	0.38	0.37	0.51
5000	−9.4	−9.7	−10.3	0.37	0.34	0.48
4900	−8.9	−9.2		0.35	0.32	
4800	−8.4	−8.7		0.34	0.29	
4700	−7.7	−8.2		0.33	0.27	
4600	−7.2	−7.7		0.32	0.24	
4500	−6.6	−7.1		0.31	0.22	
4400	−6.1	−6.6		0.30	0.20	
4300	−5.6	−6.1		0.30	0.20	
4200	−5.1	−5.6		0.30	0.20	
4100	−4.5	−5.1		0.30	0.20	
4000	−4.0	−4.5		0.30	0.20	
3900		−3.9		0.30	0.20	
3800		−3.4		0.30	0.20	
3700		−2.8		0.31	0.22	
3600		−2.3		0.32	0.25	

Table A.2. Dielectric function of gold (see also caption to Table A.1)

λ [Å]	Real part			Imaginary part		
	PM	JC	DT	PM	JC	DT
8200	−23.8	−25.7		2.19	1.62	
8100	−23.1	−24.9		2.08	1.67	
8000	−22.3	−24.0		1.99	1.62	
7900	−21.5	−23.3		1.90	1.46	
7800	−20.7	−22.5		1.82	1.40	
7700	−20.0	−21.7		1.74	1.34	
7600	−19.3	−20.9		1.67	1.29	
7500	−18.6	−20.2		1.62	1.24	
7400	−18.0	−19.4		1.56	1.19	
7300	−17.4	−18.6		1.52	1.15	
7200	−16.7	−17.9		1.48	1.11	
7100	−16.1	−17.2		1.45	1.08	
7000	−15.4	−16.6		1.43	1.05	
6900	−14.7	−15.9		1.42	1.04	
6800	−14.1	−15.2		1.41	1.03	
6700	−13.4	−14.4		1.40	1.02	
6600	−12.7	−13.7	−15.2	1.41	1.04	1.29
6500	−12.1	−13.1	−14.3	1.42	1.08	1.29
6400	−11.4	−12.4	−13.4	1.45	1.14	1.32
6300	−10.8	−11.6	−12.8	1.47	1.20	1.36
6200	−10.1	−11.0	−12.0	1.50	1.27	1.39
6100	−9.5	−10.2	−11.2	1.54	1.35	1.41
6000	−8.9	−9.6	−10.2	1.59	1.45	1.47
5900	−8.2	−8.8	−9.6	1.65	1.55	1.55
5800	−7.5	−8.2	−8.8	1.72	1.67	1.67
5700	−6.8	−7.4	−8.1	1.80	1.80	1.72
5600	−6.1	−6.7	−7.3	1.88	1.94	1.80
5500	−5.5	−6.0	−6.5	1.98	2.09	1.91
5499	−4.7	−5.3	−5.7	2.20	2.28	2.09
5300	−3.8	−4.6	−4.8	2.44	2.49	2.25
5200	−3.2	−3.9	−4.1	2.80	2.73	2.52
5100	−2.5	−3.2	−3.2	3.26	3.12	2.93
5000	−2.0	−2.6	−2.4	4.12	3.56	3.24
4900	−1.6	−2.2		4.02		

Table A.3. ε' values of thin silver films. H *Hincelin* [A.6], SCH *Schröder* [A.2], JC *Johnson* and *Christie* [A.3], DT *Dujardin* and *Thèye* [A.5]. The last column gives the values of the film after 15 days aging under UHV conditions

| λ [μm]	H	SCH	JC	DT	
0.38	−3.62		−3.4		−3.49
0.39	−4.12				
0.40	−4.64	−4.0	−4.4		−4.58
0.41	−5.17	−4.5			
0.42	−5.70	−5.1	−5.5		
0.43	−6.25	−5.6			
0.44	−6.80	−6.1	−6.5		
0.45	−7.36	−6.6		−7.21	
0.46	−7.93	−7.2	−7.6		
0.47	−8.51	−7.7			
0.48	−9.10	−8.4	−8.7		
0.49	−9.70	−8.9			
0.50	−10.30	−9.4	−9.8	−10.30	−10.06
0.51	−10.9	−10.0		−10.9	
0.51	−11.5	−10.6	−11.0	−11.6	
0.54	−12.8	−11.8	−12.3	−12.8	
0.55	−13.5	−12.4		−13.5	−13.1
0.56	−14.1	−13.0	−13.6	−14.1	
0.57	−14.8	−13.6	14.8		
0.58	−15.5	−14.3	−14.7	−15.5	
0.59	−16.2	−14.9		−16.2	
0.60	−16.9	−15.6	−16.0	−16.9	−16.4
0.61	−17.6	−16.3		−17.6	
0.62	−18.3	−16.9	−17.3	−18.4	
0.63	−19.1	−17.6		−19.2	
0.64	−19.8	−18.3	−18.7	−19.9	
0.65	−20.6	−19.0		−20.6	−20.0
0.66	−21.3	−19.7	−20.2		
0.67	−22.1	−20.3			
0.68	−22.9	−21.0	−21.6		
0.69	−23.7	−21.7			
0.70	−24.5	−22.4	−23.1		−23.7
0.71	−25.3				
0.72	−26.1		−24.6		
0.73	−27.0				
0.74	−27.8		−26.2		
0.75	−28.7				
0.76	−29.6		−27.9		
0.77	−30.5				
0.78	−31.4		−29.4		
0.79	−32.3				
0.80	−33.2		−31.0		
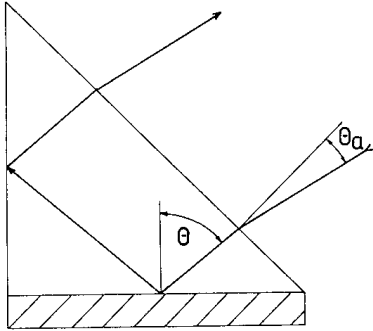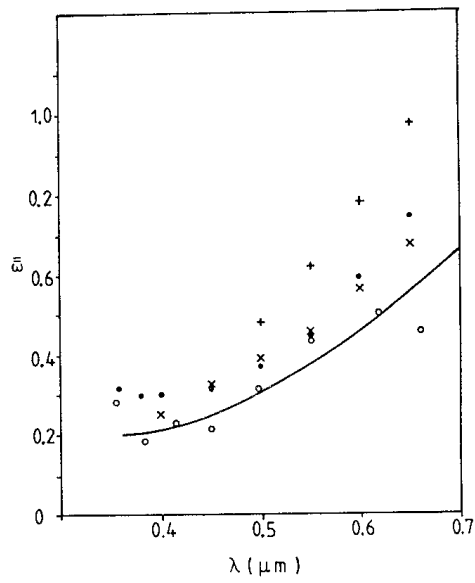
Fig. A.7. Optical device to excite SPs on the metal (hatched)/vacuum interface under UHV conditions [A.7]

Fig. A.8. Comparison of ε'' values of thin silver films obtained with different methods. (——): H [A.6]; (+++): DT [A.5]; (•••): SCH [A.2]; (ooo): JC [A.3]; (x x x) films after 15 days aging under UHV

References

Chapter 1

1.1   V.M. Agranovich, D.L. Mills (eds.): *Surface Polaritons* (North Holland, Amsterdam 1982)

Chapter 2

2.1   R.H. Ritchie: Phys. Rev. **106**, 874 (1957)
2.2   C.J. Powell, J.B. Swan: Phys. Rev. **118**, 640 (1960)
2.3a H. Raether: Physics of Thin Films **9**, 145 (1977)
2.3b H. Raether: "Excitation of Plasmons and Interband Transitions by Electrons", Springer Tracts in Modern Physics, Vol. 88 (Springer, Berlin, Heidelberg, New York 1980)
2.3c E.N. Economou, K.L. Ngai: Advances in Chemical Physics **27**, 265 (1974)
2.4   V.M. Agranovich, D.L. Mills (eds.): *Surface Polaritons* (North Holland Co., Amsterdam 1982)
2.5   A.D. Boardman (ed.): *Electromagnetic Surface Modes* (Wiley, New York 1982)
2.6   F. Forstmann, R.R. Gerhardts: *Metal Optics Near the Plasma Frequency*, Springer Tracts in Modern Physics, Vol. 109 (Springer, Berlin, Heidelberg, New York 1986)
2.7   Y. Teng, E.A. Stern: Phys. Rev. Lett. **19**, 511 (1967)
2.8   E. Kretschmann, H. Raether: Z. Naturforsch. **23a**, 2135 (1968)
2.9   R. Bruns, H. Raether: Z. Phys. **237**, 98 (1970)
2.10 A. Otto: Z. Phys. **216**, 398 (1968)
2.11 E. Kretschmann: Z. Phys. **241**, 313 (1971)
2.12 A. Otto: Z. Angew. Phys. **27**, 207 (1969)
2.13 J. Bösenberg: Phys. Lett. **A37**, 439 (1971); Z. Phys. **B22**, 261 (1975)
2.14a R. Inagaki, K. Kagami, E.T. Arakawa: Phys. Rev. **B24**, 3644 (1981); Appl. Opt. **21**, 949 (1982)
2.14b B. Rothenhäusler, J. Rabe, P. Korpium, W. Knoll: Surf. Sci. **1**, 373 (1984)
2.15a E. Kröger, H. Raether: Z. Phys. **224**, 1 (1971)
2.15b M. Bishop, A.A. Maradudin: Sol. State Comm. **12**, 1225 (1973)
2.16 A. Humbert, J.M. Debever, H. Dollaporta, J. Hanus: J. Physique Lettres **42**, L 167 (1981)
2.17 J. Schilling: Z. Phys. **B25**, 61 (1976)
2.18 E. Kretschmann: Thesis, Hamburg (1972) p. 15, 16
2.19 H. Raether: Surface Science **140**, 31 (1984)
2.20 P.B. Johnson, R.W. Christy: Phys. Rev. **B6**, 4370 (1972)
2.21 U. Schröder: Surface Sci. **102**, 118 (1981); see Appendix
2.22 G. Hincelin: Phys. Rev. **B24**, 787 (1981)
2.23 W.H. Weber, G.W. Ford: Optics Letters **6**, 122 (1981)
2.24 J. Bösenberg: Z. Phys. **B22**, 261 (1975)
2.25 W.H. Weber, S.L. McCarthy: Phys. Rev. **12**, 5643 (1975)
2.26 T.L. Haltom, E.T. Arakawa, M.W. Williams, E. Kretschmann: Appl. Optics **18**, 1233 (1979)
2.27 W.P. Chen, J.M. Chen: JOSA **71**, 189 (1981)
2.28 K. Holst, H. Raether: Opt. Comm. **2**, 312 (1970)
2.28a I. Pockrand: J. Phys. D, Appl. Phys. **9**, 2423 (1976)
2.28b J. Cowan, E.T. Arakawa: Z. Physik **235**, 97 (1970)
2.29 I. Pockrand: Surf. Science **72**, 577 (1978)
2.30 C.F. Eagan, W.H. Weber: Phys. Rev., **B19**, 5068 (1979)
2.31 D. Hornauer, H. Raether: Opt. Comm. **7**, 297 (1973)

2.32 G. Wähling: Z. Naturforsch. A33, 536 (1978)
      I. Pockrand, J.D. Swalen: JOSA 68, 1147 (1978)
2.33 G. Wähling, D. Möbius, H. Raether: Z. Naturfosch. 33a, 907, (1978);
      G. Wähling: Z. Naturforsch. 36a, 588 (1981)
2.34 I. Pockrand, J.D. Swalen, R. Santo, A. Brillante, M.R. Philpott: J. Chem. Phys. 69,
      4001 (1978)
2.34a I. Pockrand, A. Brillante, D. Möbius: J. Chem. Phys. 77, 6289 (1982)
2.35 W.R. Holland, D.G. Hall: Phys. Rev. B27, 7765 (1983)
2.36 G.S. Agarwal, S. Dutta Gupta: Phys. Rev. B32, 3607 (1985)
2.37 C. Kunz: Z. Phys. 196, 311 (1966)
2.38a P. Halevi: Phys. Rev. B12, 4032 (1975)
2.38b T. Lopez-Rios, G. Vuye: Nuovo Cimento 39b, 823 (1977)
2.38c U. Schröder: Surf. Sci. 102, 118 (1981)
2.39 P. Schmüser: Z. Phys. 180, 105 (1964)
2.40 T. Kloos: Z. Phys. 208, 77 (1968)
2.41 H. Raether: Surf. Sci. 8, 233 (1967)
2.42 R.B. Pettit, J. Silcox, R. Vincent: Phys. Rev. B11, 3116 (1975)
2.43a G.J. Kovacs, G.D. Scott: Phys. Rev. B16, 1297 (1977)
2.43b G.J. Kovacs: Thin Solid Films 60, 33 (1979); further see Chap. 4 in [2.5] "Optical
      Excitation of Surface Plasmon-Polarizations in Layered Media"
2.44 M. Fukui, V. So, R. Normandin: Phys. Status Solidi (b) 91, K61 (1979)
2.45 D. Sarid: Phys. Rev. Lett. 47, 1927 (1981)
2.46 A.E. Craig, G.A. Olson, D. Sarid: Optics Lett. 8, 380 (1983)
2.47 J.C. Quail, J.G. Rako, H.J. Simon: Optics Lett. 8, 377 (1983); Phys. Rev. Lett. 50,
      1987 (1983)
2.48 H.J. Simon, D.E. Mitchell, J.G. Watson: Phys. Rev. Lett. 33, 1531 (1974)
2.49 J.C. Quail, H.J. Simon: Phys. Rev. B31, 4900 (1985)
2.50 J.C. Quail, J.G. Rako, H.J. Simon, R.T. Deck: Phys. Rev. Lett. 50, 1987 (1983)
2.51 Y.J. Chen, G.M. Carter: Appl. Phys. Lett. 41, 307, (1982); Opt. Comm. 45, 277 (1983)
2.52 D.L. Mills: Phys. Rev. B12, 4036 (1975)
2.53 K. Arya, R. Zeyher: B28, 4090 (1983);
      K. Arya, Z.B. Su, J.L. Birman: Phys. Rev. Lett. 54, 1559 (1985)
2.54 F. Fujimoto, K. Komaki: J. Phys. Soc. Japan 25, 1679 (1968)
2.55 R.H. Ritchie, J. Crowell: Phys. Rev. 172, 436 (1968)
2.56 U. Kreibig, P. Zacharias: Z. Phys. 231, 128 (1970)
2.57 J.I. Gersten, A. Nitzan: J. Chem. Phys. 73, 3023 (1980)
2.58 P.F.Liao, A. Wokaun: J. Chem. Phys. 76, 751 (1982)
2.59 A. Wokaun, J.P. Gordon, P.F. Liao: Phys. Rev. Lett. 48, 957 (1982)
2.60 G.T. Boyd, Th. Rasing, I.R.R. Leite, Y.R. Shen: Phys. Rev. B30, 519 (1984)

Chapter 3
3.1   E. Kretschmann: Opt. Comm. 10, 356 (1974); Proc. Int. Conf. on "Thin Films", Venice
      (1972)
3.2   E. Kretschmann: Opt. Comm. 5, 331 (1972)
3.3   E. Kretschmann: Opt. Comm. 6, 185 (1972)
3.4   D. Hornauer: Thesis, Hamburg (1978)
3.5   H. Twietmeier: unpublished, Hamburg (1975)
3.6   C.F. Eagen, W.H. Weber: Phys. Rev. B19, 5068 (1979)
3.7   D.L. Hornauer: Opt. Comm. 16, 76 (1976)
3.8   R. Orlowsky, P. Urner, D. Hornauer: Surf. Sci. 82, 69 (1979)
3.9   C. Horstmann: unpublished, Hamburg (1976)
3.10 H.J. Simon, J.K. Guha: Opt. Comm. 18, 391 (1976)
3.11 J. Bodesheim, A. Otto: Surf. Sci. 45, 441 (1974)
3.12 H. Raether: Surf. Sci. 125, 624 (1983)
3.13 D.G.Hall, A.J. Braundmeier Jr.: Opt. Comm. 7, 343, (1973);
      A.J. Braundmeier Jr., D.G. Hall:Surf. Sci. 49, 367 (1975);
      D.G. Hall, A.J. Braundmeier Jr.: Phys. Rev. B17, 3808 (1978); Phys. Rev. B17, 1557
      (1978)
3.14 A.J. Braundmeier Jr., D.G. Hall: Phys. Rev. 27, 624 (1983)

3.15 F. Jansen, R.W. Hoffmann: Surf. Sci. **83**, 313 (1979); J. Vac Sci. Technol. **17**, 4, 842 (1980)
3.16 P. De Martini, P. Ristori, E. Santamato, A.C.A. Zammit: Phys. Rev. B**23**, 3797 (1981)
3.17 A.J. Braundmeier Jr., H.E. Tomaschke: Opt. Comm. **14**, 99 (1975)
3.18 R.E. Wilems, R.H. Ritchie: Phys. Lett. **15**, 882 (1965)
3.19 E. Kröger, E. Kretschmann: Z. Phys. **237**, 1 (1970)
3.20a H.J. Juranek: Z. Phys. **233**, 324 (1970)
3.20b D. Bedeaux, J. Vlieger: Physica **85A**, 389 (1976)
3.21 C. Horstmann: Opt. Comm. **6**, 176 (1977)
3.22 A.I. McAlister, E.A. Stern: Phys. Rev. **132**, 1959 (1963)
3.23 I. Brambring, H. Raether: Phys. Rev. Lett. **15**, 882 (1965); Z. Phys. **199**, 118 (1967)
3.24 P. Schreiber: Z. Phys. **211**, 257 (1968)
3.25 E. Schröder: Z. Phys. **255**, 26 (1969)
3.26 P. Pokrowsky, H. Raether: Surf. Sci. **83**, 423 (1979)
3.27 D.L. Hornauer, H. Raether: Opt. Comm. **40**, 105 (1981)
3.28 G.H. Ames, D.G. Hall: IEEE QE-**19**, 845 (1983)
3.29 I. Pockrand, H. Raether: Opt. Comm. **17**, 353 (1976)
3.30 J.R. Sandercock: Sol. Stat. Comm. **26**, 547 (1978)
3.31 A.L. Moretti, W.M. Robertson, B. Fischer, R. Bray: Phys. Rev. B**31**, 3361 (1985)

Chapter 4
4.1   D. Hornauer, H. Kapitza, H. Raether: J. Phys. D**1**, L 100 (1974)
4.2   A.J. Braundmeier Jr., E.T. Arakawa: J. Phys. Chem. Solid **35**, 517 (1974)
4.3   D. Hornauer: Thesis, Hamburg (1978)
4.4   H. Kapitza: Opt. Comm. **16**, 73 (1976)
4.5   E.T. Arakawa, M.W. Williams, R.N. Hamm, R.H. Ritchie: Phys. Rev. Lett. **31**, 1127 (1973)
4.6   R.W. Alexander, G.S. Kovener, R.J. Bell: Phys. Rev. Lett. **32**, 154 (1974)
4.7   R. Orlowsky, H. Raether: Surf. Sci. **54**, 303 (1976)
4.8   G.H. Ames, D.G. Hall, A.J. Braundmeier Jr.: Opt. Comm. **43**, 247 (1982)
4.9   H.E. Bennett, J.M. Bennett: Physics of Thin Films, Vol. 4, ed. by G. Hass (Academic Press, New York 1967) p. 1
4.10 E. Kröger, E. Kretschmann: Phys. Stat. Sol. (b) **76**, 515 (1976)
4.11 A.A. Maradudin, W. Zierau: Phys. Rev. B**14**, 484 (1976)
4.12 F.D. Toigo, A. Marvin, V. Celli, N.R. Hill: Phys. Rev. B**15**, 5618 (1977)
4.13 E. Kretschmann, T.L. Ferrell, I.C. Ashley: Phys. Rev. Lett. **42**, 1312 (1979)
4.14 S.O. Sari, D.K. Cohen, K.D. Scherkoske: Phys. Rev. B**2**, 2162 (1980); I.A. Bush, D.K. Cohen, K.D. Scherkoske, S.O. Sari: JOSA **70**, 1020 (1980)
4.15 G.C. Brown, V. Celli, M. Haller, A. Marvin: Surf. Sci. **136**, 381 (1984)
4.16 E. Kretschmann, E. Kröger: JOSA **56**, 150 (1975)
4.17 R.T. Deck, R.K. Grygier: Appl. Optics **23**, 3202 (1984)
4.18 C.K. Chen, A.R.B. de Castro, Y.R. Shen: Phys. Rev. Lett. **46**, 145 (1981)
4.19 G.T. Boyd, Th. Rasing, J.R.R. Leite, Y.R. Shen: Phys. Rev. B**30**, 519 (1984)
4.20 P.F. Liao, J.G. Bergman, D.S. Chemla, A. Wokaun, J. Melngailis, Hawryluk, N.P. Economou: Chem. Phys. Lett. **82**, 355 (1981)
4.21 J. Gersten, A. Nitzan: J. Chem. Phys. **73**, 3023 (1980); 75, 1139 (1981)
4.22 P.F. Liao, M.B. Stern: Opt. Lett. **7**, 483 (1982)
4.23 J. Moreland, A. Adams, P.K. Hansma: Phys. Rev. B**25**, 2297 (1982)
4.24 T. Inagaki, Y. Nakagawa, E.T. Arakawa, D. Aas: Phys. Rev. B**26**, 6421 (1982)
4.25 J. Lambe, S.L. McCarthy: Phys. Rev. Lett. **37**, 923 (1976); S.L. McCarthy, J. Lambe: Appl. Phys. Lett. **30**, 427 (1977); 33, 858 (1978)
4.26 P.K. Hansma, H.P. Broida: Appl. Phys. Lett. **32**, 545 (1978); A. Adams, J.C. Wyss, P.K. Hansma: Phys. Rev. Lett. **42**, 912 (1979)
4.27 R.W. Rendell, D.J. Scalapino, B. Mühlschlegel: Phys. Rev. Lett. **41**, 1746 (1978)
4.28 J.R. Kirtley, T.N. Theis, J.C. Tsang: Appl. Phys. Lett. **37**, 5, 435 (1980)
4.29 N. Kroó, Zs. Szentirmay, J. Félszerfalvi: Phys. Lett. **81A**, 399 (1981)
4.30 J. Kirtley, T.N. Theis, J.C. Tsang: Phys. Rev. B**24**, 5650 (1981)
4.31 B. Laks, C.L. Mills: Phys. Rev. B**22**, 5723 (1980)
4.32 J.E.Rowe, C.V. Shank, D.A.Zwemer, C.A. Murray: Phys. Rev. Lett. **44**, 1770 (1980)

4.33 M. Moskowitz: J. Chem. Phys. **69**, 4159 (1978)
4.34 A. Girlando, M.R. Philpott, D. Heitmann, J.D. Swalen, R. Santo: J. Chem. Phys. **72**, 5187 (1980)

Chapter 5

5.1 D.E. Barrick: In: *Radar Cross Section Handbook*, Vol. 2, ed. by G. Ruck (Plenum Press, New York 1970) p. 706
5.2 E. Kröger, E. Kretschmann: Z. Phys. **237**, 1 81970)
5.3 O. Hunderi, D. Beaglehole: Phys. Rev. **B2**, 321 (1970)
5.4 A.A. Maradudin, D.L. Mills: Phys. Rev. **B11**, 1392 (1975)
5.5 J.M. Elson: Phys. Rev. **B12**, 2541 (1975)
5.6 U. Hillebrecht: unpublished, Hamburg (1979)
5.7 V. Permien: unpublished, Hamburg (1977)
5.8 D. Heitmann, V. Permien: Opt. Comm. **23**, 131 (1977)
5.9 U. Hillebrecht: J. Phys. D., Appl. Phys. **13**, 1625 (1980)
5.10 D. Beaglehole, O. Hunderi: Phys. Rev. **B2**, 309 (1970)
5.11 S.O. Sari, D.K. Cohen, K.D. Scherkoske: Phys. Rev. **B2**, 2162 (1980);
I.A. Bush, D.K. Cohen, K.D. Scherkoske, S.O. Sari: JOSA **70**, 1020 (1980)
5.12 H. Lichte, G. Möllenstedt: J. Phys. E, Sci. Instrum. **12**, 941 (1979)
5.13 J. Trümper, B. Aschenbach, H. Bräuninger: SPIE **184**, Space Optics 12 (1979);
B. Aschenbach, H. Bräuninger, G. Hasinger, J. Trümper: SPIE **257**, 223 (1981)
5.14 A. Braslau, M. Deutsch, P.S. Pershan, A.H. Weiss: Phys. Rev. Lett. **54**, 114 (1985)
5.15 G. Hass, W.R. Hunter, R.J. Tousey: Opt. Soc. Am. **46**, 1009 (1956)
5.16 W.R. Hunter: JOSA **54**, 208 (1964)
5.17 I.G. Endriz, W.G. Spicer: Phys. Rev. **4**, 4144, 4159 (1971)
5.18 S.N. Jasperson, S.E. Schnatterly: Phys. Rev. **188**, 759 (1969)
5.19 W. Kaspar, U. Kreibig: Surf. Sci. **69**, 619 (1977)
5.20 E. Schröder: Opt. Comm. **1**, 13 (1969)
5.21 A. Daudé, A. Savary, S. Robin: JOSA **62**, 1 (1972)
5.22 T.F. Gesell, E.T. Arakawa, M.W. Williams, R.N. Hamm: Phys. Rev. **B7**, 5141 (1973)
5.23 J.M. Elson, R.H. Ritchie: Phys. Rev. **B4**, 4129, (1971); Phys. Stat. Sol. (b) **62**, 461 (1974)
5.24 B.P. Feuerbacher, W. Steinmann: Opt. Comm. **1**, 81 (1969)
5.25 L.J. Cunningham, A.J. Braundmeier Jr.: Phys. Rev. **B14**, 479 (1976)
5.26 H.E. Bennett, J.M. Bennett: Physics of Thin Films, Vol. 4, ed. by G. Hass (Academic Press, New York 1967) p. 1
5.27 G. Harbeke, L. Krausbauer, E. Steigmeier, A. Widmar: RCA Review **44**, 287 (1983)
5.28 R. Kötz, D.M. Kolb: Z. Physikal. Chem. **112**, 69 (1978)
5.29 D.M. Kolb: "The study of Solid-Liquid Interfaces by Surface Plasmon Polariton Excitation", Chap. 8 of [2.4] p. 299–329
5.30 J.M. Elson, J.P. Rahn, J.M. Bennett: Applied Optics **22**, 3207 (1983)

Chapter 6

6.1 I. Pockrand: Phys. Lett. **49A**, 259 (1974)
6.2 I. Pockrand, H. Raether: Opt. Comm. **18**, 395 (1976)
6.3 I. Pockrand, H. Raether: Appl. Opt. **16**, 1784, 2803 (1977)
6.4 D. Heitmann, H. Raether: Surf. Sci. **59**, 1 (1976)
6.5 D. Heitmann: Phys. Stat. Sol. (b) **88**, 493 (1978)
6.6 P. Beckmann, A. Spizzichino: *The Scattering of Electromagnetic Waves from Rough Surfaces* (Pergamon Press, New York 1963)
6.7 D. Heitmann: Opt. Comm. **20**, 292 (1977)
6.8 J. Moreland, A. Adams, P.K. Hansma: Opt. Comm. **45**, 11 (1983)
6.9 H. Raether: Opt. Comm. **42**, 217 (1982)
6.10 R. Petit, M. Cadilhac: C.R. Acad. Sci. **B262**, 468 (1966);
R.F. Millar: Proc. Camb. Philos. Sci **65**, 773 (1969);
N.R. Hill, V. Celli: Phys. Rev. **B17**, 2478 (1978)
6.11 I have to thank Dr. M. Weber (Irvine) for this information.
6.12 D. Maystre: Opt.Comm. **8**, 216 (1973)
6.13 I. Pockrand:J. Phys. D, Appl. Phys., **9**, 2423 (1976)
6.14 M.C. Hutley, D. Maystre: Opt. Comm. **19**, 431 (1976)

6.15 F.D. Toigo, A. Marvin, V. Celli, N.R. Hill: Phys. Rev. B15, 5618 (1977)
6.16 G. Diaz, N. Garcia, H. Raether: Surf. Sci. 146, 1 (1984)
6.17 W. Rothballer: Opt. Comm. 29, 429 (1977)
6.18 K. Berthold, R.A. Höpfel, E. Gornik: Appl. Phys. Lett. 46, 626 (1985)
6.19 R.K. Jain, M.G. Farrier, T.K. Gustafson: Phys. Rev. Lett. 36, 435 (1976)
6.20 S.R.J. Brueck, V. Diadiuk, T. Jones, W. Lenth: Appl. Phys. Lett. 46, 915 (1985)
6.21 K. Berthold, W. Beinstingl, R. Berger, E. Gornik: (in press)
6.22 D. Heitmann: J. Phys. C, Solid State Phys. 10, 397 (1977)
6.23 E.H. Rosengart, I. Pockrand: Opt. Lett. 1, 149 (1977)
6.24 R.H. Ritchie, E.T. Arakawa, J.J. Cowan, R.N. Hamm: Phys. Rev. Lett. 21, 1530 (1968)
       D.L. Mills, M. Weber: Phys. Rev. B26, 1075 (1982)
       M. Weber, D.L. Mills: Phys. Rev. 27, 2698 (1983)
6.25 N.E. Glass, M. Weber, D.L. Mills: Phys. Rev. B29, 6548 (1983)
6.26 N.E. Glass, A.A. Maradudin, V. Celli: Phys. Rev. B27, 5150 (1984)
6.27 N. Garcia: Opt. Comm. 45, 307 (1983);
       N. Garcia, G. Diaz, J.H. Saenz, C. Ocal: Surf. Sci. 143, 342 (1984)
6.28 J.L. Coutaz, M. Nevieère, E. Pic, R. Reinisch: Phys. Rev. B (in press)
6.29 J.C. Tsang, J.R. Kirtley, T.N. Theis: Solid State Commun. 35, 667 (1980)
       J.R. Kirtley, S.S. Jhan, J.C. Tsang: Solid State Commun. 35, 509 (1980)
6.30 H.W.K. Tom, C.K. Chen, A.R.B. de Castro, J.Y.R. Shen: Solid State Commun. 41, 259 (1982)
6.31 H. Numata: J. Phys. Soc. (Japan) 51, 2575 (1982)
6.32 M. Nevieère, R. Reinisch: Phys. Rev. B26, 5403 (1982)
6.33 G.S. Agarwal: Phys. Rev. B31, 3534 (1985)
6.34 R.H. Ritchie, E.T. Arakawa, J.J. Cowan, R.N. Hamm: Phys. Rev. Lett. 21, 1530 (1968)
6.35 I. Pockrand: Thesis, Hamburg (1978)
       Y.J. Chen, E.S. Koteles, R.J. Seymour, G.J. Sonak, J.M. Ballantyne: Sol. State Comm. 46, 95 (1983)
6.36 B. Laks, D.L. Mills, A.A. Maradudin: Phys. Rev. B23, 4965 (1981);
       D.L. Mills: Phys. Rev. B15, 3097 (1977)
6.37 W. Rothballer: unpublished, Hamburg (1976)
6.38 I. Pockrand: Opt. Comm. 13, 311 (1975)
6.39 R.E. Palmer, S.E. Schnatterly: Phys. Rev. B 2329 (1971)
6.40 R. Köth, H.J. Lewerenz, E. Kretschmann: Phys. Lett. 70A, 452 (1979)
6.41 M.W. Williams, J.C. Ashley, E. Kretschmann, T.A. Callcott, M.S. Chung, E.T. Arakawa: Phys. Lett. 73A, 231 (1979)
6.42 E. Kretschmann, T.L. Ferrell, I.C. Ashley: Phys. Rev. Lett. 42, 1312 (1979)
6.43 A.A. Maradudin: Chapter 10, p. 501, in [2.4]

Appendix
A.1 H. Wolter: in Handbuch der Physik, Vol. 24 (Springer, Berlin 1956) p. 461
A.2 U. Schröder: Surf. Sci. 102, 118 (1981)
A.3 P.B. Johnson, R. Christie: Phys. Rev. B6, 4370 (1972)
A.4 M. Otter: Z. Physik 161, 163 (1961)
A.5 M.M. Dujardin, M.L. Thèye: J. Phys. Chem. Solids 32, 2033 (1971);
       M.L. Thèye: Phys. Rev. B2, 3060 (1970)
A.6 G. Hincelin: Thèse 1985. Université de Paris-Sud (Centre d'Orsay)
A.7 J. Bösenberg: Z. Phys. B22, 261 (1975)

Subject Index